



Università degli Studi di Napoli *Federico II*

DOTTORATO DI RICERCA IN
FISICA FONDAMENTALE ED APPLICATA

Ciclo XXVII
Coordinatore: Prof. R. Velotta

**Aerosol attenuation measurements for
cosmic rays experiments: the Pierre
Auger Observatory experience and
the ARCADE project**

Settore Scientifico Disciplinare FIS/01

Dottorando:
Mario Buscemi

Tutor:
Dr. L. Valore
Dr. F. Guarino

Contents

Introduction	3
1 The Physics of Cosmic Rays	6
1.1 A brief history	6
1.2 Cosmic ray energy spectrum	7
1.3 Sources and acceleration mechanisms	9
1.4 Mass composition	11
1.5 Extensive Air Shower	12
1.6 Detection of Extensive Air Showers	14
1.6.1 EAS fluorescence light emission and detection	15
1.7 Effects of the atmosphere on the detection of EAS	18
1.7.1 Properties of the Atmosphere	18
1.7.2 Light Attenuation in the Atmosphere	21
2 The Pierre Auger Experiment	25
2.1 Description of the Observatory	25
2.1.1 Hybrid design	26
2.2 The Surface Detector: SD	28
2.3 The Fluorescence Detector: FD	30
2.3.1 FD Calibration	34
2.4 Event reconstruction	35
2.4.1 FD Event reconstruction	36
2.4.2 SD Event reconstruction	38
2.5 The Offline Software Framework	42
2.6 Highlights of science results	43
2.6.1 All-particle spectrum	43
2.6.2 Mass composition	43
2.6.3 Photon and neutrino limits	44
2.6.4 Arrival direction distribution	45
2.6.5 Air shower and hadronic interaction physics	46
2.7 The upgrade of the Pierre Auger Observatory	47

2.8	Atmospheric Monitoring at the Pierre Auger Observatory . . .	49
2.8.1	Atmospheric Monitoring Devices	52
2.8.2	Measurements of the VAOD profiles using CLF and XLF	56
2.9	A comparison of techniques: the ARCADE project	59
3	Aerosol attenuation measurements in the Auger experiment	60
3.1	Introduction	60
3.2	Laser Simulation technique	61
3.2.1	Simulation of a laser event	62
3.2.2	Reconstruction of a laser event	64
3.2.3	VAOD measurements	66
3.3	My contributions in the data analysis	69
3.3.1	XLF data analysis	69
3.3.2	New Auger aerosol database	72
3.3.3	Upgrade of the Laser Simulation Analysis	79
4	The ARCADE project	82
4.1	Description of the project	82
4.2	Design and construction phase	84
4.2.1	The lidar	84
4.2.2	The Atmospheric Monitoring Telescope	100
4.3	Implementation phase	102
4.3.1	Set-up of the AMT	102
4.3.2	Set-up of the lidar	103
4.4	Data taking	105
5	ARCADE data analysis	108
5.1	Introduction	108
5.2	VAOD measurements using the AMT	108
5.2.1	Geant4 simulation of the AMT	109
5.2.2	AMT calibration	113
5.2.3	AMT data analysis	114
5.3	VAOD measurements using the lidar	119
5.3.1	Raman lidar analysis	121
5.3.2	Elastic lidar analysis	125
5.4	Next step: comparison of the results	126
	Conclusions	127
	Bibliography	130

Introduction

The aim of my PhD research activity is the characterization of the optical properties of the atmosphere in the near UV, in particular the tropospheric aerosol attenuation, topic strongly needed by the cosmic rays physics community. In cosmic rays experiments, for energies greater than 10^{18} eV, the identification of the properties of primary particles is obtained through the study of the shower of particles generated by their interaction in the atmosphere (see Chapter 1). One of the techniques commonly used to achieve this goal is based on the detection of the UV fluorescence light (in the range between 300 and 420 nm) that the nitrogen molecules of the atmosphere emit after the interaction with the particles of the shower. This technique allows to reconstruct the development of a shower in the atmosphere by the measurement of the profile of light emitted at different altitudes. Since the amount of fluorescence light emitted is proportional to the energy dissipated by the shower, a fluorescence detector provides a nearly calorimetric measurement of the energy of the particle that initiated the shower. Moreover a fluorescence detector is sensitive to the mass of the primary cosmic ray, due to the fact that the development of showers in atmosphere is strongly dependent from the nature of the primary particle: showers initiated by heavy nuclei are shallower from those generated by protons.

The most significant and variable phenomenon that affects the measurements of the fluorescence light is the scattering of light due to aerosols. For example a correct estimation of the aerosol attenuation can lead to a correction of the energy of the shower that can range from a few percent to more than 40%, depending on the aerosol attenuation conditions, the distance of the shower, and the energy of the primary particle. For this reason cosmic rays experiments need a network of instruments for a continuous monitoring of the aerosol attenuation.

Instruments usually dedicated to the measurement of the aerosol attenuation in atmospheric physics community are the Lidars (LIght Detection And Ranging). Lidar measurements need long acquisition time, and since their use interferes with usual shower acquisition, these instruments can't be used

in a cosmic rays observatory during data taking. For this reason other faster techniques to measure aerosol optical depth based on side-scattering measurements of vertical laser track, have been developed.

Within the activities described above, during my PhD I have been working within the Pierre Auger Collaboration and in the ARCADE project (Atmospheric Research for Climate and Astroparticle Detection).

The Pierre Auger Observatory is the largest cosmic rays observatory in the world (see Chapter 2). It was designed to study Ultra High Energy Cosmic Rays (UHECRs) from fraction of EeV to the highest energies ever observed (hundreds of EeV), with the aim to answer to all the questions that are still open in this research field. The measurement of the properties of the extensive air showers (EAS) allows the determination of the energy and arrival direction of each cosmic ray and also provide a statistical determination of the distribution of primary masses. The essential feature of the Pierre Auger Observatory is its hybrid design: EAS are detected simultaneously by the *Surface Detector*, an array of Cherenkov detectors covering an area of 3000 km^2 , and by the *Fluorescence Detector*, consisting in 24 telescopes placed in 4 sites disposed at the borders of the area occupied by the Surface Detector. The complementarity of these techniques provides important cross-checks and measurement redundancy.

My activity in the Auger Collaboration has been focused on the analysis of data obtained using the two laser facilities of the observatory (CLF and XLF). The analysis of the light emitted by the lasers and collected by the Fluorescence Detector after side-scattering within the atmosphere is used to measure the atmospheric aerosol attenuation. The technique I used for the data analysis is the so-called “Laser Simulation Analysis”, a method fully developed in the Naples group in the past years. The Laser Simulation Analysis compares measured to simulated laser events, generated varying the aerosol conditions, to find the best compatibility. Results of the analysis are stored in the Auger Aerosol Database that is used for the reconstruction of shower data.

During my PhD I was involved in many items related to the aerosol atmospheric monitoring (see Chapter 3):

- I performed the analysis of the XLF data for the first time, adapting the analysis technique to the new laser facility.
- I took part to the complete revision of the Auger Aerosol Database, released in April 2013: this database contains data from 2004 to 2012 and was used for the update of the “energy scale” of the experiment. For this release a certain number of improvements were included with

respect to previous releases, that brought to the recalculation of the uncertainties related to the optical depth profiles.

- I worked on an upgrade of the “Laser Simulation Analysis” in order to produce more realistic profiles of aerosol attenuation that takes into account the characteristics of the atmosphere in its lowest part, the planetary boundary layer.

The use of the side-scattering technique introduce some assumptions on the features of the atmosphere and its results need to be checked using other methods. An experiment designed for this purpose is the ARCADE project in which I was involved for all the duration of my PhD. It is a three year project started in 2012 and funded by the MIUR; it was conceived to solve the open problems affecting the measurements of aerosol attenuation obtained with the typical techniques used in cosmic rays experiments. The goal of the project is the comparison of some techniques (side-scattering measurement, elastic lidar and Raman lidar) in order to assess the systematic errors affecting each method providing simultaneous observations of the same air mass. For this purpose we designed a steerable lidar: it uses a 355 nm Nd:YAG laser and collects the elastic and the N_2 Raman-shifted back-scattered light. For the side-scattering measurement we use the Atmospheric Monitoring Telescope (AMT), a facility owned by the Colorado School of Mines and placed in Lamar (Colorado), the site where the experiment has taken place since June 2014 and is currently in acquisition. All the operations of the experiment are controlled remotely from Italy. I took part to all the phases of the project, from the design to the data analyses: all the the details of the project are described in Chapter 4, where all my first hand contributes are highlighted. The description of the analysis methods that I developed for the data analysis of both devices will be described in Chapter 5, together with some preliminary results.

Chapter 1

The Physics of Cosmic Rays

1.1 A brief history

Cosmic ray physics, born almost by chance, opened the door to the particle physics and gave a big contribution in the understanding of geophysical, solar and planetary phenomenon.

The discovery of cosmic rays had its origin in the need of understanding why a heavily shielded detector still recorded radiation. Since the 19th century scientists noticed the spontaneous discharging of electroscopes and were not able to explain this phenomena. The puzzle seemed to be solved after the discovery of ionizing radiation: these radiations can ionize the air surrounding an electrically charged electroscope causing its neutralization. Since this phenomenon occurred also when no radioactive sources were close to the electroscope and when it was heavily shielded, physicists assumed that the spontaneous discharging was due to some residual high penetrating radiation emitted by the earth. If true, the detected radiation should have been reduced by placing a detector at some distance from the earth's surface. In 1912 Victor Hess [1] carried an ion chamber on a balloon up to several thousand meters above the earth's surface. During the ascension of the balloon, he observed that the radiation level first decreased, but then, above 1000 m, it started to rise. This measurement led to the conclusion that the radiation had an extraterrestrial origin, and that its intensity decreased approaching the sea level due to the interaction in atmosphere.

After this discovery many hypothesis were offered in order to explain the nature of these so-called cosmic rays. In 1933 Arthur Compton demonstrated that the intensity of the cosmic radiation depended on the magnetic latitude [2]: cosmic rays were predominately charged particles and not γ rays as previously hypotized.

The same year Bruno Rossi placed three Geiger-Muller counters on the same plane to form a triangle and observed a rapid increase of triple coincidences when some samples of lead were placed above the system. Coincidences were due to different particles hitting the counters at the same time: this experiment was the first record of a shower of secondary particles produced by a cosmic ray. In 1938 Pierre Auger and Roland Maze observed time coincidences between cosmic ray particles separated by a distance of approximately 20 meters proving that cosmic rays interacting with the atmosphere can produce a shower of secondary particles, the so-called "Extensive Air Shower", or EAS [3]. In 1962 John Linsley recorded a cosmic ray event with energy of 10^{20} [4], measurement that opened the era of the Ultra High Energy Cosmic Rays (UHECR) research.

1.2 Cosmic ray energy spectrum

The range of energies covered by the cosmic rays spectrum is very broad, spanning 11 orders of magnitude from $10^9 eV$ to $10^{20} eV$ (Fig. 1.1). The flux of cosmic rays drops off dramatically at a rate of about 3 order of magnitude per energy decade following the power law:

$$\frac{dN}{dE} \sim E^{-\gamma} \quad (1.1)$$

The value of the flux is 1 particle per m^2 per second at energies of about $10^{11} eV$ and decreases to 1 particle per km^2 per century at energies above $10^{20} eV$. A deep examination of the spectrum shows different changes in the spectral index γ : at the lowest energy its value is about 2.6 - 2.7, at about $3 \cdot 10^{15} eV$ a steepening of the spectrum is visible, the so-called *knee*, where $\gamma \sim 3$, and then a *second knee* appears at about $5 \cdot 10^{17} eV$ where the spectral index is about 3.3 [6]. A flattening in the spectrum appears at about $4 \cdot 10^{18} eV$ where $\gamma \sim 2.55$, the so-called *ankle* [7]. Different values of the spectral index, in some energy regions, can indicate a change in the origin and in the mass composition of cosmic rays. This change may depend on the *magnetic rigidity* defined as $R = \frac{Pc}{Ze}$, where P is the the total momentum of a nucleus and Ze its electrical charge: in particular if there is a maximum energy to which particles can be accelerated, then highest particles will cutoff first [5]. According to the classical theory in the knee region particles originated in the Milky Way by acceleration of supernovae remnants (SNR) begins to be not confined in the galaxy [8]. The region between the first and the second knee can be associated with a transition from a light mass composition (mostly proton) to a heavier one. Concerning the ankle, according to one of the

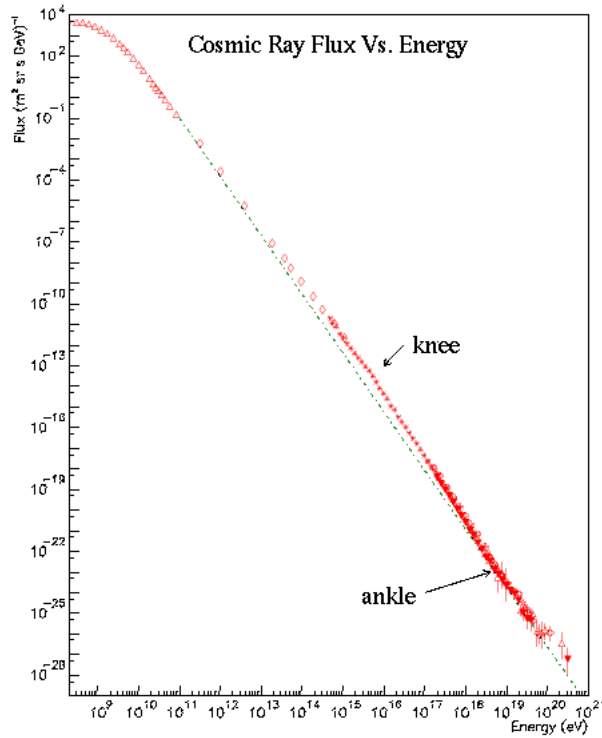


Fig. 1.1: Cosmic rays energy spectrum

proposed theories, it is due to the transition to particles from extra-galactic sources. Above the ankle ($E > 4 \cdot 10^{18} eV$) the spectral index changes and assumes the value 2.5: the spectrum is then suppressed by a factor two at $E \sim 10^{19.6} eV$ [7]. It is not still clear if this behavior is due to a limit in the maximum acceleration energy of cosmic rays sources or if it is related to the so called GZK effect[9, 10]. This effect, that takes its name from the physicist Greisen, Zatsepin and Kuzmin, foresees a cutoff in the cosmic rays energy spectrum at the highest energies. The cutoff is due to the interaction of cosmic rays primaries with the *cosmic microwave background radiation* (CMBR), the thermal (2.7 K) radiation produced during the Big Bang that is present in the whole Universe. Taking into account the thresholds of particles production in the interaction of different cosmic ray primaris with the CMBR and the relative mean free path, the GZK theory predicts the impossibility for primaries of energy above $\sim 5 \cdot 10^{19}$ to travel through distances above 100 *Mpc*: detection of primaries with energy above the GZK limit suggests their origin from near-Earth sources , and since at these energies primaries do not suffer deflections by galactic/extragalactic magnetic field, they should point directly to their source, allowing their individuation.

1.3 Sources and acceleration mechanisms

One of the consequences of the extension of the energy spectrum of cosmic rays up to $10^{15}eV$ is that it is actually impossible to imagine a single process able to give to a particle such an energy. It seems much more likely that the charged particles which constitute the primary cosmic radiation acquire their energy along electric fields of a very great extension[11].

This was the conclusion of Pierre Auger after the discovery of cosmic particles with an energy of $10^{15}eV$, and, after more than eighty years, the question related to the origin of cosmic rays has not been definitely answered yet, even if many experiments significantly contributed to a better understanding of this topic.

Since the largest part of this radiation consists in charged particles, cosmic rays suffer interaction with galactic magnetic field. This interaction deletes the informations on their provenance with the exception of ultra high energy cosmic rays ($E > 10^{18}$), that are only slightly deflected from their original path and so point to their sources.

In general two basic acceleration mechanisms can explain the existence of cosmic rays with energies up to $10^{20}eV$: the *bottom-up* and *top-down* processes.

In the bottom-up process particles are accelerated by astrophysical sources. For example the bulk of cosmic rays ($E < 10^{15}eV$) is believed to be confined in the galaxy and seems to be accelerated by shock waves from supernovae remnants as proposed by Fermi in 1949 [12] (statistical or Fermi acceleration). In general the maximum energy that a particle with an electric charge Z can achieve, if accelerated by this mechanism, depends on the size of the source (L), on the strength of its magnetic field (B) and on the the speed of the shock wave (β) [13]:

$$E_{max} \sim ZBL\beta \tag{1.2}$$

Some possible astrophysical sources of acceleration are shown in the Hillas plot in Fig.1.2. In this scenario, only a few sources (i.e. Gamma Ray Bursts (GRB) and Active Galactic Nuclei (AGN)) can accelerate proton at energy up to $10^{20}eV$.

On the other hand, top-down acceleration mechanisms explain UHECRs as produced by the decay of super-heavy exotic particles [14, 15] or of topological defects [16, 17].

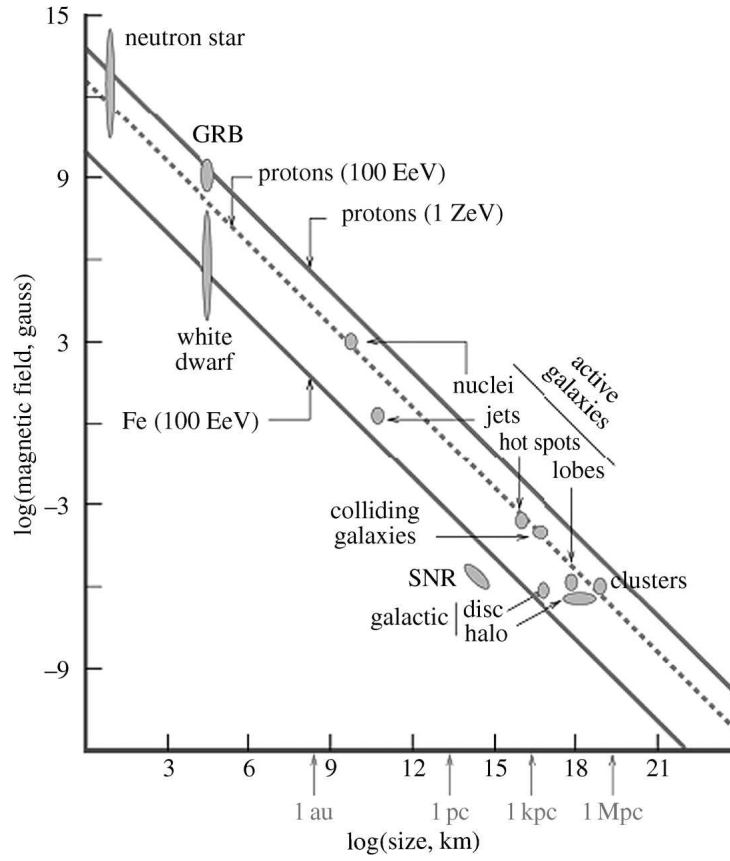


Fig. 1.2: The Hillas plot: size and magnetic field of possible astrophysical acceleration sources are shown. Each line represents the maximum energy achievable by a particle accelerated by a source placed in that region.

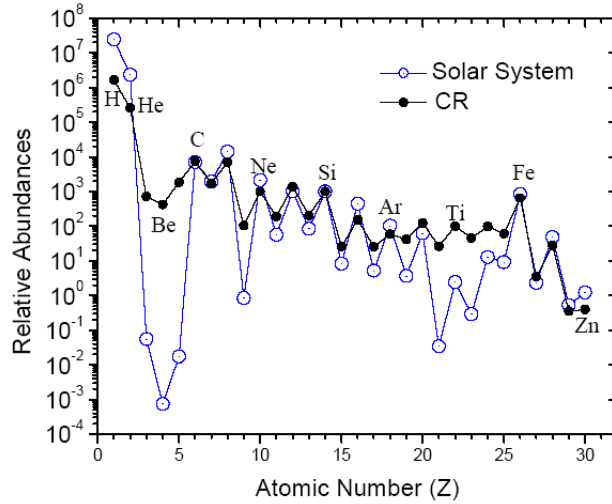


Fig. 1.3: Comparison between the abundance of elements in the cosmic rays and in the Solar System.

1.4 Mass composition

The mass composition of cosmic rays at low energies, up to $10^{14}eV$, has been carefully investigated through direct measurements of primary particles. The 99.8% of them are charged particle, and the remaining 0.2% consists of photons and neutrinos. Charged particles are composed by nuclei (98%), positrons and electrons (2%); protons represents the 87% of nuclei, the 12% are helium nuclei and the remaining part heavy nuclei. The abundance of cosmic rays is comparable with the abundance of elements in the Solar System (Fig. 1.4). The only differences are for elements below Carbon ($Z = 6$) and Iron ($Z = 26$) where CR abundance is greater than the one of Solar System: these elements are not produced in stellar nucleosynthesis but could be generated in heavy nuclei fragmentation processes.

At energies above $10^{14}eV$ direct measurements of primaries are no longer achievable due to the low flux of particles. The only way to study cosmic rays is then left to the detection of Extensive Air Showers: the atmospheric depth of the shower maximum, X_{max} , is sensitive to the mass of the primary particle, but due to the statistical nature of the process, it is no longer possible to identify the chemical composition of each primary but only informations on the average mass composition can be achieved.

Mass composition becomes heavier between the first and the second knee, because at these energies light particles are no more confined by the galactic magnetic field. At higher energies, above the ankle, the scenario is less clear:

the results of the the Pierre Auger Observatory suggest a trend towards heavier elements at the highest energies; on the other hand the data of other experiments, such as Hires and Telescope Array, are compatible with a light composition at all energies. The debate is still open and the forthcoming upgrade of the Pierre Auger Observatory (see sec. 2.7) will shed light on the issue.

1.5 Extensive Air Shower

The flux of cosmic rays decreases dramatically with energy and above $10^{14}eV$ it is difficult to make direct measurements on balloon or space craft: only the production of secondary particles by the interaction of the primary with the atmosphere allows their detection. The number of particles starts to increase rapidly as this cascade of particles moves downwards in the atmosphere. On their way, and in each interaction, particles lose energy and eventually will not be further able to create new particles, reaching finally, nearly-simultaneously, a large area where they can be detected: this phenomena is called Extensive Air Shower (EAS).

Showers can be classified in electromagnetic and hadronic; when an hadron interact with the molecules of the atmosphere it produces mostly pions and some kaons. Neutral pions decay in two γ initiating an electromagnetic shower that carries about 30% of the primary energy.

The simplest way to understand the properties of an electromagnetic shower is the Heitler toy model [18]. In this model a particle with energy E_0 starts the shower that propagates only by pair production from photons and bremsstrahlung of electrons and positrons (see Fig. 1.4(a)). In both processes it is assumed that the interaction happens after the same interaction length $X_0 \sim 37gcm^{-2}$ and that the two particles produced, e^- and e^+ in pair production, and photon and e^- or e^+ in the bremsstrahlung process, share the energy of the mother particle equally; the multiplication process continues until the energy of the particles reaches the critical energy E_C , when the increase of particles is balanced by the absorption of particles in the atmosphere due to radiative and ionization processes: this point marks the shower maximum (X_{max}).

The number of particle grows geometrically after each step, so after $n = X/X_0$ steps, the total number of particles as a function of the slant depth, the so-called *longitudinal development*, is:

$$N(X) = 2^{X/X_0} \tag{1.3}$$

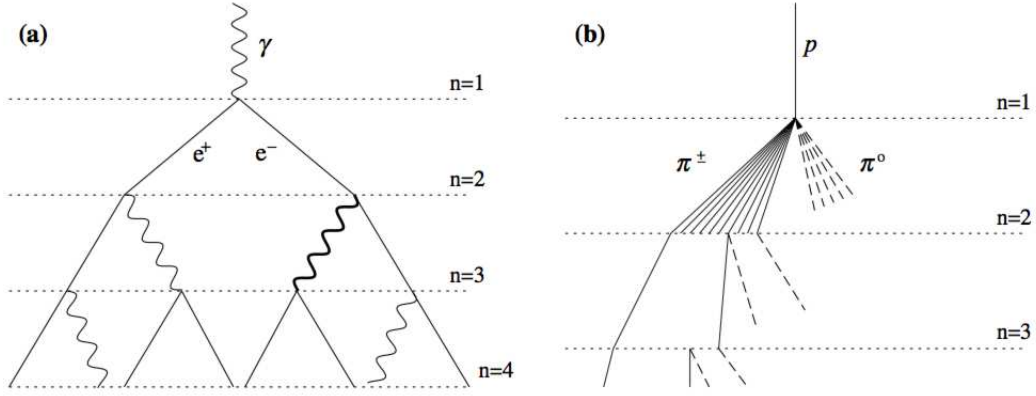


Fig. 1.4: Scheme of the electromagnetic (a) and hadronic (b) development in the Heitler model.

and the energy of each particle is:

$$E(X) = \frac{E_0}{N(X)} \quad (1.4)$$

So the number of particles and the atmospheric depth of the shower maximum are:

$$N(X_{max}) = \frac{E_0}{E_C} \quad (1.5)$$

$$X_{max} = \ln\left(\frac{E_0}{E_C}\right) \cdot \frac{X_0}{\ln 2} \quad (1.6)$$

Summarizing, the main results of the Heitler model are that the amount of particles at the maximum of the electromagnetic shower is proportional to the energy of the primary particle E_0 , and that the atmospheric depth of the shower is proportional to the $\ln(E_0)$.

Hadronic showers originate from the decay of charged pions neutrinos and muons. Neutrinos do not interact and are not detectable and then represent the "invisible" energy of the shower, while the number of muons produced changes slowly with the energy; in a shower induced by a proton the number of muons generated is proportional to $E^{0.85}$, so assuming a nucleus with mass A as a collection of Z protons it will produce about 80% more muons than a shower induced by a proton: an accurate measure of the muon content of a shower could allow the mass discrimination of primary particles.

A modified Heitler model adapted to hadronic showers can be found in [19].

In this case the primary energy is proportional to a combination of the number of muons and electrons produced in the shower:

$$E_0 = (N_e + kN_\mu) \quad (1.7)$$

where the relative weighting k depends mainly on the characteristic energy scales at which hadronic cascading and electromagnetic showering cease.

1.6 Detection of Extensive Air Showers

Different techniques have been developed to detect and to study EAS and all of them are based on two main methods: the first consists in the measurement of the secondary particles of the shower that reach the ground through an array of detectors on the Earth's surface; the second studies the longitudinal development of the shower in the atmosphere through the measurement of the electromagnetic radiations emitted by the secondary particles in their travel through the atmosphere.

Surface detectors: since the pioneering work of Pierre Auger in 1938, surface detectors have been widely used for the detection of EAS. Detectors are placed on a large area forming an array; the distance between two of them and the total area covered by the array depend on the range of energies of primaries that should be measured. Cascades generated by lower energy particles have a smaller size ($\sim 1 \text{ km}^2$ at 10^{15} eV), therefore small but dense arrays are needed for their detection; at the highest energies the size of the shower at ground increases dramatically ($\sim 100 \text{ km}^2$ at 10^{18} eV) but the flux is very low, so large arrays are needed in order to accumulate enough events. Typically large arrays are made of scintillator detectors (e. g. AGASA [20], Cascade-Grande [6], Telescope Array [21]) or Cherenkov detectors as in the Pierre Auger Observatory whose surface detector will be described more in detail in sec. 2.2. The main advantage of the use of surface detectors is their duty cycle of 100%, and, when detectors are made of different layers, the possibility of discriminate the muonic component of the shower from the electromagnetic one, allowing the direct study of the mass composition of the primaries; on the other hand a critical issue of this technique is the indirect measurement of the energy of primaries. This involves the usage of simulations of the shower development in the atmosphere introducing systematic uncertainties due to the limited knowledge of the hadronic interaction at such high energies.

Electromagnetic radiations detectors: The passage of charged particles of a shower through the atmosphere can lead to radiation emission: Cherenkov light emitted by relativistic particles, fluorescence light due to

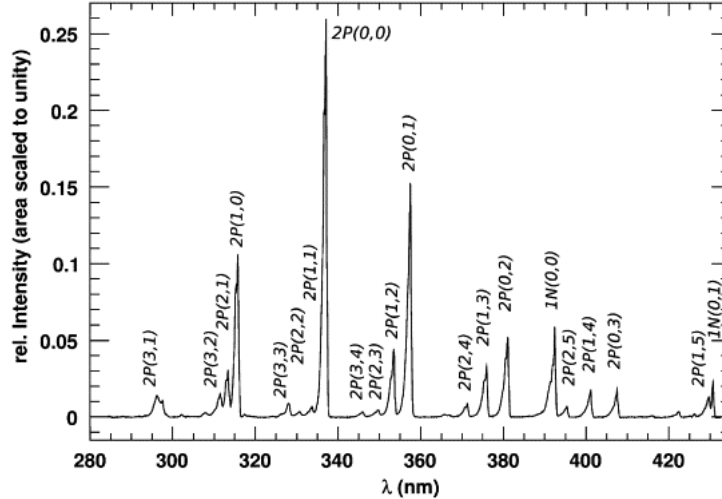


Fig. 1.5: Air fluorescence spectrum as measured by the AIRFLY collaboration [24]

the interaction with air molecules, and radio emission due to the deflection of electrons and positron in the Earth’s magnetic field [22]. In the next paragraphs I will introduce the techniques for detection of EAS based on the measurements of the fluorescence light emitted after the interaction of secondary particles of the shower with the atmosphere, describing in detail the mechanisms of emission. The advantage of this technique is to give a calorimetric measurement of the energy of the shower, the limitation is the low duty cycle, in fact fluorescence measurements can be performed only during moonless night.

1.6.1 EAS fluorescence light emission and detection

Measurement of fluorescence light released during the air showers development provides a calorimetric measurement of the energy deposited in the air by the shower. This energy is assumed to be proportional to the energy of the primary particle that generated the cascade: this is the most direct and model independent method to determine the energy of an UHECR [23].

When electrons go through the atmosphere, they lose energy due to inelastic collisions with air molecules. A small fraction of this energy is absorbed by nitrogen molecules and then released as UV radiation in the spectral range $\sim 300 - 420$ nm [25, 26]. A measured air fluorescence spectrum is shown in Fig. 1.5. In this spectral range nitrogen fluorescence emission takes place after nitrogen excitation or ionization. In the first case the emission comes

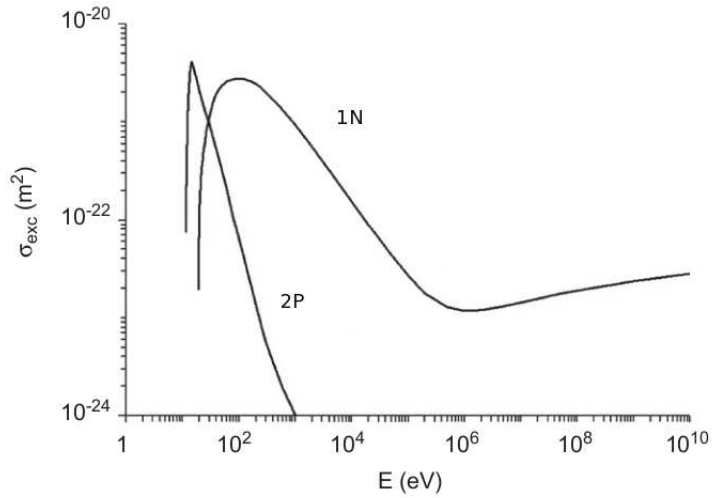


Fig. 1.6: Cross sections for the nitrogen excitation as a function of electron energy.

from the Second Positive system (2P) of N_2 , in the latter from the First Negative system (1N) of N_2^+ . The cross section for excitation of both systems as a function of electron energy is shown in Fig. 1.6. The excitation cross section for the 2P system shows a maximum at about 15 eV followed by a fast decrease due to the optically forbidden nature of the transition, while the curve of 1N system shows a maximum at about 100 eV followed by a slower decrease. It is clear that air fluorescence is mostly due to low-energy secondary electrons produced in ionization process since the process is very inefficient for energetic primary particles.

Fluorescence emission is not the only process that excited nitrogen molecules can undergo: indeed there are some processes that compete with it and the most important is the collisional quenching, a process that depends on the atmospheric pressure. In this process excited nitrogen molecules lose their excitation energy by collision with other air molecules.

The number of fluorescence photons ϵ_λ with wavelength λ per unit path length emitted after the deposit of the energy E_{dep} by an electron is [23]:

$$\epsilon_\lambda = Y_\lambda \cdot \frac{\lambda}{hc} \cdot E_{dep} \cdot \rho_{air} \quad (1.8)$$

where ρ is the air density referred to the position of the photon emission, and Y_λ is the so-called *fluorescence yield*: it is defined as the number of fluorescence photons emitted per unit of deposited energy and includes air temperature, pressure and umidity dependences [27]. The fluorescence emis-

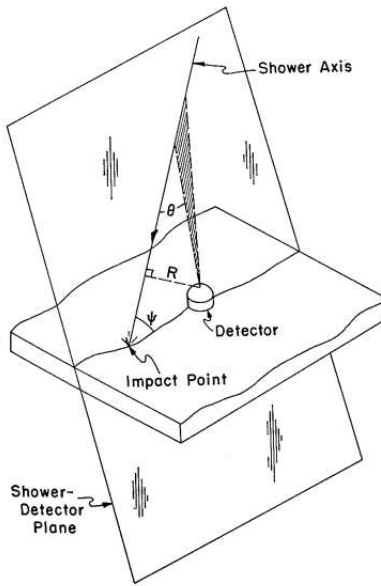


Fig. 1.7: Scheme of the shower geometry for fluorescence detector observations.

sion is isotropic and its average value is about 4 photons per meter of electron track.

EAS detection based on the measurement of the fluorescence light assumes the fluorescence yield to be independent from the electron energy and the fluorescence intensity to be proportional to the energy deposited by the electron; it is also assumed that the energy deposited by a shower at a given altitude is almost independent of the energy spectrum of the shower electrons: this assumption has been confirmed by different studies [28, 29, 30].

Detectors to measure fluorescence light typically consists of an array of photomultipliers each one focused on a specific portion of the sky. In this way the longitudinal development of a shower can be directly measured, and the energy of the primary particle can be inferred from the total amount of fluorescence light detected. The main limitation of this technique is that it is usable only in dark moonless cloud free night, factor that reduces its duty cycle to about 10-15%.

The first complete experiment based on fluorescence detection was Fly's Eye [26] that started in 1982. The detector was constituted by 67 mirrors with 880 photomultipliers displaced over a semi-spherical surface.

To calculate the energy of the primary particle from the observed fluorescence light some effects have to be taken into account: for example not all the energy of the shower is deposited in the atmosphere since some particle

reach the ground and some other can't be detected.

Moreover, not all the light collected by a fluorescence detector is necessarily fluorescence light: also Cherenkov light must be taken into account. It is emitted, primarily in the forward direction, by electrons and positrons when their speed is greater than the speed of light in the atmosphere. Cherenkov light dominates the fluorescence light at emission angles θ , relative to the EAS axis, of less than 25° [26].

Fluorescence light production and detection is strongly influenced by the atmosphere, so accurate studies of its properties are required in order to obtain a reliable measurement of shower properties.

1.7 Effects of the atmosphere on the detection of EAS

It became apparent that the detection of air showers by fluorescent light could only be made successfully by operating in a different part of the earth where the weather would permit observing during four times as many hours per year, and where the lower atmosphere is free of the particles and aerosols that cause Mie scattering (Greisen, 1972)

The atmosphere plays multiple roles in the field of cosmic rays physics. In the previous sections it was explained that when UHECRs interact with atmosphere they produce a shower of particles and that the detection of this shower is the only way to detect cosmic rays of this huge energy; on the other hand we have seen that one of the techniques adopted to measure the energy of the primary and to study the development of the shower is to detect the UV light that is emitted by the nitrogen molecules of the atmosphere along the trace of the shower; at last the atmosphere attenuates this UV light during its travel toward the detectors affecting its correct measurement. These processes depend on the state variables and on the composition of the atmosphere, so an accurate monitoring of the properties of the atmosphere is needed to obtain a reliable knowledge of UHECRs features.

In the next paragraphs the main properties of the atmosphere will be introduced through a detailed description of the light attenuation processes.

1.7.1 Properties of the Atmosphere

The atmosphere is a gaseous layer that surrounds the earth, and, starting from its top toward the earth's surface, it can be separated in five main

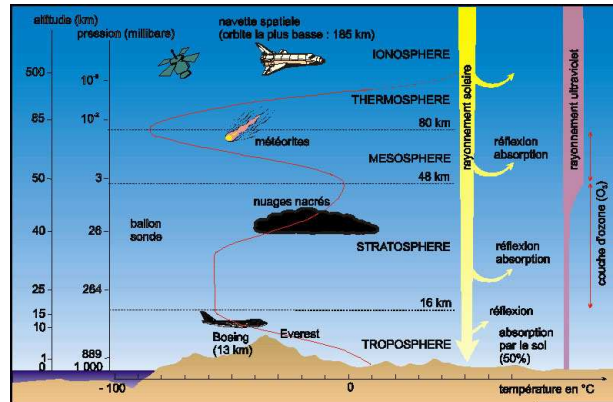


Fig. 1.8: The layers of Earth's atmosphere.

layers, characterized by different temperature gradient: the exosphere, the thermosphere, the mesosphere, the stratosphere, and the troposphere [31]. The lower part of the troposphere, called planetary boundary layer (PBL), is an important sublayer that is directly affected by the interaction with the surface.

The exosphere is that part of the atmosphere, the farthest from the surface, where molecules from the atmosphere can overcome the pull of gravity and escape into outer space. There are no definable boundaries to mark the limits of this layer: the lower level is usually taken as low as 500 km, while at heights of 800 km the atmosphere is still measurable, even if the molecular concentrations here are very small and are considered negligible.

The thermosphere is a relatively warm layer just below the exosphere where there is a significant temperature inversion. The few atoms that are present in the thermosphere (primarily oxygen) absorb ultraviolet (UV) energy from the sun, causing the layer to warm to temperatures that can exceed 500 K.

The mesosphere is the middle layer in the atmosphere where the temperature decreases with altitude. At the top of the mesosphere, air temperature reaches its coldest value, approaching 190 K. The mesosphere is bounded above by the mesopause, that has an average height of about 85 km, and below by the stratopause that extends up to 50 km.

The stratosphere is the layer between the troposphere and the mesosphere, characterized as a stable, stratified layer with a large temperature inversion throughout its depth. The stratosphere also contains the ozone layer that strongly absorbs UV light and prevents it from reaching the earth's surface at levels that could be dangerous to life. The absorption of UV light in this layer warms the atmosphere. This creates a temperature inversion

in the layer so that a temperature maximum occurs at the top of the layer, the stratopause. The stratosphere cools primarily through infrared emission from trace gases, and it is bounded above by the stratopause, where the atmosphere again becomes isothermal.

The troposphere is the lowest major layer of the atmosphere, where nearly all weather processes take place. In the troposphere, pressure and density rapidly decrease with height, as well as temperature that generally decreases at a constant rate of about $6.5^{\circ}\text{C}/\text{km}$. A characteristic of the troposphere is that it is well mixed. Air molecules can travel to the top of the troposphere and back down again in just a few days: this mixing encourages weather changes. Rain acts to clean the troposphere, removing particulates and many types of chemical compounds. The troposphere is bounded above by the tropopause, a boundary marked as the point at which the temperature stops decreasing with altitude and becomes constant; it has an average height of about 10 km. An important sublayer is the PBL that is the source of nearly all the energy, water vapor, and trace chemical species that are transported higher up into the atmosphere. The PBL represents the lowest 1–2 kms of the atmosphere that are directly affected by interactions with the earth's surface, particularly by the deposition of solar energy. Because of turbulent motion near the surface and convection, emissions at the surface are mixed throughout the depth of the PBL on timescales of an hour. Solar heating at the surface causes thermal plumes to rise, transporting moisture, heat, and particulates higher into the boundary layer. The plumes rise and expand adiabatically until a thermodynamic equilibrium is reached at the top of the PBL. The moisture transported by the thermal plumes may form convective clouds at the top of the PBL that will extend higher into the troposphere. The top of the PBL is characterized by a sharp increase in temperature and a sudden drop in the concentration of water vapour and particulates. As the air in the PBL warms during the morning, the height at which thermal equilibrium occurs increases. Thus the depth of the PBL increases from dawn to several hours after noon, after which the height stays approximately constant until sunset. The lowest part of the PBL, called the surface layer, comprises approximately the lowest hundred meters of the atmosphere and in windy conditions is characterized by a strong wind shear caused by the mechanical generation of turbulence at the surface. Convective air motions generate turbulent mixing inside the PBL above the surface layer, this tends to create a well-mixed layer between the surface layer at the bottom and, at the top, the entrainment zone, where the potential temperature and humidity as well as trace constituents are nearly constant with height. The entrainment zone is the part of the troposphere between the highest thermal plume tops and deepest parts of the sinking free air.

The bulk of air shower takes place in the lowest 20-25 km of the atmosphere, so, up to this height, the profile of atmospheric variables, such as temperature, pressure and density, and particulate concentrations must be known or estimated. Indeed interaction of cosmic rays in the atmosphere are described in dependence of the amount of matter trasversed, the atmospheric depht X , that can be calculated by integrating the air density $\rho(h)$:

$$X_{slant}(h_0) = \int_{h_0}^{\infty} \rho(h)dh \quad (1.9)$$

Different studies have shown that the altitude profile of $X(h)$ in average varies by $\sim 5 g cm^{-2}$ on successive nights, with extreme daily variation value of $20 g cm^{-2}$, variations that could introduce significant biases into the determination of the atmospheric depth of the shower maximum, X_{max} [32]. Moreover yields of light from the Cherenkov and fluorescence emission depends on the atmospheric variables. Cherenkov light emission depends only on the refractive index of the atmosphere $n(\lambda, p, T)$, so the dependence on pressure and temperature can be estimated analytically and weather effects are relatively simple to incorporate in shower reconstructions. The fluorescence yield suffers of other weather effects whose estimation need more complex experimental measurements. For example, the cross section of collisional quenching is function of temperature, pressure and umidity of the atmosphere, and should be determined via laboratory measurements [33].

Daily informations about atmospheric state variables, as temperature and pressure, that are useful to evaluate molecular air density, can be obtained through balloon measurements, or using data from global models like the Global Data Assimilation System (GDAS) [34], while the case of particulate, microscopic solid or liquid matter suspended in the earth's atmosphere, is more complex. The size and chemical composition of particulates and, thus, their optical properties may change quickly in time and this makes it difficult to characterize even average conditions, so hourly measurements are needed. The particulate concentrations are 3–10 times greater in planetary the boundary layer than they are in the free troposphere, so the sharp drop of these parameters is often used as a measure of the height of the PBL.

1.7.2 Light Attenuation in the Atmosphere

Light emitted by a source in the atmosphere is attenuated along a path toward an observer due to absorption and scattering with molecules and aerosols. In scattering processes a portion of the incoming light is dissipated in all directions with an intensity that depends, for a given angle, on the

physical characteristics of the scatterers within the scattering volume. The intensity of light absorption depends on the presence, along the path of the emitted light, of atmospheric absorbers, such as carbonaceous particulates, water vapour, or ozone, and results in a change in the internal energy of the molecular or particulate absorbers.

The intensity of a light source $I(0, \lambda)$ decreases to the value $I(\lambda)$ after the light has passed through a layer H ; the ratio of these values defines the optical transmission coefficient T of the layer H .

$$T(H, \lambda) = \frac{I(\lambda)}{I(0, \lambda)} \quad (1.10)$$

Introducing the *optical depth* of the path $(0, H)$ as $\tau(H, \lambda)$, the transmission coefficient T can be estimated using the Beer–Lambert–Bouguer’s law which describes the total extinction of a light beam in a turbid heterogeneous medium.

$$T(H, \lambda) = e^{-\tau(H, \lambda)} = e^{-\int_0^H \alpha(r) dr} \quad (1.11)$$

where $\alpha(r)$ is the extinction coefficient of the scattering or absorbing medium that represents the probability per unit path length that a photon will be scattered or absorbed.

The optical depth is a function of the orientation of a path within the atmosphere but, if the atmosphere in the path $(0, H)$ is horizontally uniform the range dependence of $\tau(r, \lambda)$ is reduced to the altitude $\tau = \tau(h, \lambda)$, and the transmission coefficient for a slant path elevated at an angle ϕ above the horizon is:

$$T(H, \lambda, \phi) = e^{-\tau(H, \lambda)/\sin \phi} \quad (1.12)$$

In an air fluorescence detector the amount of the isotropic fluorescence light emitted along the shower track (I_0) that is collected is [35]

$$I(H, \lambda) = I_0(H, \lambda)T(H, \lambda)(1 + f)\frac{d\Omega}{4\pi} \quad (1.13)$$

where f are high order corrections due to multiple scatterings and $d\Omega$ is the solid angle seen by the detector. The transmission coefficient $T(H, \lambda)$ can be factorized in two components that take into account singularly molecular ($T_{mol}(H, \lambda)$) and aerosol attenuation ($T_{aer}(H, \lambda)$).

Light extinction due to molecular scattering in the near UV (the range of fluorescence photons in the atmosphere) is primarily an elastic scattering process, since the Rayleigh scattering of light by molecular nitrogen and oxygen dominates inelastic scattering and absorption [36]. Moreover, while

O_2 is an important absorber in the deep UV, its absorption cross-section is effectively zero for wavelengths above 240 nm [37]. Ozone (O_3) molecules absorb light in the UV and visible bands, but O_3 is mainly concentrated in a high-altitude layer above the atmospheric volume used for air fluorescence measurements [37]. For these reasons in the following the term “attenuation” will refer only to processes that scatter light outside the field of view.

Molecular optical depth - Rayleigh Scattering

The amount of scattering for a volume of gas, characterized by the total Rayleigh volume-scattering coefficient $\alpha(\lambda, h)$ is given by the product of the total Rayleigh cross-section per molecule, σ , and the molecular number density N at a given pressure and temperature, or altitude, h :

$$\alpha(\lambda, h) = N(h)\sigma(\lambda) \quad (1.14)$$

The total Rayleigh cross section per molecule σ is given by the formula:

$$\sigma(\lambda) = \frac{24\pi^3(n^2 - 1)^2}{\lambda^4 N_s^2 (n^2 + 2)^2} \cdot F_k(\lambda) \quad (1.15)$$

where n is the refractive index for air at λ , N_s is the molecular number density for standard air ($N_s = 2.547 \cdot 10^{25} m^{-3}$ at $T = 288.15K$, $P = 101325Pa$) and F_k is the King correction factor which accounts for the anisotropy of air molecules and is a function of the polarization factor ρ_n ,

$$F_k(\lambda) = \left(\frac{6 + 3\rho_n}{6 - 7\rho_n} \right) \quad (1.16)$$

The intensity of molecular scattering is proportional to λ^{-4} , therefore the atmospheric molecular scattering is negligible in the infrared region of the spectrum and dominates in the ultraviolet region; but the dependence of the King correction factor on the wavelength shifts the wavelength dependence of $\alpha(\lambda, h)$ in the range 300 nm - 400 nm from the classical behaviour λ^{-4} to $\lambda^{-4.2}$.

For unpolarized radiation the angular distribution of the light scattered by air is given by the molecular phase function P :

$$P_{mol}(\theta) = \frac{3}{16\pi}(1 + \cos^2 \theta) \quad (1.17)$$

The molecular phase function is symmetric and has the same value $3/8\pi$ for light scattered in forward and backward direction.

Aerosol optical depth - Mie Scattering

Atmosphere is mainly composed by molecules but contains a great variety of aerosols, such as dust, ice crystals, fog or clouds. Aerosols dimensions span approximately from $0.01\mu m$ to a few mm . Rayleigh scattering is inherent not only to molecules but also to particulates when their radius is smaller than the wavelength of the incident light, while the scattering properties change when the size of particulates is comparable or greater to it. The solution of the equations of scattering of light on aerosols, often called Mie scattering, is much complex and in general it is not possible to calculate the total aerosol extinction coefficient analitically. The intensity of light scattering by particulates depends upon the particulate characteristics, specifically, the geometric size and shape of the scattering particle, the refractive index of the particle, the wavelength of the incident light, and on the particulate number density, quantity that can change rapidly depending on the wind and weather conditions. The dependence on wavelength of the aerosol extinction coefficient is connected with the size of the scatterer and can be parametrized with the Ångström's law:

$$\alpha_{aer}(h, \lambda) = \alpha_{aer}(h, \lambda_0) \cdot \left(\frac{\lambda_0}{\lambda}\right)^\gamma \quad (1.18)$$

where γ is the Ångström coefficient.

Aerosol phase function has not also an analytical solution. For the purposes of air fluorescence detection it is sufficient an approximation of the light scattering distribution that in general is strongly peaked in the forward direction, reaching a minimum near 90° and having a small backscattering component. A reasonable approximation of the aerosol phase function is the Henyey-Greenstein function[38]:

$$P_{aer}(\theta) = \frac{1 - g^2}{4\pi} \cdot \left(\frac{1}{(1 + g^2 - 2g \cos \theta)^{3/2}} + f \frac{3 \cos^2 \theta - 1}{2(1 + g^2)^{3/2}} \right) \quad (1.19)$$

The first term accounts for forward scattering [39], the second describes the peak at larger θ ; the parameter $g = \langle \cos \theta \rangle$ measures the asymmetry of the scattering, and f describes the relative strength of the forward and backward peaks; both the parameters are observables that depend on local aerosol characteristics.

Chapter 2

The Pierre Auger Experiment

2.1 Description of the Observatory

The Pierre Auger Observatory is the largest cosmic rays observatory in the world[40]. It was designed to study UHECRs, from fraction of EeV to the highest energies ever observed (hundreds of EeV), with the aim to answer to all the questions that are still open in this research field. The Auger Observatory was designed to collect cosmic rays events at the highest energies with high statistic . The measurement of the properties of the extensive air showers allows the determination of the energy and arrival direction of each cosmic ray and also provide a statistical determination of the distribution of primary masses. The construction of the Pierre Auger Observatory started in 2002 and was completed in 2008. Nowadays the Pierre Auger Collaboration is composed of more than 500 members of 19 different countries. The Observatory, sited near Malargüe, in the Province of Mendoza, Argentina, started collecting data in January 2004 and is composed by:

- A surface detector (SD) of 1660 water Cherenkov detectors covering an area of 3000 km^2 [41];
- A fluorescence detector (FD) consisting in 24 telescopes placed in 4 sites disposed at the borders of the area occupied by the SD[42].

During last years the original design of the observatory was refined by the addition of other detectors:

- The *Infill*, a sub array, with 71 water Cherenkov detectors on a denser grid covering about 30 km^2 [43];
- 3 High Elevation Auger Telescopes (HEAT) dedicated to the fluorescence observation of lower energy shower [44];

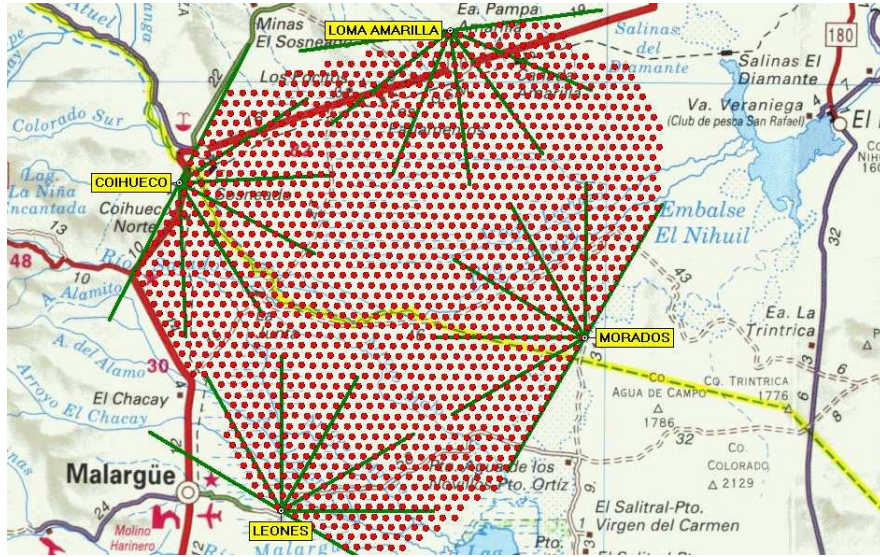


Fig. 2.1: Map of the Pierre Auger Observatory, Malargüe (Argentina): each red point represent a Cherenkov detector.

The Observatory includes also some system to test the detection of EAS using the radio emission of the electromagnetic cascade in the atmosphere:

- A sub array of 124 radio sensor (AERA - Auger Engineering Radio Array) working in the MHz range [45];
- A sub array of 61 radio sensor (EASIER - Extensive Air Shower Identification with Electron Radiometer) working in the GHz range [46];
- Two GHz imaging radio telescope, AMBER [47] and MIDAS [48].

2.1.1 Hybrid design

The essential feature of the Pierre Auger Observatory is its hybrid design: EAS are detected simultaneously by the Cherenkov detectors and by the fluorescence telescopes. The complementarity of these techniques provide important cross-checks and measurement redundancy.

Charged particles that reach the ground are sampled with the surface detector. The water-Cherenkov stations of the array are sensitive to both the electromagnetic and muonic components of the shower and measure the lateral and temporal distribution of the shower.

The SD has a duty cycle of 100% and thus provides uniform coverage in right ascension with a huge 3000 km^2 collecting area and has a unit efficiency

in the detection of the EAS with energy greater than 10^{18} falling on any part of the array, whatever primary particle initiates the shower. Another important property of the SD is that the quality of the measurements improves with the shower energy.

The fluorescence detector is used to image the longitudinal development of the shower in the atmosphere through the detection of the UV fluorescence light that is emitted isotropically by nitrogen molecules of the atmosphere. The FD collects data only during moonless nights of good weather, achieving a duty cycle which has increased from 12% during early years [49] up to $\sim 15\%$ at the present time.

Since fluorescence light production is proportional to the collisional energy deposit by the shower in the atmosphere, the technique provides a near-calorimetric method for determining the primary cosmic ray energy. Moreover, the depth at which a shower reaches maximum size, X_{max} , is observable in its longitudinal development: this is the most direct mass composition indicator. The detection of hybrid events (events measured by both FD and SD), allows a direct measurement of the energy with the FD that can be transferred to the surface array with its 100% duty factor.

However, the FD is not only a calibration tool: hybrid events are high quality data, and are especially useful for those studies that require more precise shower directions information than those available from the surface array only, and for studies where longitudinal profile measurements are vital. Moreover the hybrid data set provides a better understanding of the capabilities and the systematic uncertainties of both components.

An example of the synergy between the two techniques are the measurements of the cosmic ray energy spectrum for showers arriving with zenith angles smaller than 60° [7]. The SD observable chosen to estimate the primary energy is the signal measured in the water-Cherenkov detectors at 1000 m from the shower axis, $S(1000)$. Using the surface array alone the relationship between $S(1000)$ and the energy of the primary can only be found using cascade simulations. Since the necessary hadronic physics is unknown at the energies of interest, this method is not fully reliable and it is therefore not even practical to assign a reliable systematic uncertainty.

The use of a hybrid system provides a method to estimate the primary energy that is essentially free from simulations. The first step is to quantify the dependence of $S(1000)$ on the zenith angle. This is done using the “constant intensity” method [50], where the attenuation of the typical air shower with increasing atmospheric depth is mapped out using SD data alone. The conversion to primary energy is then achieved using hybrid events. The only simulation input to the determination of primary energy with the FD is the estimation of the small fraction ($\sim 10\%$) that goes into neutrinos and high-

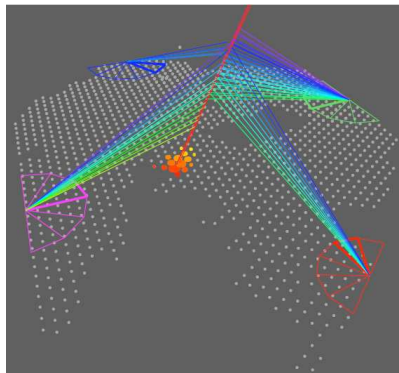


Fig. 2.2: Schematic view of an hybrid event.

energy muons that continue into the ground.

2.2 The Surface Detector: SD

The Surface Detector of the Pierre Auger Observatory consists of an array of 1660 water-Cherenkov detectors disposed on a triangular grid. Each station is 1500 m far from another, and the whole array covers approximately 3000 km^2 in the Argentine pampa. A surface detector station consists of a 3.6 m diameter and 1.2 m height water tank containing a sealed liner with a reflective inner surface. The liner contains 12000 liters of ultra-pure water. Cherenkov light produced by the passage of relativistic charged particles through the water is recorded by three 9 inch diameter Photonis XP1805 photomultiplier tubes. PMTs are placed on the surface of the liner at a distance of 1.20 m from the tank center axis and look downward into the water. The tank is also sensitive to high energy photons that interact with water producing electron-positron pairs.

Each surface detector station is equipped with a solar panel that provides an average power of 10 Watts for PMTs and electronics package consisting of a processor, a GPS receiver, a radio transceiver and a power controller [52]. A picture of a SD station is shown in figure 2.3.

The Cherenkov light recorded by a tank is measured in a unit termed *Vertical-Equivalent Muon*. A VEM unit is equal to the signal produced by a muon traversing the tank on a vertical trajectory. The conversion to units of VEM is done both to provide a common reference level between tanks and to calibrate against the detector simulations. Tanks are calibrated using atmospheric muons, whose signal is proportional to the path length of

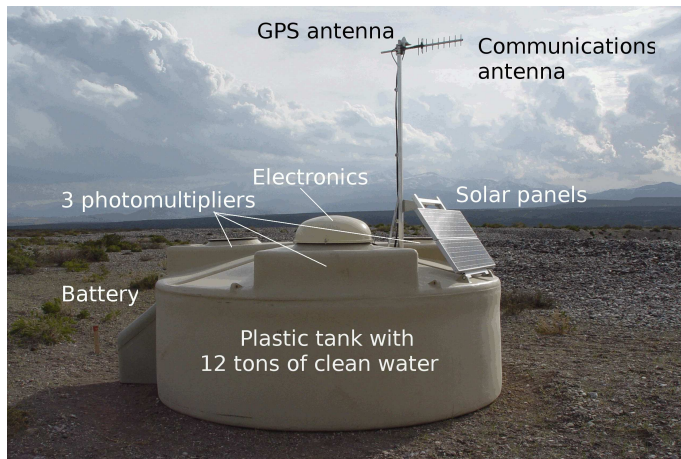


Fig. 2.3: Schematization of a surface detector station.

the particles within the tank. A test tank was used to calculate the relation between down-going vertical muons and the peak of the histogram obtained from omni-directional muons. Each tank is calibrated matching the photomultipliers gain to obtain the expected trigger rate over a given VEM threshold. This procedure allows to calibrate tanks with a precision of 5%. Each detector station has a two level trigger, a hardware implemented T1 and a software T2 [53]. Front-end implements two different first level triggers (T1). A *threshold trigger* (ThT) requires that the signal on some PMTs exceeds a given value defined in terms of VEM, typically 1.75 VEM on a single 25 ns time bin. This trigger is designed to detect fast signals associated to the muons of very inclined showers.

The second condition for T1 is the *time over threshold trigger* (ToT): it requires that the signal in 13 FADC bins out of a window of 120 bins ($3\mu s$) are above a value of 0.2 VEM; it is efficient to select small signals away from the core of showers at the tail of the lateral distribution. The rate of T1 is about 100 Hz but the second level trigger T2 reduces the trigger rate to less than 20 Hz, so as not to saturate the radio bandwidth available. All ToT are promptly promoted to T2, while ThT requires a condition of 3.2 VEM in coincidence for the 3 PMTs to be promoted. Trigger signals that satisfy T2 requirements are sent to the central data acquisition system (CDAS) of the observatory.

At CDAS trigger signals are further selected: an event trigger (T3) requires a number of contiguous stations triggered. The number of stations triggered sets the lower energy threshold. Only groups of at least 3 stations are examined for spatial coincidence, and, typically, four stations are required for

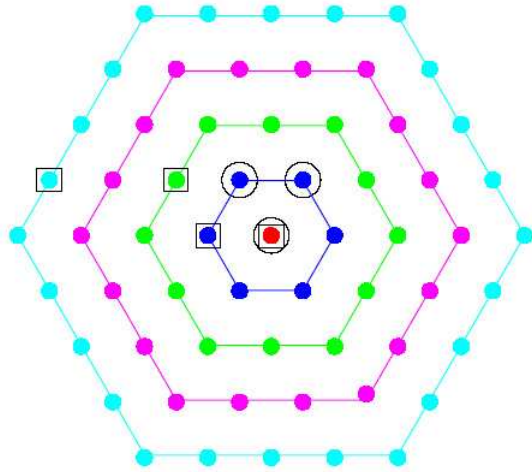


Fig. 2.4: Four hexagons, containing stations, are illustrated around a central surface station, for a portion of an ideal array. Two examples of the topology of triggers are shown: a 4-fold coincidence in which the triggered stations are identified by squares, and a 3-fold coincidence identified by circles.

a threshold of $10^{19}eV$.

Physical events are selected by a physical trigger, the fourth trigger level (T4). Its requirements depend on the number of triggered stations, and to apply the main trigger condition, the acquisition system defines concentric hexagons centered in each station (see Fig.2.4). Signals of three tanks that satisfy the ToT conditions pass T4 if one of them have one of its closest neighbours and one of its second neighbours triggered. The 90% of events selected by the so called $3ToT$ are physical events. It is very efficient for vertical showers.

Horizontal showers, which produce fast signals with a wide-spread topological patterns are selected when signals of four tanks pass the T2 trigger in coincidence. In this case it is required that one tank must be as far as 6 km away from others within an appropriate time window.

2.3 The Fluorescence Detector: FD

The Fluorescence Detector of the Pierre Auger Observatory consists of 24 telescopes which overlook the SD array from four sites: Los Leones, Los Morados, Loma Amarilla and Coihueco (see Fig. 2.1). Each FD site, named “eye” holds six telescopes: a scheme of an FD site is shown in Fig. 2.5. A

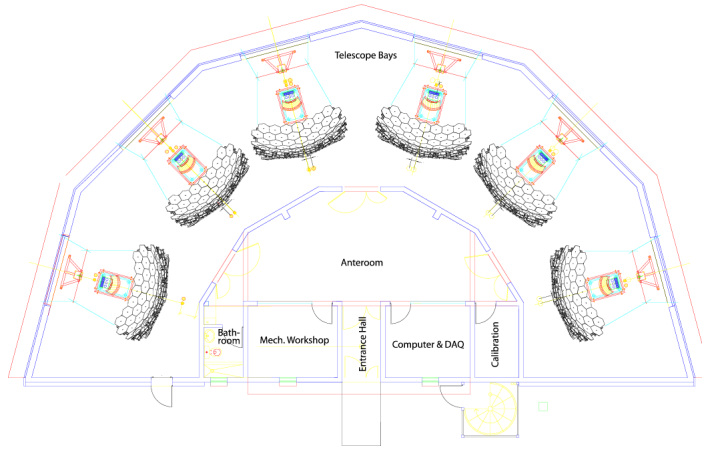


Fig. 2.5: Scheme of an FD station: each *eye* is divided in six “*bays*” each housing a telescope.

single telescope has a field of view of $30^\circ \times 30^\circ$ in azimuth and elevation and a minimum elevation of 1.5° above the horizon. The telescopes face towards the interior of the array so that the combination of the six telescopes provides 180° coverage in azimuth [55].

The basic elements of the optical system in each FD telescope are a filter at the entrance window, a circular aperture, the diaphragm, a corrector ring, a mirror and a camera with photomultipliers (see Fig.2.6).

The telescope design is based on Schmidt optics because it reduces coma aberration of large optical system and partially corrects spherical aberration. Nitrogen fluorescence light, emitted isotropically by an air shower, enters through a circular diaphragm of 1.1 m covered with a filter glass window. The filter, made of Schott MUG-6 glass [56], absorbs visible light while transmitting UV photons from ~ 290 nm up to ~ 410 nm wavelength, which includes almost all of the nitrogen fluorescence spectrum.

The size of the aperture is optimized to keep the 90% of the light from a distant point source, located anywhere within the FOV of a camera, falls into a circle of 15 mm.

The outer part of the aperture holds a segmented *corrector ring*, a simplified annular lens, which corrects spherical aberration and eliminates coma aberration. It has inner and outer radii of 850 and 1100 mm, respectively. The light is collected by a spherical mirror of 3.4 m radius of curvature and focused onto a spherical focal surface with radius of curvature 1.7 m. The mirror is segmented in two different configurations, one is a tessellation of 36 rectangular anodized aluminum mirrors of three different sizes; the other is a structure of 60 hexagonal glass mirrors (with different shapes and sizes)

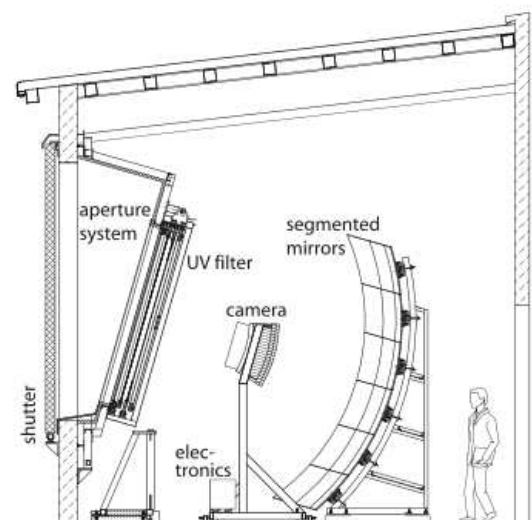


Fig. 2.6: Schematic view of an FD telescope.

with vacuum-deposited reflective coatings. The average reflectivity of cleaned mirror segments at $\lambda = 370$ nm is more than 90%.

The light detecting system consists in a matrix of 440 hexagonal photomultiplier tubes, model XP3062 [57] manufactured by Photonic. Specific characteristics are [58]:

1. non-uniformity of the response over the photocathode within 15%: the light spot size for an infinity distant point source is about one-third of the pixel size, so the uniformity is not a critical parameter.
2. a nominal gain 5×10^4 .
3. spectral response: the *PMT* average quantum efficiency is 0.25 in the wavelength range of interest.
4. linear response: it is better than 3% over a dynamic range of at least 10^4 for signals of $1 \mu s$.
5. longevity: the integrated anode charge corresponding to the half life of the tube is not less than 500 C with an half life of ~ 50 years.
6. single photoelectron: even if it is not necessary, *PMT* have a single photoelectron detection capability, which guarantees a good resolution for the tube.

PMTs are arranged in a matrix of 22 rows by 20 columns, with a side to side distance of 45.6 mm, corresponding to an angular size of 1.5° . To maximize light collection and guarantee a sharp transition between adjacent pixels, the hexagonal PMTs are complemented by light collectors. The pixel light collector is realized by a combination of six plastic “Mercedes stars”. The geometrical structure of the light collector for one pixel is shown in Fig. 2.7: a Mercedes star has three arms, each arm is positioned on a pixel vertex. Every pixel is then surrounded by six Mercedes. The length of an arm is approximately half of the pixel side length, and its section is an equilateral triangle with base length of 9.2 mm.

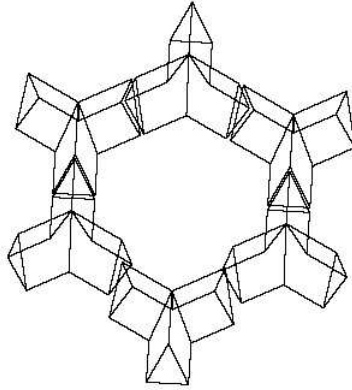


Fig. 2.7: Geometrical structure of the light collector for one pixel is shown. The Mercedes stars are made of plastic material covered by aluminized Mylar™ foils.

Each FD camera is read out by one front-end sub-rack and an associated PC. The front-end electronics contain 20 Analog Boards, and each one receives data from a column of 22 PMT channels.

FD data registration is regulated by a four levels trigger system.

The First Level Trigger (FLT) selects pixels whose signal is above a fixed threshold. The threshold is dynamically adjusted to maintain a pixel trigger rate of 100 Hz. When the sum of the ADC samples in certain time bins exceeds the threshold, a pixel trigger is generated.

The Second Level Trigger (SLT) evaluates the chronological sequence of pixel that passed the FLT to individuate signals that are compatible with a cosmic ray track on the camera.

The selection criterion is based on the comparison of the signal with the five fundamental types of pattern regarded as straight track segments shown in figure 2.8 and with all the pattern obtained by their rotation and reflexion (in total 108 patterns). SLT requires at least 4 out of 5 pixels to be over

threshold. This request is motivated by the possibility that some tracks will not pass through every pixel center, and therefore some PMTs along the track may not record enough light to trigger.

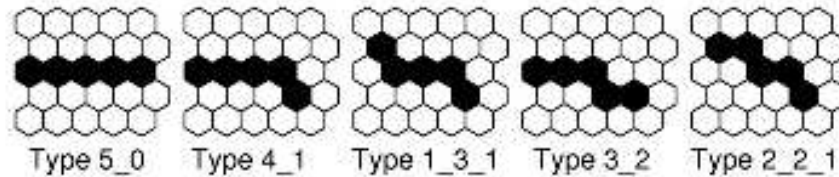


Fig. 2.8: Basic valid topologies for T1 trigger level.

The Third Level Trigger (TLT) is a software trigger that evaluates the length and the space-time features of a track, in order to discard sequences generated by pixels that are spatially but not temporally correlated.

The last trigger is the T3 that is used to calculate a preliminary shower direction and ground impact time. T3 trigger is sent to the CDAS and then used as external trigger for the SD, in order to record hybrid events at low energies (below $3 \cdot 10^{18} eV$) where the array is not fully efficient and would not often generate an independent trigger.

2.3.1 FD Calibration

The reconstruction of air shower longitudinal profiles requires the conversion of an ADC count to a light flux for each pixel that receives a portion of the signal from the shower. It is therefore necessary to evaluate the response of each pixel to a given flux of incident photons from the solid angle covered by that pixel taking into account the effects of aperture projection, optical filter transmittance, mirror reflectivity, pixel light collection efficiency and area, cathode quantum efficiency, PMT gain, pre-amplifier and amplifier gains, and digital conversion.

A calibrated light source, the “drum”, is used to perform the absolute calibration of the fluorescence detectors. The drum is a cylinder 1.4 m deep with a 2.5 m diameter, and when mounted at the exterior of the FD apertures, it provides the same flux of light to each pixel (see Fig. 2.9). The known flux from the light source and the response of the acquisition system give the required calibration for each pixel. Use of the drum for gain adjustment and calibration provides a known, uniform response for each pixel in each camera of the FD detector. The average response of the FD is approximately 5

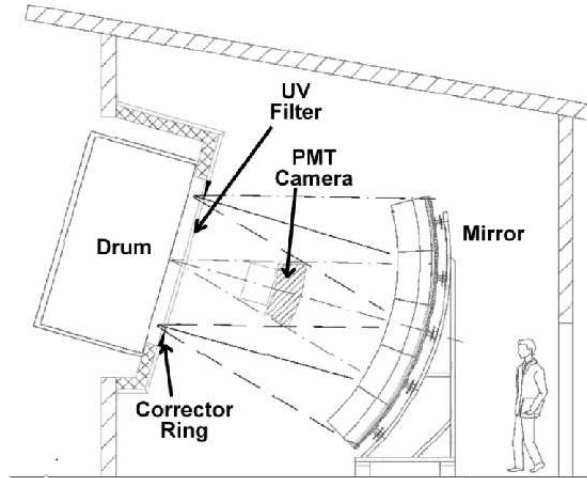


Fig. 2.9: A schematic showing the “drum” calibration of an FD telescope.

photons/ADC bin.

In addition to the absolute calibration a relative calibration of the PMTs is performed before and after each night of data taking. This relative calibration is used to track both short and long term changes in detector response. Three light sources (A, B, and C) for each camera are used to monitor different groups of detector components. Light is distributed through optical fibers, from permanently installed light sources (see Fig. 2.10). The A source is a 470 nm LED, the B and C light sources are xenon flash lamps. The relative FD response has been measured at wavelengths of 320, 337, 355, 380 and 405 nm, defining a spectral response curve which has been normalized to the absolute calibration.

2.4 Event reconstruction

As widely explained the Pierre Auger Observatory uses two different techniques to detect, and then reconstruct, a shower event. SD reconstruction is performed for events with at least 3ToT stations, and FD reconstruction can be performed for events detected by the fluorescence detector. The combination of both technique, the hybrid reconstruction, improves the geometry determination and takes advantages of the calorimetric measurement of the energy from FD.

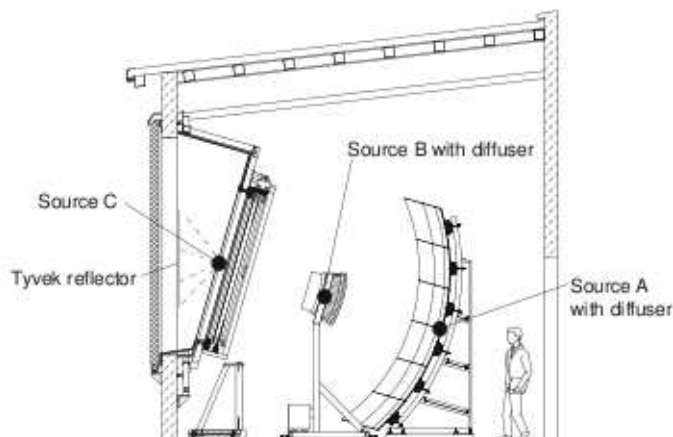


Fig. 2.10: A schematic showing positions of light sources for three different relative calibrations of the telescope.

2.4.1 FD Event reconstruction

In the FD, cosmic ray showers are detected as a sequence of triggered pixels in the camera. The reconstruction of an event can be divided in *geometrical* and *profile* reconstruction. The first step of the geometrical reconstruction is the determination of the shower-detector plane (SDP). The SDP is the plane that includes the location of the eye and the line of the shower axis (see Fig. 2.11). Next, the timing information of the pixels and the viewing angle of the pixels projected into the SDP are used for reconstructing the shower axis within the SDP.

Two parameters characterize the shower axis: the perpendicular distance, R_p from the camera to the track, and the angle χ_0 that the track makes with the horizontal line in the SDP. From these parameters the arrival time $t(\chi_i)$ of light to the pixel i can be measured:

$$t(\chi_i) = t_0 + \frac{R_p}{c} \cdot \tan\left(\frac{\chi_0 - \chi_i}{2}\right) \quad (2.1)$$

where t_0 is the time when the shower front on the axis passes the point of closest approach R_p to the camera and χ_i is the angle between the pointing direction of each pixel and the horizontal line.

To determine the three free parameters t_0 , R_p and χ_0 the minimum of

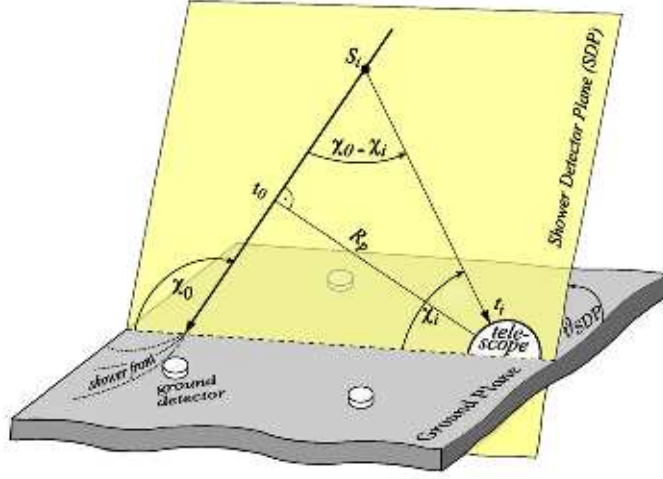


Fig. 2.11: A schematic of the geometrical shower reconstruction from the observables of the fluorescence detector.

the function

$$\chi^2 = \sum_i \frac{(t_1 - t(\chi_i))^2}{\sigma(t_i)^2} + \frac{(t_{SD} - t(\chi_{SD}))^2}{\sigma(t_{SD})^2} \quad (2.2)$$

where t_{SD} is the additional SD station time with its uncertainty $\sigma(t_{SD})$, and χ_{SD} is the angle at which the shower front hits the station.

Shower reconstruction using only FD data can achieve good accuracy, but is limited when the measured angular speed $d\chi/dt$ does not change much over the observed track length. In this case there is a family of possible (R_p, χ_0) axis solutions. The fit degeneracy can be broken by combining the timing information from the SD stations with that of the FD telescopes. This is called the hybrid reconstruction.

Once the geometry of the shower is known, the light collected at the aperture as a function of time can be converted to energy deposit at the shower as a function of slant depth. For this purpose, the light attenuation from the shower to the telescope needs to be estimated and all contributing light sources need to be disentangled: fluorescence light, direct and scattered Cherenkov light and multiple-scattered light. Since the Cherenkov and fluorescence light produced by an air shower are connected to the energy deposit by a linear set of equations, the shower profile is obtained by an analytic linear least square minimization. The longitudinal energy deposit profile

and its maximum $\left(\frac{dE}{dX}\right)_{max}$ at depth $X = X_{max}$ are estimated by fitting a Gaisser–Hillas function [59] to the signal produced by the FD cameras after folding it with the light yields, atmospheric transmission, lateral distributions and detector response. .

$$f_{GH}(X) = \left(\frac{dE}{dX}\right)_{max} \left(\frac{X - X_0}{X_{max} - X_0}\right)^{\frac{X_{max}-X_0}{\lambda}} e^{-\frac{X_{max}-X}{\lambda}} \quad (2.3)$$

The calorimetric energy of the shower is obtained by integrating Eq. 2.3. From Monte Carlo shower simulations it is possible to calculate the “invisible energy” carried away by neutrinos and high energy muons, so the total energy of the shower can be estimated [60]. An example of the measured light at aperture and the reconstructed light contributions and energy deposit profile is shown in Figs. 2.12 and 2.13.

2.4.2 SD Event reconstruction

The SD is able to reconstruct the energy and the arrival direction of the cosmic rays producing air showers from the sizes and times of signals registered from individual SD stations. The reconstruction is performed by sampling both the arrival times and the deposited signal in the detector array: it allow to determine the shower geometry, i.e. the shower core, the arrival direction of the incident cosmic ray, and the shower size.

A first approximation for the arrival direction of the primary particle is obtained by fitting the start times of the signals, t_i , in each triggered SD stations to a plane front. When enough stations are triggered the start times are fitted by a more detailed concentric-spherical model, that describes the evolution of the shower front with a speed-of-light inflating sphere (see Fig. 2.14):

$$c(t_i - t_0) = |\vec{x}_{sh} - \vec{x}_i| \quad (2.4)$$

where \vec{x}_i are positions of the stations on the ground, \vec{x}_{sh} is a virtual origin and t_0 a start-time of the shower development.

The SD detects only a sample of the particles arriving at ground therefore a fit of the lateral distribution has to be performed to obtain the impact point of the air showers on the ground. The function used to describe the lateral distribution of the signals on ground is a modified Nishimura-Kamata-Greisen (NKG) function [61]

$$S(r) = S(r_{opt}) \left(\frac{r}{r_{opt}}\right)^\beta \cdot \left(\frac{r + r_1}{r_{opt} + r_1}\right)^{\beta+\gamma} \quad (2.5)$$

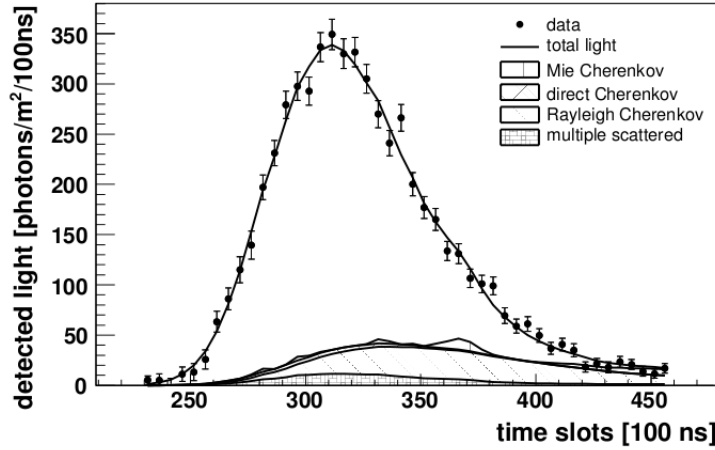


Fig. 2.12: Example of the shower light detected by the FD with an estimation of the different light components.

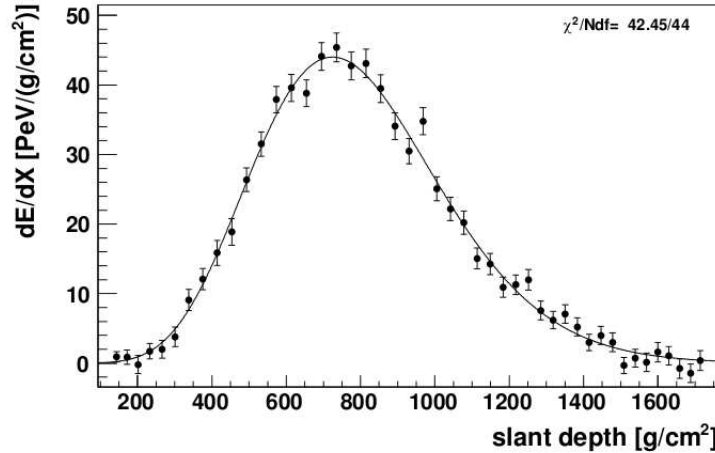


Fig. 2.13: Example of a reconstructed shower profile.

where r_{opt} is the optimum distance, $r_1 = 700$ m and $S(r_{opt})$ is an estimator of the shower size used for an energy assignment. For the SD array with station spacing of 1.5 km the optimum distance is $r_{opt} = 1000$ m and the shower size is thus $S(1000)$ [62]. The parameter β depends on the zenith angle and shower size. The uncertainties on the $S(1000)$ evaluation have three sources: a systematic uncertainty due to assumptions on the shape of the lateral distribution function (LDF), a statistical uncertainty due to the finite number of particles producing signal in a given SD station and the

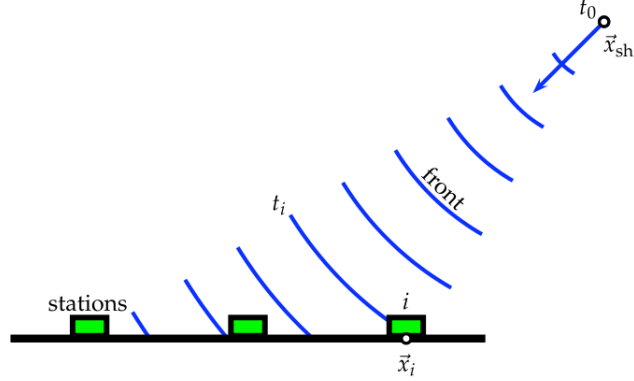


Fig. 2.14: Schematic representation of the evolution of the shower front.

limited dynamic range of the signal detection, and an uncertainty due to shower-to-shower fluctuations. The first two terms contribute a factor that varies from 6% to 20% depending on the energy, the contribution of the last is about 10%.

The shower arrival direction is obtained from the virtual shower origin of the geometrical reconstruction and the shower impact point on the ground (\vec{x}_{gr}) obtains from the LDF reconstruction:

$$\hat{a} = \frac{\vec{x}_{sh} - \vec{x}_{gr}}{|\vec{x}_{sh} - \vec{x}_{gr}|} \quad (2.6)$$

The shower energy estimation depends on the value of $S(1000)$. It decreases with the zenith angle θ due to the attenuation of the shower particles and geometrical effects. The shape of the attenuation curve is calculated using the Constant Intensity Cut (CIC) method [50] that fits the attenuation curve with a third degree polynomial function f_{CIC} (see Fig. 2.15). The median angle, $\theta = 38^\circ$, is taken as a reference point to convert $S(1000)$ to S_{38} , the signal a particular shower with size $S(1000)$ would have produced as it arrived at $\theta = 38^\circ$:

$$S_{38} \equiv S(1000)/f_{CIC}(\theta) \quad (2.7)$$

The high quality hybrid events are used to estimate the energy of the primary particle producing the air showers recorded with the SD. For the FD events it is required an accurate fit of the longitudinal profile to the Gaisser-Hillas function, a zenith angle less than 60° , X_{max} must be contained within

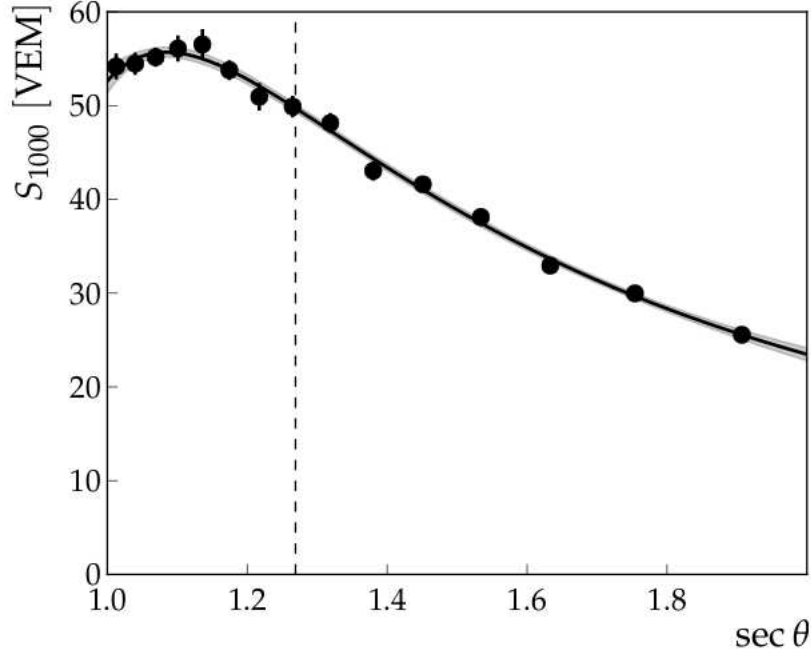


Fig. 2.15: Attenuation curve described by a third degree polynomial in $x = \cos^2\theta - \cos^2\bar{\theta}$ where $\theta = 38^\circ$.

the telescope field of view and measured with an accuracy better than $40 \text{ g} \cdot \text{cm}^{-2}$, and the uncertainty on the reconstructed FD energy is required to be less than 18%. Finally a correlation between S_{38} and E_{FD} is obtained from a maximum likelihood method which takes into account the evolution of uncertainties with energy. The relation between S_{38} and E_{FD} is described by a power-law function:

$$E_{FD} = A(S_{38}/VEM)^B \quad (2.8)$$

where $A = (1.90 \pm 0.05) \times 10^{17} \text{ eV}$ and $B = 1.025 \pm 0.007$ are the parameters resulting from the data fit of events accumulated until December 2012 [51]. Result of the fit is shown in Fig. 2.16. Using the FD energy resolution of 7.6%, the resulting SD energy resolution with its statistical uncertainty is $\sigma_{E_{SD}}/E_{SD} = (16 \pm 1)\%$ at the lower energy and $(12 \pm 1)\%$ at the highest energies. The energy range of the surface detector has extended down to $3 \times 10^{17} \text{ eV}$ using the events recorded by the 750 m array.

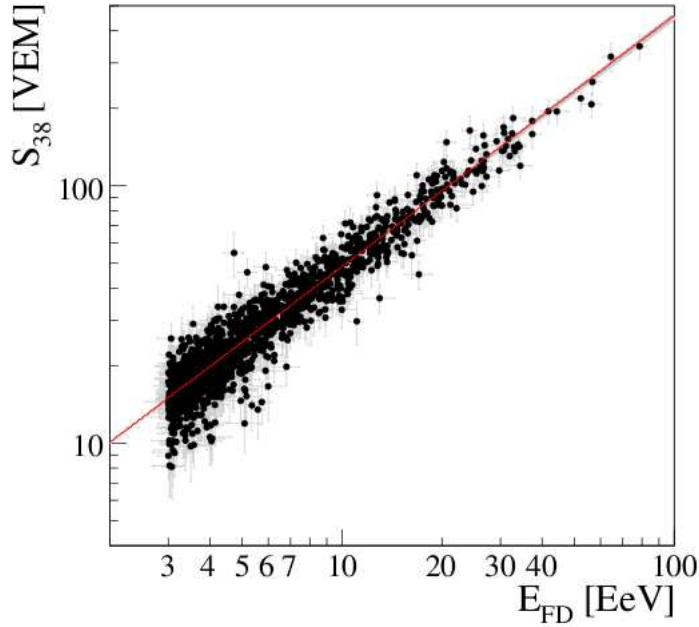


Fig. 2.16: Correlation between S_{38} and E_{FD} .

2.5 The Offline Software Framework

The official software framework of the Pierre Auger Observatory is the Offline. It is implemented in C++ and is designed to support a variety of distinct computational tasks necessary to analyze data gathered by the observatory [63]. Specifically, the software supports simulation and reconstruction of events using surface, fluorescence and hybrid methods, as well as simulation of calibration techniques and of lasers, and other ancillary tasks such as data preprocessing.

The framework comprises three principal parts:

- a collection of processing *modules* which can be assembled and sequenced through instructions provided in an XML file [79];
- an event data model through which modules can relay data to one another and which accumulates all simulation and reconstruction information;
- a detector description which provides a gateway to data describing the

configuration and performance of the observatory. The atmosphere is treated as part of the detector and data from atmospheric monitoring devices are stored in MySQL databases.

2.6 Highlights of science results

2.6.1 All-particle spectrum

The all-particle spectrum of the Auger Observatory is shown in Fig. 2.17 [64]: it results from the combination of the energy spectra derived from the array with 1500 m spacing (including both vertical and incline showers), the infill array of 750 m station separation, and the hybrid data set. The total number of events entering the spectrum is about 130000, the statistics at high energy is dominated by the surface detector array. This unprecedented statistical accuracy allows to clearly identify two features in the energy spectrum, the *ankle* and a cut-off at the highest energy. The ankle appears at ~ 5 EeV, at this energy the spectral index changes from -3.23 ± 0.07 to -2.63 ± 0.04 . Above 20 EeV the spectrum starts to deviate from a simple power law and a flux suppression is observed. The significance of the cut-off is more than 20σ , however its origin, as that of the ankle, is yet to be determined.

These features can originate from interactions of the cosmic rays with the intergalactic radiation field along the path from their sources to the Earth. For example the ankle can be due to the electron-positron pair production from protons interacting with the CMBR, and the cut-off to the pion production that occurs in the same process. They can also originate from the source distributions and their acceleration characteristics, in this case the ankle could sign the transition from a galactic dominated cosmic ray component to an extra-galactic dominated one, while the cut-off would directly reflect the maximum energy reachable by the sources themselves. In the right panel of Fig. 2.17 the data are compared to two model scenarios that inject either only proton or iron primaries.

2.6.2 Mass composition

The determination of the composition of UHECRs is performed by measuring the depth of shower maximum, X_{max} , the muon production depth, and rise-time asymmetry of the shower disk at ground.

Results of the analysis of the X_{max} distribution show a substantial change in the proton fraction across the entire energy range (see Fig. 2.18); proton fraction rises to over 60% around the ankle region and then drops to near

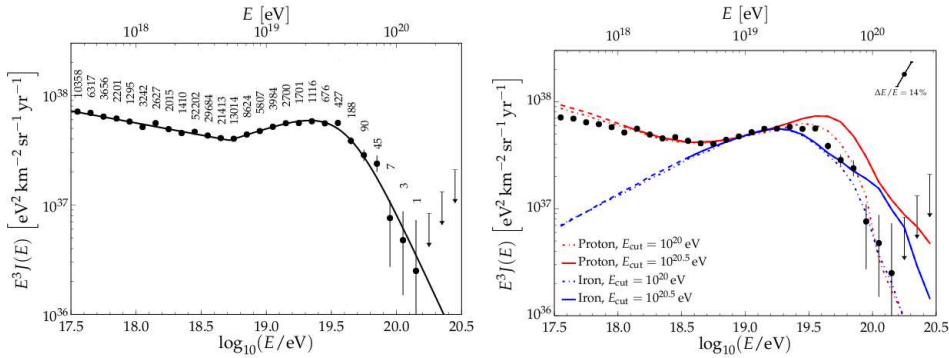


Fig. 2.17: All-particle flux measured with the Auger Observatory. Left: The Auger data are shown with an empirical fit and in addition the number of events is given for each energy bin. Right: The energy spectrum is compared to predictions for the idealized scenario of homogeneously distributed sources injecting either only proton or iron primaries.

zero just above 10^{19} eV with a possible reappearance at higher energies. The proton fraction in ankle region is surprisingly large and this behavior contrasts with interpretation of the ankle as a transition from galactic to extragalactic cosmic rays. In order to accommodate a proton-dominated scenario for energies above 10^{18} eV the hadronic interaction models would need to be modified considerably [65].

2.6.3 Photon and neutrino limits

Top-down scenario for sources of UHECRs predict large secondary fluxes of photons and neutrinos. The limits on the fluxes of photons and neutrinos obtained from the Pierre Auger Observatory are shown in Fig. 2.19 [66, 67, 68].

The directional photon flux upper limit from a point source is the limit on the number of photons from a given direction divided by the directional acceptance from the same target at a confidence level of $\text{CL} = 95\%$. The current flux limits strongly disfavor top-down models.

The photon flux limits have further far-reaching consequences by providing important constraints on theories of quantum gravity involving Lorentz invariance violation (LIV) [69]. Similarly, observing cosmogenic neutrinos would allow to put constraints on LIV in the neutrino sector.

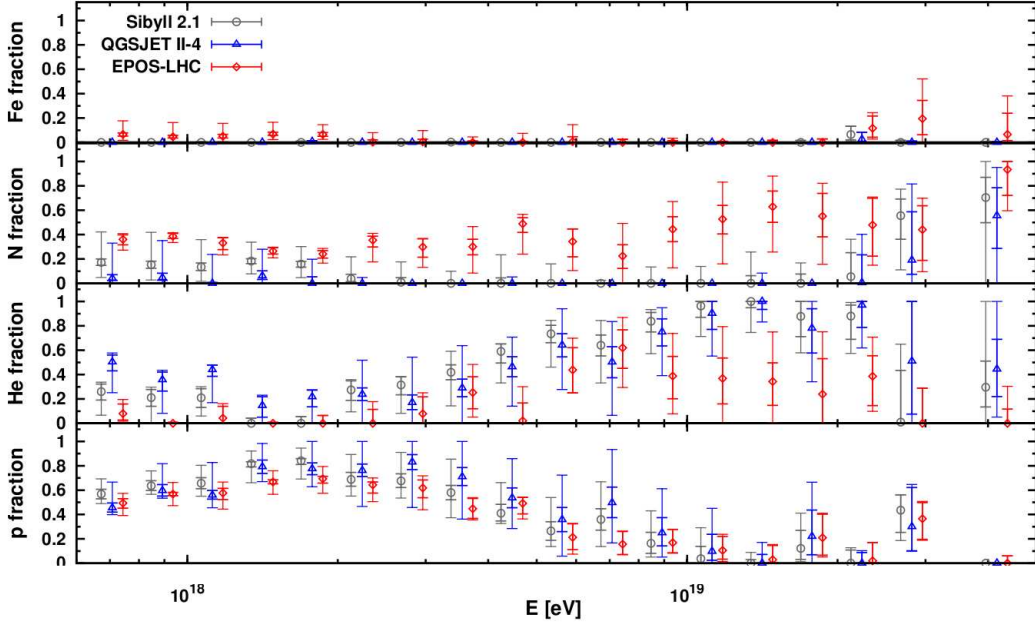


Fig. 2.18: Fitted fraction for the scenario of a complex mixture of protons, helium nuclei, nitrogen nuclei, and iron nuclei [65].

2.6.4 Arrival direction distribution

The arrival direction distribution is one of the key observables to search for the transition from galactic to extragalactic cosmic rays and for source regions of UHECRs.

An anisotropy in the distribution of cosmic rays with energy above about 57 EeV was reported with a confidence level of 99% using data collected in the period 2004 - 2006 [74]. The analysis was based on the finding of a correlation within a small angular separation (3.1°) between the UHECRs arrival directions and the locations of nearby active galaxies (within 75 Mpc) in the Véron-Cetty and Véron (VCV) catalog [75].

The analysis was repeated with a larger data set and the correlation fraction was found to be lower. With an enlarged data set the correlating fraction was found to be lower although still $\sim 3\sigma$ above expectations from an isotropic distribution [76].

Latest results suggest high degree of isotropy in the distribution of UHECRs: if the actual source distribution were anisotropic, these results could be understood for instance as due to the large deflections caused by the inter-

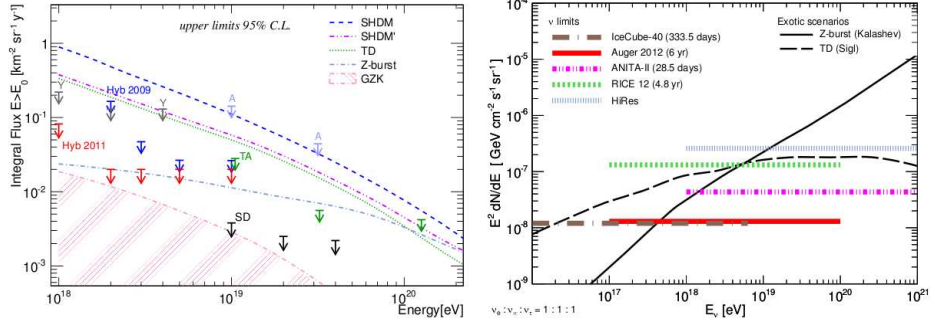


Fig. 2.19: Limits on the flux of photons (left) and neutrinos (right) obtained from the Pierre Auger Observatory. The data are shown together with the current limits from other experiments and some examples of predicted fluxes [70, 71, 72, 73].

vening magnetic fields if a large fraction of the CRs in this energy range were heavy, as is indeed suggested by mass-composition studies [65]. Alternatively, it could also be explained in a scenario in which the number of individual sources contributing to the CR fluxes is large.

2.6.5 Air shower and hadronic interaction physics

The depth of maximum is directly related to the first interaction of the cosmic rays in the atmosphere. Based on this correlation the proton-air cross section has been measured at 57 TeV c.m.s. energy using hybrid data of the Auger Observatory [77]. Applying the Glauber approximation [78] this cross section can be converted to an equivalent (inelastic) proton-proton cross section. The cross section is found to be consistent with model extrapolations that describe the LHC data (see Fig. 2.20).

The number of muons in an air shower is sensitive to hadronic particle interaction in the shower cascade: several analyses were performed to extract a muon size parameter from the hybrid or SD data set of Auger. All the analyses indicate that current hadronic interaction models predict muon size that are smaller (by at least 20%) than observed in the data, unless one assumes that the data is composed of pure iron which is in contradiction, according to the same models, with the observed X_{max} distributions.

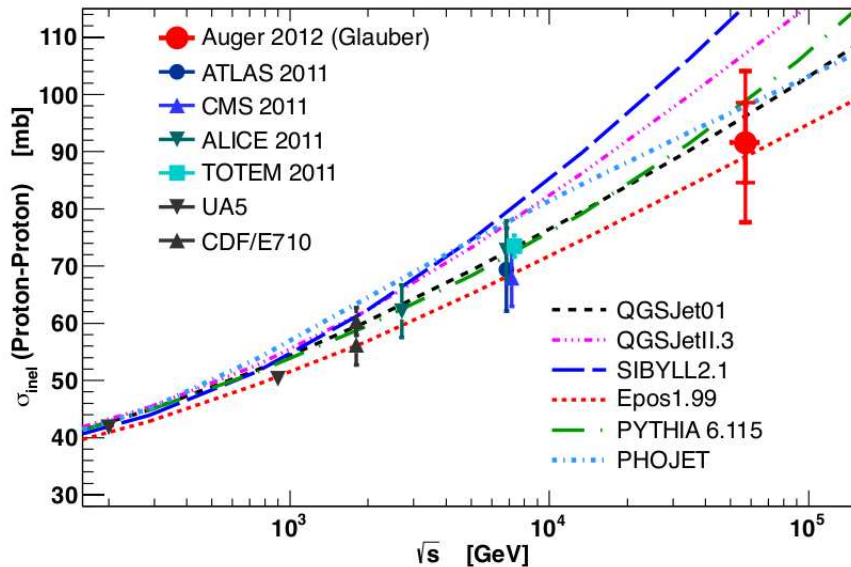


Fig. 2.20: Examples of measurements related to hadronic interactions. The Auger results are shown together with collider measurements and model extrapolations.

2.7 The upgrade of the Pierre Auger Observatory

The measurements of the Pierre Auger Observatory have led to a number of puzzling observations that indicate a complex astrophysical scenario, whose phenomenology is far from being understood. One striking result is the presence of a large fraction of protons in the energy range of the ankle. At the same time, according to the Auger data, the anisotropy of the arrival directions of these protons cannot be larger than a few percent. This is in contradiction to the expectations for light particles produced in Galactic sources, given the current knowledge of propagation in the Galactic magnetic field. The protons at energies as low as 10^{18} eV are most likely of extragalactic origin or one has to accept rather extreme assumptions on the Galactic magnetic field.

The Pierre Auger Observatory will operate until 2023, tripling the statistics of the current dataset. However, increasing the statistics of the measured showers will not be sufficient to answer the key questions that are still open. In this perspective an upgrade of the Pierre Auger Observatory was decided with the aim to improve the composition sensitivity and to extend it into the energy region of the flux suppression. The best way to obtain further

composition-sensitive information is the discrimination between the electromagnetic and muonic components of the shower with ground-array measurements.

The upgrade includes two components: an enhancement of the muon identification capabilities of the SD array and an upgrade of the SD station electronics to provide interfaces and data handling necessary for the muon enhancement. The electronics upgrade also includes improvements in sampling speed, dynamic range, triggering, and calibration to enhance the capabilities of the SD stations.

The current SD stations are already quite sensitive to the muonic component of the extensive air showers, a 4 m^2 plastic scintillator detector on the surface, more sensitive to the electromagnetic component of the EAS, could provide a complementary measurement. Infact the signal in the SD station is composed of roughly equal contributions from the electromagnetic and muon components, since a vertical muon deposits about 240 MeV as it traverses the detector while the hundredfold more abundant electrons and photons deposit a few MeV each. On the other hand the scintillator will not record large signals from the muons since muons and electrons will both produce minimum ionizing particle signals as they pass through the thin plastic scintillator, and then will count the numbers of electrons at ground level. This means that will be possible to estimate independently the energy of the shower with the scintillators, and the muon information obtained from the tanks could be applied toward composition studies.

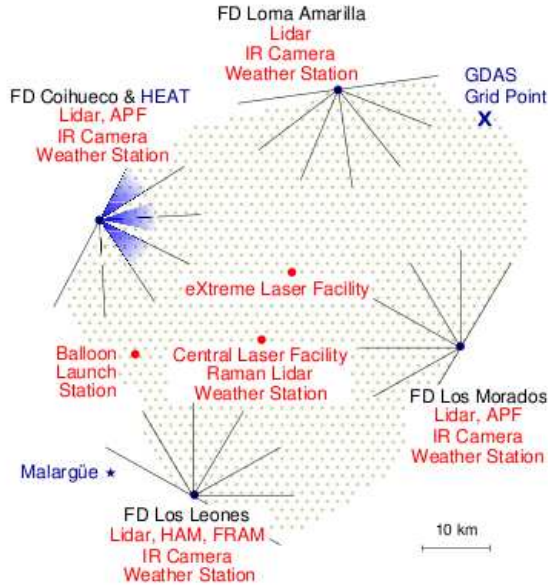


Fig. 2.21: Schematic overview of the atmospheric monitoring devices installed at the Pierre Auger Observatory.

2.8 Atmospheric Monitoring at the Pierre Auger Observatory

A detailed knowledge of the atmospheric conditions is a crucial point in experiments based on the detection of fluorescence light emitted by cosmic ray showers, since these experiments use the atmosphere as a huge calorimeter. The largest uncertainties that affect the fluorescence measurements comes from a correct estimation of atmospheric transmission, air Cherenkov subtraction and light multiple scattering. Between 10^{18} and 10^{20} eV, the systematic uncertainties due to all atmospheric effects increase from 3.4% to 6.2% in measurements of shower energy, and from $4 \text{ g} \cdot \text{cm}^{-2}$ to $8 \text{ g} \cdot \text{cm}^{-2}$ in measurements of the shower maximum [80, 51].

The Pierre Auger Observatory is complemented by an extensive atmospheric monitoring system to understand and remove the effect of atmospheric fluctuations on FD measurements. The altitude profile of the atmospheric depth, $X(h)$, typically varies by $\sim 5 \text{ g} \cdot \text{cm}^{-2}$ from one night to the next. In extreme cases, the depth can change by $20 \text{ g} \cdot \text{cm}^{-2}$ on successive nights, which is similar to the seasonal differences in depth. The largest variations are

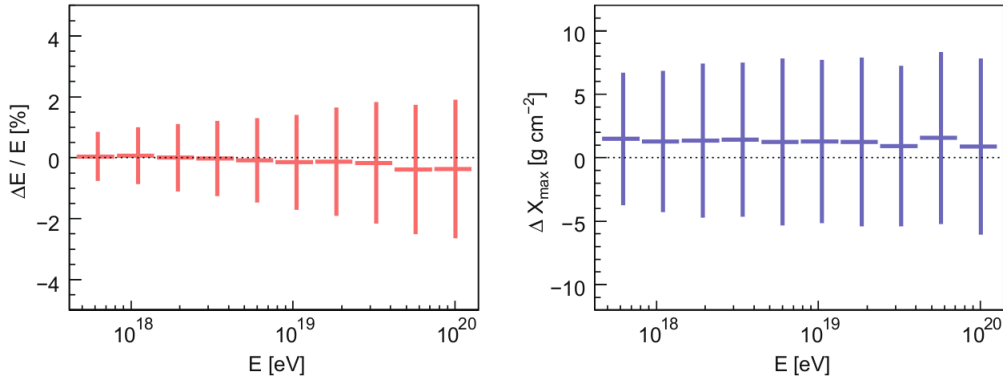


Fig. 2.22: Comparison of simulated events reconstructed with monthly average atmospheric profiles vs. profile measurements from 109 cloud-free balloon flights. The dotted lines indicate the reference for the 109 balloon flights; the uncertainties indicate the RMS spread [80].

comparable to the X_{max} resolution of the Auger FD, and could introduce significant biases into the determination of X_{max} if not properly measured. Atmosphere state variables are measured at ground level every five minutes by a network of weather stations placed at each FD site and in the center of the SD. In addition, their altitude profiles have been measured using regular meteorological radiosonde flights till 2010, and results were used to generate monthly models of atmospheric conditions.

These monthly models have been used to reconstruct simulated events that have been compared to events reconstructed with data from balloon measurements. The difference between results obtained with the two atmospheric data set is shown in Fig. 2.22. The use of the monthly models introduces small shifts into the reconstructed energy and X_{max} , the RMS of the measured energies shows an energy-dependent increase from 0.8% to 2.0% over the simulated energy range. The systematic shift in X_{max} is about $2 g \cdot cm^{-2}$ over the full energy range.

Another atmospheric property that affects air shower measurements is the variation of aerosol conditions: in hazy night the attenuation aerosol can reduce the light flux from distant showers by factors of 3 or more. Therefore, hourly measurements of the vertical aerosol optical depth, $\tau(h, \lambda)$ or $VAOD(h)$, are performed using the FD telescopes: they record vertical UV laser tracks produced by the two laser facilities of the observatory, the Central Laser Facility (CLF) and the eXtreme Laser Facility (XLF).

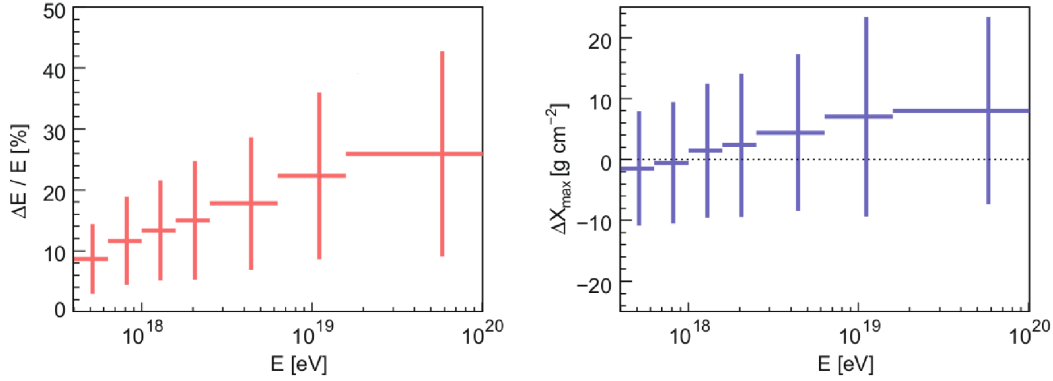


Fig. 2.23: Comparison of hybrid events reconstructed with hourly CLF aerosol optical depth measurements vs. events reconstructed with purely molecular transmission. Uncertainties indicate the RMS spread for each energy [80].

A comparison between energy and X_{max} of hybrid showers reconstructed using hourly aerosol optical depth measurements versus those reconstructed using a purely molecular atmosphere is shown in Fig. 2.23. Neglecting the aerosol contribution leads to an underestimation of the energy from 8 to 25% and a shift in the X_{max} that can reach $10 \text{ g} \cdot \text{cm}^{-2}$.

Scattering of light due to aerosol influence the correct determination of the longitudinal development of an air shower and leads to the introduction of correction of its energy that can range from a few percent to more than 40%, depending on the aerosol attenuation conditions, the distance of the shower, and the energy of the primary particle. In particular 20% of all the showers are corrected by more than 20%; 7% of showers need a energy correction greater than 30% and a small but significant fraction of the showers (3%) are corrected by more than 40%. The systematic shift in X_{max} ranges from $-1 \text{ g} \cdot \text{cm}^{-2}$ at low energies to almost $10 \text{ g} \cdot \text{cm}^{-2}$ at the highest energies, with an RMS of $10 - 15 \text{ g} \cdot \text{cm}^{-2}$.

The rapid changing in aerosols conditions makes the use of average aerosol models in showers reconstruction not reliable. The differences in the reconstruction between this average model and the hourly data are shown in Fig. 2.24: the RMS of $\Delta E/E$ is about 8%, with events with correction greater than 40%. Uncertainties in aerosol attenuation measurements cause over- or under-corrections of recorded shower light profiles, particularly for the showers far from the FD stations. On average, underestimation of the aerosol optical depth decrease the shower energy estimate and push the reconstructed X_{max} higher into the atmosphere.

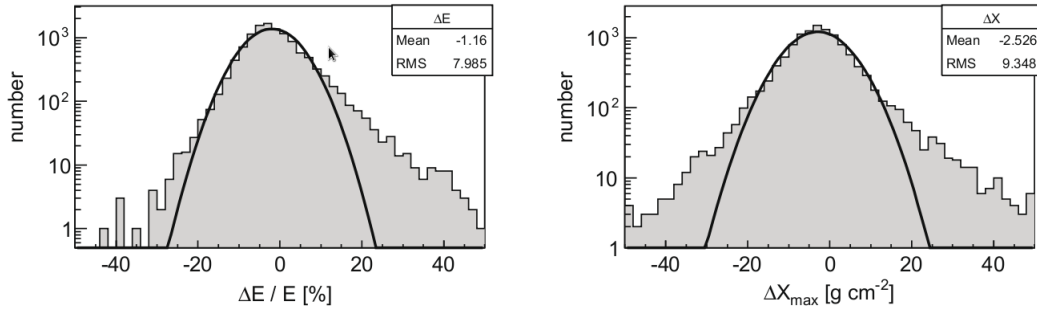


Fig. 2.24: Distributions of the differences in energy and X_{max} , shown with Gaussian fits, between hybrid event reconstructed using average aerosol conditions rather than hourly measurements.

The aerosol monitoring system of the Observatory is completed by a Raman lidar and an elastic lidar recently installed at the CLF site, two Aerosol Phase Function Monitors (APFs) that measure aerosol scattering properties, two optical telescopes — the Horizontal Attenuation Monitor (HAM) and the (F/ph)otometric Robotic Telescope for Atmospheric Monitoring (FRAM) — record data used to determine the wavelength dependence of the aerosol attenuation.

The atmospheric monitoring network is completed by four lidar stations that are used to measure the cloud height, and infrared cameras placed on the roof of each FD building are used to record the cloud coverage in the FD field of view. The features of each device will be described in the next paragraph.

Data from atmospheric measurements are stored in MySQL databases and indexed by observation time, so that the atmospheric conditions can be used to reconstruct hybrid events.

2.8.1 Atmospheric Monitoring Devices

Air Density Profile: balloon launches, weather stations and GDAS

Altitude profiles of air density and molecular optical depth are needed for a proper reconstruction of the fluorescence telescope signals. These quantities are calculated from measurements of atmospheric state variables, temperature, pressure, and humidity up to about $20 \div 25$ km a.s.l..

Atmospheric ground informations are registered by several weather stations

that are installed in the observatory. Some of these stations are also used for operational control of the nearby installations (e.g. FD, lidars).

The measurement of air density profiles with altitude results from several campaigns of launches of meteorological radiosondes that started in August 2002 and were terminated in December 2010. Based on the locally measured atmospheric profiles, monthly models of atmospheric conditions at the Pampa Amarilla were derived in December 2008 [81]. These measurements have been used to validate the precision of data from the Global Data Assimilation System (GDAS) for the purpose of air shower reconstruction at the Pierre Auger Observatory [82]. GDAS data relies on established meteorological models and have an excellent time resolution of 3 h. Since the GDAS data significantly reduce the systematic errors and overall uncertainties in air shower reconstructions, the standard air shower analyses of the Pierre Auger Observatory are now applying atmospheric data from GDAS.

Horizontal Attenuation Monitor (HAM)

The Horizontal Attenuation Monitor (HAM) of the Pierre Auger Observatory has been used to measure the wavelength dependence of the aerosol extinction coefficient. This dependence is typically parameterized by a power law whose exponential factor is the Ångström coefficient γ (see formula 1.18). Larger value of γ correspond to smaller particle size: the clear air limit of γ is about 4. The HAM consists of a high intensity discharge lamp installed close to the FD building Coihueco. Light from this lamp is measured by a filtered CCD camera at the FD Los Leones building, about 45 km away. Total horizontal atmospheric attenuation was measured over this path at five wavelengths between 350 and 550 nm. The data indicates that the atmosphere of the Auger Observatory is quite desert-like with weak wavelength dependence. An average value of γ of about 0.7 with an RMS of 0.5 is used as a parameter in the air shower reconstruction.

Photometric Robotic Atmospheric Monitor (FRAM)

The ph(F)otometric Robotic Atmospheric Monitor (FRAM) is an optical telescope (0.3 m diameter mirror) equipped with CCD camera and photometer [83]. It measures the integral atmospheric extinction using stellar photometry, by comparing light flux of selected standard stars to values from catalogues. It also determines the wavelength dependence of Rayleigh and Mie scattering, by measuring the Ångström coefficient: the FRAM measured a mean value of $\gamma = -0.1 \pm 0.9$, in good agreement with theoretical expectations for atmosphere in desert-like environment.

Aerosol Phase Function (APF)

The scattering of the fluorescence light from EAS with the atmosphere varies with scattering angle. The knowledge of the scattering angular distribution, the phase function, is necessary to implement a suitable parametrization of the scattering behaviour into the air shower reconstruction process. The atmospheric molecular phase function can be estimated analytically but the aerosol one depends on the size and shape of the aerosols and must be measured. The *Aerosol Phase Function monitors* fire a collimated light of a Xenon flash lamp, at wavelength between 350 and 390 nm, horizontally across the FD field of view at Coihueco and Los Morados, and the FD measures the light as a function of scattering angle (30° to 150°).

Results from data analysis reveals that the aerosol scattering at the site of the Auger Observatory is well described by the Henyey-Greenstein function (see eq. 1.19). An average value of the phase function asymmetry parameter $g = 0.56 \pm 0.10$ is used in the Auger air shower analysis for nights with aerosol. For clear or almost clear nights, g is set to zero with an estimated uncertainty of 0.2.

Cloud Cameras

The Pierre Auger Observatory utilizes four infra-red cameras, located on the roof of each FD building, to measure the fraction of the sky covered by cloud [87]. The cloud cameras used are Gobi384 uncooled radiometric microbolometer array infra-red cameras. These cameras operate in the 8 – 14 μm wavelength band with a field of view of $50^\circ \times 37.5^\circ$ and produce images consisting of 384×288 pixels. Directions of the cloud camera pixels can be associated to FD pixel directions so it is possible to flag that detected showers that may be affected by cloud. An hourly cloud coverage below 20% is required for the use of hybrid events in the analysis of the mass composition and energy spectrum of the cosmic rays.

Laser Facilities : CLF, XLF

Two laser facilities (Central Laser Facility, CLF [84] and eXtreme Laser Facility, XLF [85]) are located in the middle of the Pierre Auger Observatory SD array, at distances that range from 25 to 40 km from the FD buildings. The light emitted by a pulsed frequency Nd:YAG UV lasers (355 nm) into the sky is recorded by the 4 FD sites. The linearly polarized beam emitted by the laser pass through a depolarizer that randomizes the polarization, in this way the light of the vertical beam is scattered with the same probability in the direction of each FD telescope.

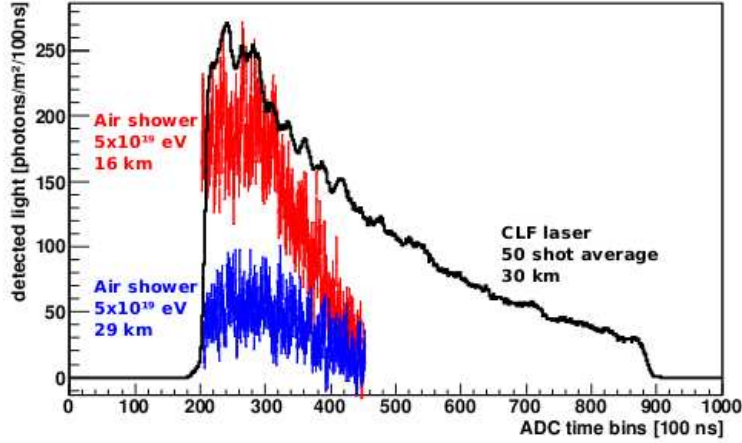


Fig. 2.25: Comparison between a 50 shot average of vertical 6.5 mJ UV laser shot from the CLF and near-vertical cosmic ray showers measured with the FD. The cosmic ray profile has been flipped in time so that in both cases the left edge of the profile corresponds to the bottom of the FD field of view.

The nominal energy of the laser is 6.5 mJ, and relative energy of each pulse is monitored by a photo-diode detector. The amount of light of a laser beam of this energy that is scattered out by the atmosphere is roughly equivalent to the amount of UV fluorescence light produced by an EAS of $5 \cdot 10^{19} eV$ at a distance to the telescope of about 16 km, as shown in Fig. 2.25. Laser light is attenuated exactly as the fluorescence light emitted by a shower; therefore, the analysis of the amount of laser light that reaches the detector can be used to infer the attenuation due to aerosols. The CLF and the XLF are then used to obtain hourly measurements of the aerosol optical depth profiles [86] that are used in the reconstruction of each FD air shower event. The Vertical Aerosol Optical Depth (VAOD, or $\tau_{aer}(h)$) is defined as the integral of the aerosol extinction from the ground to a point at a given altitude observed at a given elevation angle ϕ :

$$VAOD(h) = \int_0^h \alpha(z) dz / \sin(\phi) \quad (2.9)$$

The CLF has been in operation since 2003. The XLF was installed in 2008 and includes an automated calibration system that measures the beam energy and polarization. A major upgrade to the CLF in 2013 added a beam calibration system and a backscatter Raman lidar receiver.

Lidars

The Pierre Auger Observatory is equipped with a network of lidars. A lidar is a laser-based system that emits a light pulse into the atmosphere: the light is scattered in all directions by molecules and particulates of the atmosphere, and the portion that is scattered in the backward direction is collected by a telescope and focused on a photodetector. In the Observatory four steerable lidars are installed close to each FD: these lidars use a Nd:YLF laser that produces 0.1 mJ pulses at a wavelength of 351 nm and repetition rate of 333 Hz. The light receiver is composed by three 80 cm mirrors and a 20 cm mirror and the backscattered light is measured with Hamamatsu R7400U photomultipliers. Each lidar measures the cloud cover and cloud height. [88, 89]. Lidars can provide profiles of the volume backscatter coefficient, of the volume extinction coefficient, and then of the aerosol optical depth but these measurements are not performed in the field of view of the FD due to the high interference with data acquisition.

A Raman lidar has been recently installed at the Central Laser Facility site. It measures the elastic backscattered light and the Raman-shifted light scattered by N_2 molecules, at about 375 nm, and by water vapour at about 387 nm. The value of the cross sections for the Raman scattering is about three order of magnitude smaller than corresponding Rayleigh cross-section, accordingly, the number of photons returning to the lidar is small: for this reason the Raman technique needs longer data taking time (at least 20 minutes) and cannot be used during shower acquisition due to interference.

2.8.2 Measurements of the VAOD profiles using CLF and XLF

The aerosol attenuation profiles needed for showers analysis are stored in a hourly database produced analyzing CLF and XLF data. CLF and XLF fire 50 vertical shots every 15 minutes during FD data taking. The scattering angles of light from the beam observed by the FD are in the range of 90° to 120° : the aerosol database is filled in steps of 200 m starting from the ground up to the maximum height analyzable. Data refers to four regions of the observatory centered in each FD station as shown in Fig. 2.27: in each region horizontal uniformity of the aerosol concentration in a vertical slice is assumed.

To measure the aerosol attenuation, laser light profiles are normalized to the expected profile for an aerosol-free night.

Two independent analyses have been developed to provide hourly aerosol optical depth profiles using CLF and XLF laser shots [86] and fill the aerosol

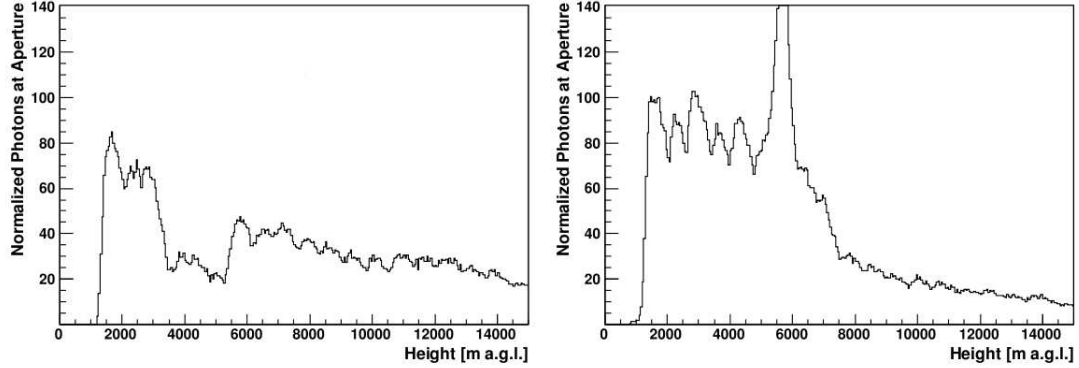


Fig. 2.28: Examples of clouds identification from the measure of laser light profiles with the FD: on the left a cloud is present between FD and laser, on the right a cloud is above the laser beam.

database:

- The *Data Normalized Analysis* is based on the comparison of measured profiles with a reference clear night profile in which the light attenuation is dominated by molecular scattering.
- The *Laser Simulation Analysis* is based on the comparison of measured light flux profiles to simulations generated in various atmospheres in which the aerosol attenuation is described by a parametric model. This method will be described in detail in the next chapter.

In both techniques measured profiles are normalized to a reference aerosol-free profile. This normalization allows to remove the systematic uncertainties related to the FD and laser calibrations and to the simulation process.

Analysis of longitudinal profiles of lasers are also useful to identify clouds above the observatory. Clouds appear in laser light profiles as peaks or holes depending on their position. A cloud placed directly above the CLF appears as a peak in the profile, since multiple scattering in the illuminated cloud enhances the amount of light scattered towards the FD. A cloud between the CLF and the FD appears as a hole in the profile because blocks the transmission of light in its travel from the emission point towards the fluorescence telescopes.

2.9 A comparison of techniques: the ARCADE project

Instruments usually dedicated to the measure of aerosol attenuation in atmospheric physics community are the lidars. In the previous paragraphs it was discussed that in a cosmic rays experiment lidar measurements interfere with usual shower acquisition, and since they need long acquisition time, these instruments can't be used during EAS data taking. For this reason other techniques, less accurate but also less invasive than lidar have been developed to measure the aerosol optical depth. These methods, based on use of the same telescopes of the observatory, introduce some assumption on the features of the atmosphere and need to be checked.

In chapter 4 I will introduce the ARCADE project - Atmospheric Research for Climate and Astroparticle DEtectors: one of the aims of the project is to provide simultaneous observations of the same air mass with different instruments (a Raman lidar, a steerable elastic lidar and a UV telescope for side scattering measurement) to allow a direct comparison of the techniques. From a better knowledge of the methods it will be possible to estimate the systematic uncertainties related to each one and to determine their limit of applicability.

Chapter 3

Aerosol attenuation measurements in the Auger experiment

3.1 Introduction

Two different analysis methods for the measurement of aerosol attenuation altitude profiles using vertical laser tracks have been developed within the Pierre Auger Collaboration: the *Data Normalized Analysis* (DN) and the *Laser Simulation Analysis* (LS). Both techniques evaluate the aerosol attenuation from the measuring with the FD the light that is emitted by the laser facilities of the observatory and that is scattered toward the FD by the atmosphere. Two different aerosol databases are generated using results of the two analyses. The consistence of the two databases is evaluated mainly by the comparison the aerosol optical depth measured at 3 km a. g. l. with the two techniques: if a good correlation between the two data sets is found results are merged to fill the official aerosol database. The value of the Vertical Aerosol Optical Depth (VAOD) at 3 km a.g.l. is also used as discriminating parameter to decide which data can be used for the shower analysis: only hours of the night when the value of the VAOD at 3 km is lower than 0.1 are used to fill the aerosol database, and so only air shower data acquired during those hours can be properly analyzed. In this chapter I will describe in detail the technique I used for the measurements of aerosol attenuation, the Laser Simulation Analysis, and I will present the results of the data analysis I have carried out.

Data Normalized Analysis

The method depends on the assumption that it is possible to find a night in which the atmosphere can be considered free of aerosols and determines the VAOD of a certain hour from the ratio between the associated hour light profile with the profile measured in the clear night [90]:

$$VAOD(h) = -\frac{\sin(\pi - \theta)}{1 + \sin(\pi - \theta)} \left(\ln \left(\frac{N(h)}{N_{mol}(h)} \right) - \ln \left(1 + \frac{S_{aer}(\theta, h)}{S_{mol(h)}(\theta, h)} \right) \right) \quad (3.1)$$

where $N(h)$ is the number of photons of the observed hourly profile as a function of height and scattering angle θ , and $N_{mol}(h)$ is the number of photons from the reference clear profile as a function of height. $S_{mol}(\theta, h)$ and $S_{aer}(\theta, h)$ are the fraction of photons scattered out of the laser beam per unit height by air molecules, and aerosols respectively and are defined as the product of the differential cross section for scattering towards the FD multiplied by the number density of scattering centers.

Since aerosol scatter predominately in the forward direction $S_{aer}(\theta, h)$ is small compared to $S_{mol(h)}(\theta, h)$ thus the second term in equation 3.1 can be neglected and it becomes:

$$VAOD(h) = \frac{1}{1 + \operatorname{cosec}(\pi - \theta)} \cdot \ln \left(\frac{N(h)}{N_{mol}(h)} \right) \quad (3.2)$$

With these simplifications, the CLF optical depth measurements depend only on the elevation angle of each laser track segment and on the number of photons of the observed laser event and the reference clear profile.

3.2 Laser Simulation technique

The Laser Simulation method is a procedure developed in the past years within the Auger group of Naples to estimate the atmospheric VAOD using the Fluorescence Detector and the Central Laser Facility (CLF) of the Pierre Auger Observatory.

The light emitted by the CLF, randomly polarized and hence isotropically diffused towards each FD building, is scattered and attenuated by the molecular and aerosol components of the atmosphere along the path towards the FD buildings exactly as the fluorescence light emitted by a shower.

The measurement of the aerosol attenuation comes from the comparison of a quarter-hour average laser light profile (photons collected at the aperture of the FD building as a function of ADC time bins) with a grid of simulated profiles.

Each simulation is generated using a different profile of the aerosol extinction coefficient $\alpha_{aer}(h)$ that is evaluated following the parametric formula:

$$\alpha_{aer}(h) = \frac{1}{L_{aer}} \left[\exp\left(-\frac{h}{H_{aer}}\right) \right] \quad (3.3)$$

where the parameter L_{aer} is the *aerosol horizontal attenuation length* that describes the attenuation of light due to aerosols at ground level and H_{aer} is the *aerosol scale height*, that accounts for the dependence of the aerosol attenuation on height. As a result the aerosol optical depth from the ground level h_0 to a certain altitude h_1 is:

$$\tau_{aer}(h_1 - h_0) = \int_{h_0}^{h_1} \alpha_{aer}(h) dh = -\frac{H_{aer}}{L_{aer}} \left[\exp\left(-\frac{h_1}{H_{aer}}\right) - \exp\left(-\frac{h_0}{H_{aer}}\right) \right] \quad (3.4)$$

The Laser Simulation Analysis can be divided in three main phases:

- production of a grid of simulated laser events;
- reconstruction of measured laser events;
- research of the simulation that best fit the measured event in analysis to evaluate the aerosol optical depth profile.

3.2.1 Simulation of a laser event

The software for the simulation and reconstruction of a laser profile are implemented in the official framework of the Auger Collaboration, the Offline. The simulation of a laser event is performed in different steps developed in dedicated modules:

- *LaserGeneratorNA* sets energy, wavelength and direction of the laser beam;
- *EventGeneratorOG* sets position (in UTM coordinates) and time of the event;
- *FdSimEventCheckerOG* sets the status of the detector components that are existing at the time of the simulation;
- *LaserLightSimulatorNA* calculates the starting number of photons in the laser beam $N_0 = \frac{Energy}{hc/\lambda}$, where h is the Planck's constant, c is the speed of light, and λ the wavelength of the laser.

- *LightAtDiaphragmSimulatorKG* propagates the laser light along the axis of the beam, calculates the amount of light scattered toward each FD site, and propagates it through the atmosphere taking into account the Rayleigh and Mie scattering phase functions and attenuation. Multiple scattering is not yet implemented in the code;
- *ShowerPhotonGeneratorOG* calculates the number of photons reaching the FD diaphragm for each time interval;
- *TelescopeSimulatorKG* handles the ray-tracing of the photons on the diaphragm through the geometry of the telescope. Ray-tracing of photons in the telescope optics takes care of reflection and refraction at the corrector lens, mirror, light collectors and PMT window. Transmission and reflectivity of all materials is properly considered. Photons reaching the photocathode of a PMT are added to the corresponding photon signal.
- *FdBackgroundSimulatorOG* simulates the background photons flux from bright stars, the Milky Way, the moon, the atmosphere and other sources that are recorded by the telescopes.
- *FdElectronicsSimulatorOG* converts the number of generated photoelectrons at the photocathode of each PMT in an ADC signal;
- *FdTriggerSimulatorOG* simulates the three trigger levels of the telescopes;
- *EventBuilderOG* combines all FD and SD data to build a valid data object;
- *EventFileExporterOG* writes the resulting event on disk at the end of the module chain.

The simulation chain produces an output ROOT file that contains, among other informations, the number of counts recorded by the ADC as a function of the time as shown in Fig.3.1.

To summarize, the simulation of a laser event within the Offline includes the generation of a laser beam, scattering and attenuation of the laser light toward the FD, and the generation of the signals produced by the PMTs of the FD.

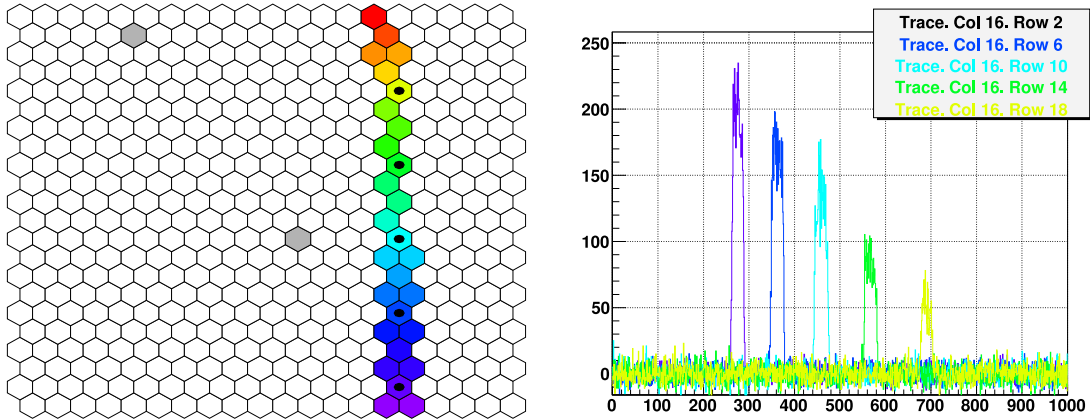


Fig. 3.1: A simulated CLF event as seen by the FD. On the left, a vertical trace as seen by Los Leones FD site; on the right, the ADC signal corresponding to the selected pixels. On the y-axis there is the number of ADC counts, on the x-axis the ADC time bins, where each bin is 100 ns.

3.2.2 Reconstruction of a laser event

The reconstruction process consists in the conversion of the ADC counts recorded by the acquisition in number of photons at the aperture of the telescope. The procedure for the reconstruction of simulated and measured laser profile is the same. The reconstruction of a laser event is performed in different steps developed in dedicated modules:

- *EventFileReaderOG*: reads the measured/simulated input file containing the laser events;
- *FdLaserSelectEvents*: distinguishes if the data is a measured or simulated event and the laser (CLF or XLF) used to generate it, and read the file containing the measured energy of each laser shot that will be used to normalize each event to the energy of the laser set in the simulation;;
- *FdCalibratorOG*: discriminates the triggered pixels and evaluate the calibration factor for each one;
- *FdPulseFinderOG*: finds the pulse generated by the laser light in each pixel signal;
- *FdAxisFinder_FixGeom* sets the geometry of the event;

- *FdApertureLightFinderCoord* finds the optimal light collection angle of image of the laser on the camera;
- *FdMeanProfile* generates an average light profile using group of 50 laser events, and normalizes it to the energy of the laser set in the simulation;

The number of photons at diaphragm calculated takes into account the absolute and relative calibrations of photomultipliers.

Each light profile is normalized to 6.5 mJ, the energy of the laser set in the simulation, reading a text file generated during laser firing that contains informations about the time of each shot and its energy.

Since single event profiles are characterized by large fluctuations, the laser facilities fire groups of 50 vertical shots every 15 minutes and so average profiles of 50 events are produced for this analysis. The average profiles reveal very clearly the details of the shape and the structures due to the detector (see Fig. 3.2). As for measured events, also simulations are generated in groups of 50 to build average profiles of light at the aperture for the comparison procedure.

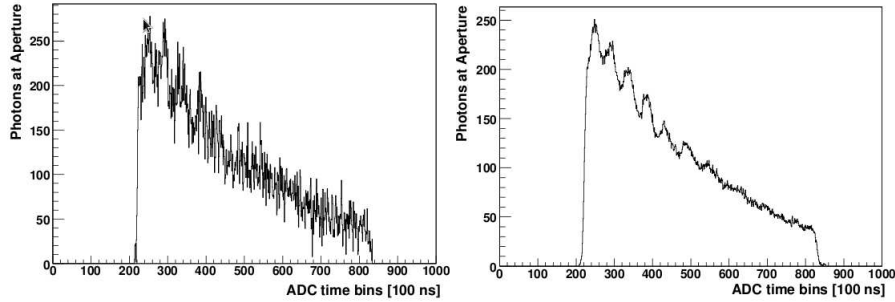


Fig. 3.2: On the left a reconstructed light profile of a single CLF vertical shot seen from the Los Leones FD site; on the right a 50 shots average profile.

3.2.3 VAOD measurements

The laser facilities of the Pierre Auger Observatory fire 50 shots at 4 Hz every 15 minutes during the normal EAS data taking. The goal of the data analysis is to measure an altitude profile of the VAOD for all the available laser data, in order to produce hourly corrections for the shower data.

Since the Laser Simulation Analysis is based on the search for the simulated light profile that best reproduces the aerosol conditions of a measured one, a grid of different simulations is produced. The simulations are generated at 6.5 mJ, which is the average laser energy, the air density profiles are provided by the Malargüe Monthly Models, as discussed in 2.8.1, and the aerosol conditions are varied according to the parametric model described by the formula 3.4. The grid is generated by varying L_{aer} from 5 to 150 km in steps of 2.5 km and H_{aer} from 0.5 km to 5 km in steps of 0.25 km, corresponding to 1121 profiles per month and to a total of 13452 simulated profiles for each FD site. In the left panel of Fig. 3.3, a measured CLF profile (in blue) is shown together with four out of the 1121 monthly CLF simulated profiles (in red) used for the comparison procedure. In the right panel, the four aerosol profiles corresponding to the simulated CLF profiles are shown.

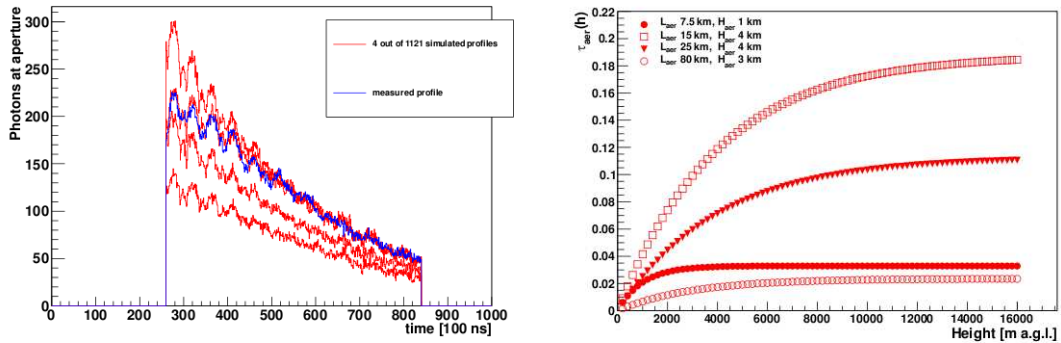


Fig. 3.3: Left: a reconstructed laser profile (in blue) with four simulated profiles (in red) used for the comparison procedure. Right: the four aerosol profiles $\tau_{aer}(h)$ corresponding to the simulated profiles are shown.

Since the absolute FD and laser calibrations are known within an uncertainty of 10% and 7%, respectively, the relative energy scale between measured and simulated laser profiles has to be fixed. To scale simulations to data we use a reference night, the so-called “Rayleigh night”, where the aerosol attenuation of light can be neglected and the scattering is dominated by the molecular part of the atmosphere. In this night, the measured light profiles are larger than profiles affected by aerosol attenuation and have shapes

that are compatible with a profile simulated under atmospheric conditions in which only molecular scattering of the light is used. The Rayleigh night profile is chosen among measured profiles by the comparison with an aerosol free simulated profile: the *Kolmogorov test* implemented in the ROOT package is used to define a sub-set of profiles that have a shape compatible with the simulation, and the one that has the highest number of photons is identified as the Rayleigh night profile [86]. The ratio between the number of photons of this profile and the simulated one provides the normalization constant that fixes the relative energy scale between measured and simulated laser profiles. In this way the dependence on FD and CLF absolute calibrations is avoided and only the relative uncertainty (daily fluctuations) of the laser probes (3%) and FD calibration constants (3%) must be taken into account.

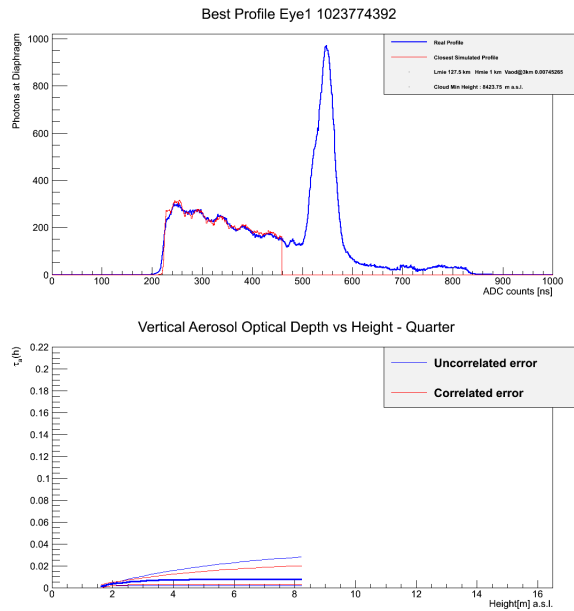


Fig. 3.4: Top panel: a measured light profile (blue) showing a cloud in the field of view of the FD and the simulated profile (red) that best fit it after the cloud identification. Bottom panel: the VAOD(h) profile associated to the measured event; VAOD(h) value are calculated up to the cloud base altitude.

The code developed for the determination of the aerosol attenuation corresponding to each quarter hour average measured profile identifies the L_{aer} and H_{aer} pair corresponding to the simulated profile closest to the analyzed event. The parameters chosen are those the one that minimizes the square difference between measured and simulated profiles computed for each time bin. Before the determination of the VAOD, each quarter hour average pro-

file is checked for the presence of clouds in the FD field of view in order to establish the maximum altitude of the corresponding aerosol profile. To identify a cloud the code produces the light profile of the difference in photons for each bin between the measured profile under study and the most compatible simulated one, in this way the signal is flat and peaks or holes are clearly visible.

A peak indicates presence of a cloud directly above the CLF, a hole is due to a cloud placed in the path between the CLF and the FD. The quarter-hour is rejected if a cloud is detected between the laser track and the FD; on the other hand, if a cloud is detected above the laser track, the profile is truncated at the cloud base height and the lowest part of the profile is reanalyzed, since the first search for clouds only identifies the optically thicker cloud layer (see Fig. 3.4). If the truncated profile shows another cloud, or if the height of the first cloud is lower than 5500 m above sea level, the profile is rejected. If no clouds are detected, the pair of parameters together with the maximum height of the profile are stored, the procedure is completed and the quarter hour VAOD profile ($VAOD_{BEST}$) is calculated according to equation 3.4.

The four quarter hour VAOD profiles are averaged to obtain the hourly VAOD profile and the aerosol extinction profile $\alpha_{aer}(h)$ with the associated uncertainties obtained propagating the errors due to laser energy monitoring, to the FD calibration, to the choice of the reference night and to the use of a parametric model to approximate (the way to propagate the uncertainties is described in sec. 3.3.2). In average the relative uncertainty associated to the VAOD altitude profile, $\Delta VAOD(h)/VAOD(h)$ is about 30%.

3.3 My contributions in the data analysis

As a member of the atmospheric monitoring group of the Pierre Auger Collaboration, I worked on the data analysis of vertical laser tracks for the writing of the aerosol database.

In particular I performed for the first time the analysis of XLF data adopting the Laser Simulation Analysis, producing results that, after an accurated validation, were used to fill a new version of the aerosol database released in 2013 (sec. 3.3.1); I have also taken part to the release of the new aerosol database in 2013 characterized by a different estimation of uncertainties, addition of more data and new laser calibration evaluation (sec. 3.3.2); finally I was asked by the collaboration to work on an upgrade of the Laser Simulation Analysis that includes a third parameter in the description of the aerosol attenuation to reproduce more realistic VAOD altitude profiles (sec. 3.3.3).

3.3.1 XLF data analysis

In 2010 a new laser facility was installed at the Pierre Auger Observatory, the XLF with the purpose of having two laser facilities each equidistant from three of the four FD buildings: infact since CLF is far from Loma Amarilla FD site (~ 40 km) before the use of XLF the VAOD analysis using that FD eye was achievable only in night with low values of aerosol attenuation. The XLF is placed ~ 30 km far from Loma Amarilla, Los Morados and Coihueco FD sites, as shown in Fig 3.5, and about 40 km far from Los Leones (LL): so XLF can be used to perform the VAOD analysis for the three nearest sites. The XLF is also equipped with an automated robotic beam calibration system that provides daily absolute calibration of the laser beam.

I performed the analysis of the XLF data for the first time, applying the Laser Simulation Analysis to the FD data of the new laser facility. First of all to adopt the analysis I had to generate a new grid of simulated XLF profiles varying aerosol conditions as for the CLF analysis. A comparison of a simulated light profile with a measured one is shown in Fig. 3.6: also XLF simulated events perfectly reproduce measured data.

The algorithm used to identify the reference night and the simulation that best reproduces the event in analysis is the same as for the CLF, with some minor modifications. VAOD profiles have been produced from all FD buildings for the years 2010 - 2013.

To check the reliability of XLF results I compared hourly aerosol optical depth profiles obtained with XLF analysis to those obtained using CLF analysis in the same hours and from the same FD site.

First I compared the value of VAOD at 3 km a.g.l for the FD sites that are

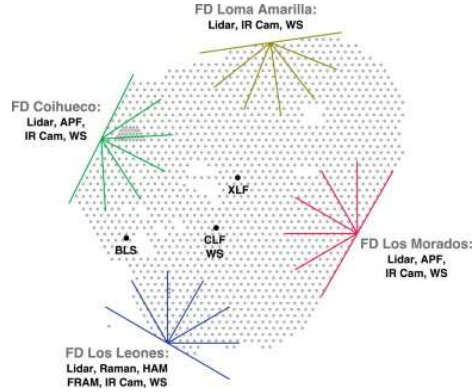


Fig. 3.5: Map of the Pierre Auger Observatory: both laser facilities are equidistant from three of the four FD sites. The CLF is placed ~ 30 km far from LL, LM and CO FD sites, and is far ~ 40 km from LA FD site; the XLF is placed ~ 30 km far from LM, LA and CO FD sites, and is ~ 40 km from LL FD site

almost equidistant from the two laser facilities, looking at the same portion of atmosphere (Fig. 3.7): the good correlation among the two measurements, within the error budget, confirms the goodness of results obtained with the new laser analysis. In average the differences in the values of the VAOD at 3 km a.g.l. obtained with the two laser facilities is less than 0.01 (Fig. 3.8), a value comparable with the average uncertainty associated to the VAOD at this altitude.

A step forward was a check of the compatibility of the VAOD resulting from the analysis of the two lasers for those FD sites, Los Leones and Loma Amarilla, which are near (~ 30 km) to one laser facility and far (~ 40 km) from the other. The value of the VAOD at 3 km obtained using XLF is still correlated, within the error, to that obtained using CLF, but in this case the far laser facility can't provide results in hazy atmospheric conditions and so comparison is limited to value of VAOD at 3 km lower than ~ 0.1 (Fig.3.9). As a conclusion, the Laser Simulation Analysis applied to XLF data produces aerosol profiles compatible to those obtained with CLF, even in case of a very distant laser facility.

Within the Auger Collaboration it has been first decided to use XLF data only to fill the aerosol database for the Loma Amarilla FD site, starting from 2010. During 2014 since the CLF was off for an upgrade from March to June 2013, it has been decided to use XLF data to fill the aerosol database when CLF is not available.

Finally in Fig. 3.10 results of the VAOD at 3 km a.g.l from the Laser Simulation Analysis are compared with results of the Data Normalized Analysis

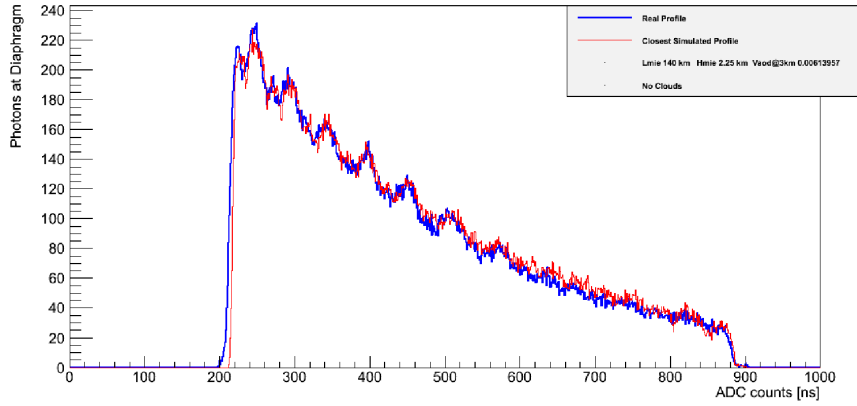


Fig. 3.6: XLF simulated profile (red) superimposed to measured (blue) profile.

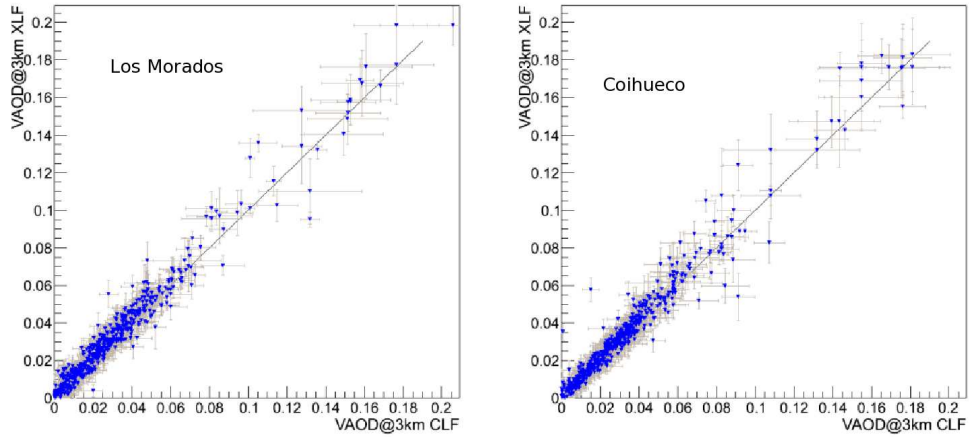


Fig. 3.7: Comparison of the values of the VAOD at 3 km obtained using the XLF and CLF data analysis for FD sites which are equidistant from the two lasers.

for the equidistant FD sites: the values compare well, although there seems to be a small systematic shift towards higher VAOD for the Laser Simulation method. Anyway this shift is within the error budget.

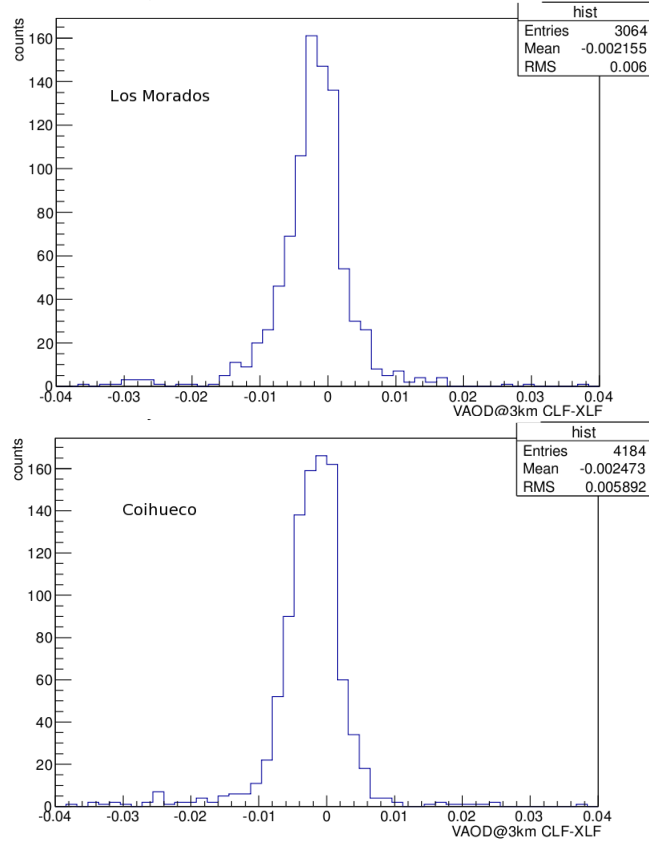


Fig. 3.8: Differences between the value of the VAOD at 3 km obtained using CLF and that obtained using XLF for equidistant FD sites.

3.3.2 New Auger aerosol database

During the last years (2012-2013) the Auger collaboration has made a big effort to update the energy scale of the Surface Detector obtained using hybrid events [51]. The update took benefits of more precise measurements of the fluorescence yield, of a deeper understanding of the detector and of a better estimate of the invisible energy, that component of the shower (such as neutrinos and high energy muons) that cannot be measured by the detector. The detailed study of the detector led to a re-estimate of the past FD absolute and relative calibrations and CLF energy calibration. Concerning the CLF energy calibration, all the past calibration factor were re-calculated using a function describing the time drift in the calibration factor (see Fig. 3.11) due to accumulation of dust on one the mirror of the laser bench. Infact the calibration factor was changing every time the mirror was cleaned. For all these reasons it was decided to work on a complete revision of the aerosol

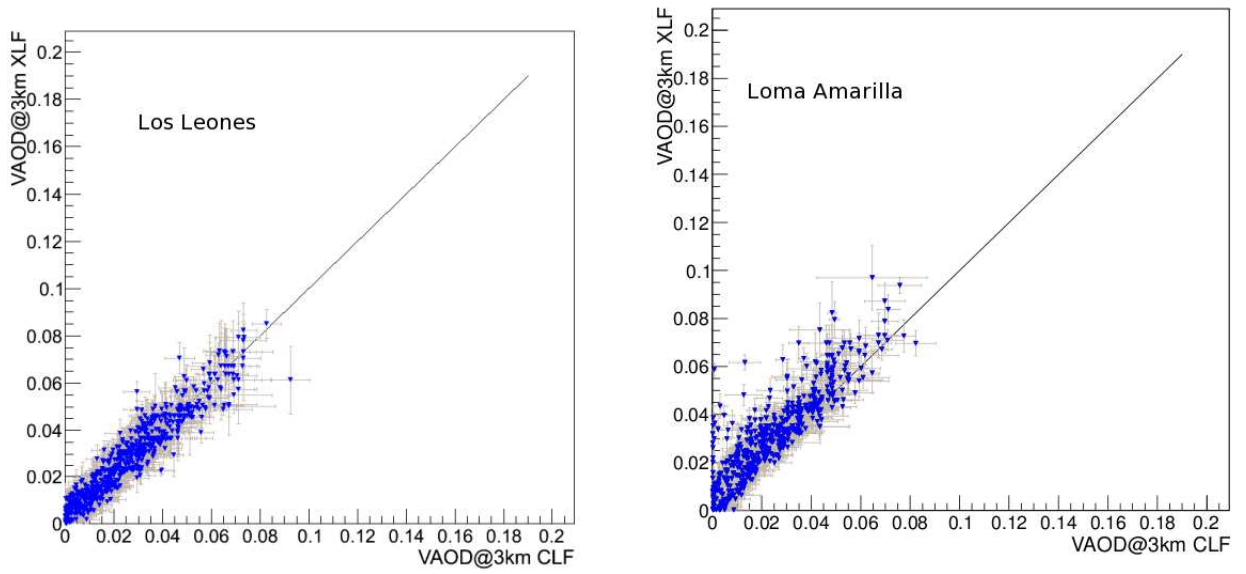


Fig. 3.9: Comparison of the values of the VAOD at 3 km obtained using the XLF and CLF data analysis for FD sites which are near to one laser and far from the other one.

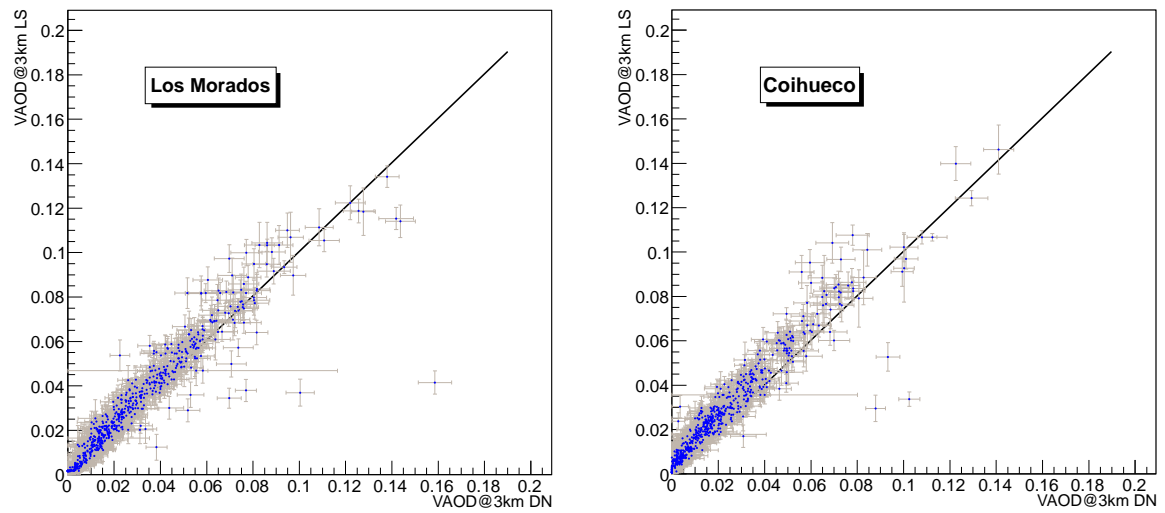


Fig. 3.10: Comparison of the values of the VAOD at 3 km using XLF data from the Laser Simulation Analysis and the Data Normalized Analysis.

Epoch	Los Leones	Los Morados	Loma Amarilla	Coihueco
1	Apr. 21, 2004, 5–7			Jun. 12, 2004, 5–7
2	Dec. 12, 2004, 2–3			Dec. 12, 2004, 2–3
3	Jun. 5, 2005, 3–5			Jun. 4, 2005, 3–5
4		May 17, 2005, 2,5,7		
5		Jun. 11, 2005, 1–3		
6	Jun. 30, 2006, 6–8	Jun. 25, 2006, 3–5		Jun. 25, 2006, 2–4
7	Jul. 17, 2007, 7–9	Jul. 20, 2007, 3,4,6		Aug. 22, 2006, 1–3
8	Aug. 30, 2008, 2–4	Aug. 30, 2008, 3–5		Aug. 30, 2008, 5–7
9	Jun. 24, 2009, 7–9	Jun. 23, 2009, 0–2		Oct. 19, 2009, 4–6
10	Aug. 18, 2010, 7–9	Jul. 8, 2010, 6–8	Jun. 6, 2010, 4–6	Jun. 20, 2010, 5–7
11	Jun. 8, 2011, 3–5	Jun. 24, 2011, 4–6	Jul. 9, 2011, 6–7	Jul. 23, 2011, 4–6
12	Jun. 26, 2012, 5–7	Jun. 24, 2012, 5–7	Jun. 26, 2012, 3–5	Jun. 24, 2012, 0–2

Table 3.1: A list of the day and hours (in UTC) of the reference nights used for the analysis of the CLF data (LL, LM, CO) and the XLF data (LA) for each CLF and XLF epoch and FD site.

database that contains data from January 2004 to December 2012.

We searched new reference nights, one for each epoch corresponding to the period between two different cleaning of the mirror of the CLF, for each FD site. For the XLF, since the absolute calibration is performed every night, there are no cleaning events that define epochs. We split the data artificially into year-long epochs to minimize possible systematic shifts that are not tracked by the XLF calibration system. A list of the new reference nights for the CLF epochs and the FD sites Los Leones, Los Morados and Coihueco and for the XLF epochs and the Loma Amarilla site can be found in Tab. 3.3.2, as expected most of the clear night are found during austral winter.

The new database contains a new estimate of uncertainties on the VAOD profile that are now separated into *correlated* and *uncorrelated* contributions. These assignments were based on whether the effect of the uncertainty would be correlated over the EAS data sample, or would be largely uncorrelated from one EAS to the next (see table 3.3.2). The FD uncertainties correlated between different showers should be propagated to the SD energy scale by shifting all FD energies coherently by their uncertainties. This means that the correlated uncertainties propagate entirely to the SD energies.

Since the analysis method is based on the normalization of an FD events to another using the the reference night, it is not sensitive to the absolute photometric calibration of either the laser or the FD, so the calibration correlated uncertainties are those that describe how accurately drifts in the FD

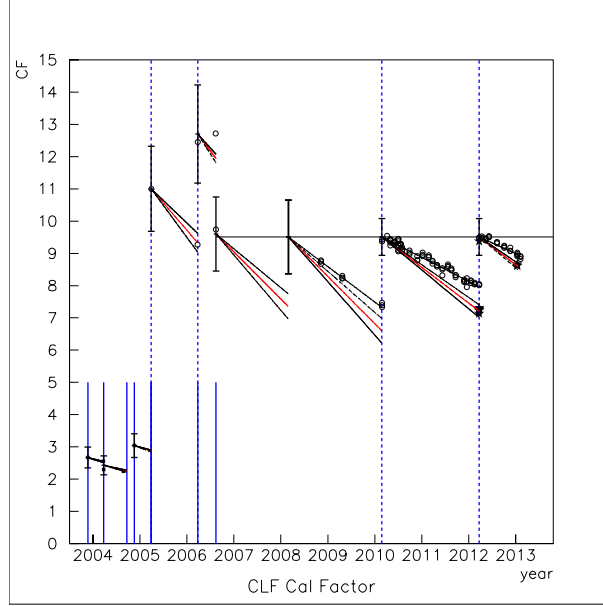


Fig. 3.11: Calibration factors for the CLF. Dashlines denote cleaning of the final tilted mirror. Solid vertical lines denote hardware changes. Open circles denote measurements made with the calibration probe placed directly over the optical table. Starred points denote measurements made at the exit of the vertical beam cover box on the roof. Calibration factors prior to 2005 were measured using the photodiode probe and are scaled to fit on this plot. The vertical error bars denote the uncertainty in the absolute calibration of the CLF.

and laser energy calibrations were tracked over the period between reference nights.

For the CLF, the 1-2.5% value corresponds to different epochs and depends on how well the effect of dust accumulation on the optics was tracked and takes into account how much the depolarization of the laser beam is stable. For XLF the value of the corresponding term is fixed (1%) because the automated calibration system tracks beam energy and polarization every day. The uncertainties due to the variability in FD calibration during the night is contained in the uncorrelated error of the relative FD calibration; the choice of the reference clear night introduces a correlated uncertainty estimated in 3%; atmospheric fluctuations within the hour cause an uncorrelated error estimated on an event-by-event basis that is about 3%, and at last a 2% uncorrelated uncertainty considers how well the parametric model used describes the real aerosol attenuation conditions.

For the calculation of the uncorrelated error on the VAOD altitude profile, the total uncertainty due to the FD relative calibration, the laser calibration

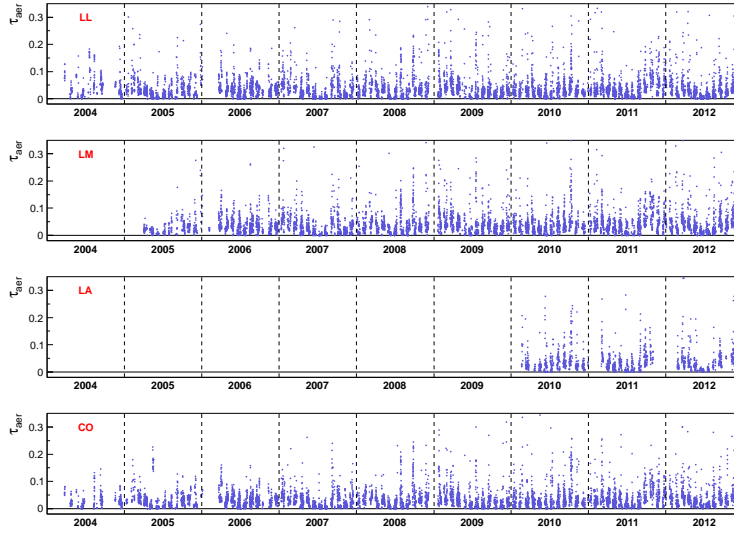


Fig. 3.12: Values of τ_{aer} at 4.5km above sea level contained in the aerosol database for all FD sites.

and the fluctuation of the atmospheric conditions comes from the quadratic sum of each term. The value obtained is used to increase and to decrease the number of reconstructed photons in the measured light profile to obtain two light profiles with a maximum and minimum number of photons; the procedure adopted to evaluate the VAOD altitude profile ($VAOD_{ERR}^{UN}$) is then applied to the new light profiles. The value of the uncertainty associated to

	Correlated	Uncorrelated
Relative FD Calibration	2%	4%
Relative Laser Energy (CLF)	1 - 2.5%	2%
Relative Laser Energy (XLF)	1%	2%
Reference Clear Night	3%	-
Atmospheric Fluctuations	-	$\sim 3\%$
Parametric Model	-	2%

Table 3.2: A list of uncertainties in the new aerosol database, separated in correlated and uncorrelated error sources. The uncertainty introduced by the parametric model refers only to the Laser simulation Analysis.

the VAOD(h) profile is:

$$\Delta VAOD^{UN} = \sqrt{(VAOD_{ERR}^{UN} - VAOD_{BEST})^2 + (\Delta_{PAR} \cdot VAOD_{BEST})^2} \quad (3.5)$$

where Δ_{PAR} is the uncertainties coming from the use of the parametric model.

Similarly the correlated error on the VAOD altitude profile is:

$$\Delta VAOD^{CO} = \sqrt{(VAOD_{ERR}^{CO} - VAOD_{BEST})^2 + ERR_{STAT}^2} \quad (3.6)$$

The $VAOD_{ERR}^{CO}$ term is calculated in the same way of the $VAOD_{ERR}^{UN}$ term but taking into account the uncertainties related to the choice of the reference clear night, to the relative calibration of the FD and the relative calibration of the laser energy. ERR_{STAT} is an uncertainty deriving from the method, it is the difference between the $VAOD_{BEST}$ profile and the second-best VAOD altitude profile found with the same method.

The effect of the uncertainties that affect the VAOD(h) on reconstructed EAS energy and X_{max} was studied moving the VAOD(h) up or down by its systematic uncertainty: it results that energy varies from +2.4% to -2.5%, and X_{max} from 0.8 to -1.2 $g \cdot cm^{-2}$ [91], the resulting shifts are lower than those evaluated in the past aerosol database release [32].

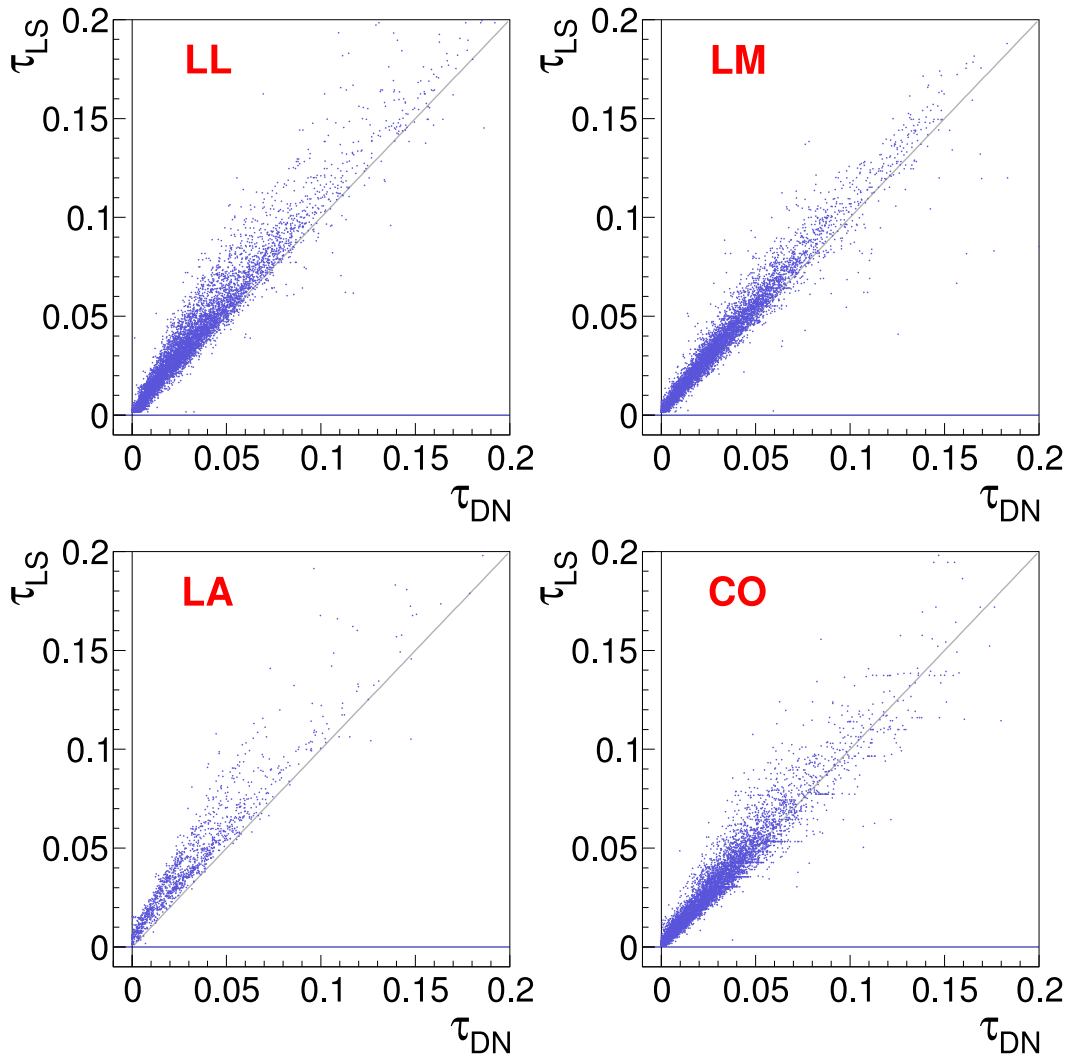


Fig. 3.13: Comparison between the values of τ_{aer} at 3 km a.g.l. obtained using the Laser Simulation Analysis and Data Normalized Analysis for all the data of the new database. The correlation is evident for all the FD sites, and differences are within the errors except for Loma Amarilla data, where the Data Normalized Analysis produces slightly different results which are under investigation from the group of the Colorado School of Mines.

3.3.3 Upgrade of the Laser Simulation Analysis

The Auger Collaboration asked to the atmospheric group to work on upgrade of the Laser Simulation Analysis in order to produce more realistic profile of aerosol optical depth taking into account the characteristics of the atmosphere in its lowest part, the planetary boundary layer (PBL), so I decided to work on this item.

The new method uses a different parameterization to describe the aerosol optical depth altitude profile adopted during the laser event simulation [92]:

$$\begin{cases} \tau_{aer}(h_1 - h_0) = -\frac{H_{aer}}{L_{aer}} \left[\exp\left(-\frac{h_1 - H_{PBL}}{H_{aer}}\right) - 1 \right] + \frac{1}{L_{aer}} (H_{PBL} - h_0) & (if \quad h_1 > H_{PBL}) \\ \tau_{aer}(h_1 - h_0) = \frac{1}{L_{aer}} (h_1 - h_0) & (if \quad h_1 < H_{PBL}) \end{cases} \quad (3.7)$$

Using the new parameterization the VAOD altitude profile presents a linear trend up to the PBL height ($h < H_{PBL}$) and then an exponential trend above it ($h > H_{PBL}$). The linearity of the VAOD profile inside the PBL is a typical assumption used in atmospheric physics; in the PBL aerosol are well mixed in height so we can assume that the aerosol extinction coefficient has an almost constant value at different altitudes.

The code has been modified and I generated a new grid of simulated laser profiles by varying L_{aer} from 5 to 50 km in steps of 1.25 km and from 50 km to 150 km in steps of 2.5 km, H_{aer} from 0.25 km to 3 km in steps of 0.25 km, and H_{PBL} from 0 to 2.5 km in steps of 0.25 km corresponding to 10164 profiles per month and to a total of 121968 simulated profiles for each FD site.

An example of the VAOD(h) profile resulting from the analysis of the same measured laser event using the 2 and 3 parameters Laser Simulation Analysis is shown in Fig. 3.14. The introduction of the third parameter in the VAOD(h) function has an effect mainly in the first part of the profile where the 3 parameters analysis profile shows a linear trend up to the PBL altitude.

Plots in Fig. 3.15 show a comparison between values of the VAOD at 3 km a.g.l. obtained using the 2 and 3 parameters Laser Simulation Analysis: results are strongly correlated. The excellent correlation of the two set of data confirms the quality of the 2 parameters procedure, and then of the data which were used to fill the aerosol database so far.

The 3 parameters analysis can be used to produce new more precise VAOD altitude profiles which will fill the future release of the aerosol database.

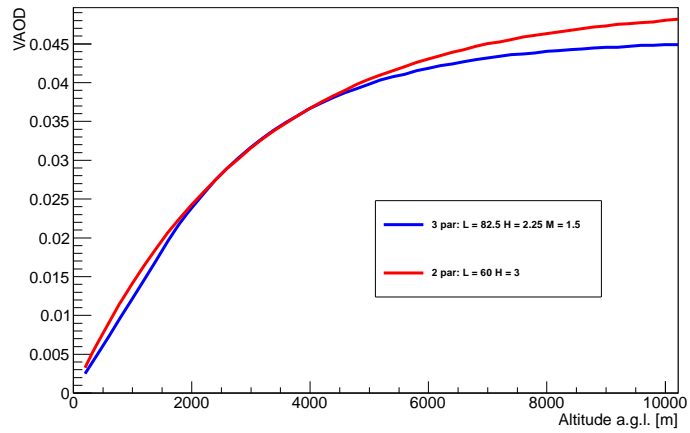


Fig. 3.14: A VAOD altitude profile obtained using 2 and 3 parameters Laser Simulation Analysis: the 3 parameters analysis profile (blue) shows a linear trend up to the PBL altitude, in this case up to 1.5 km.

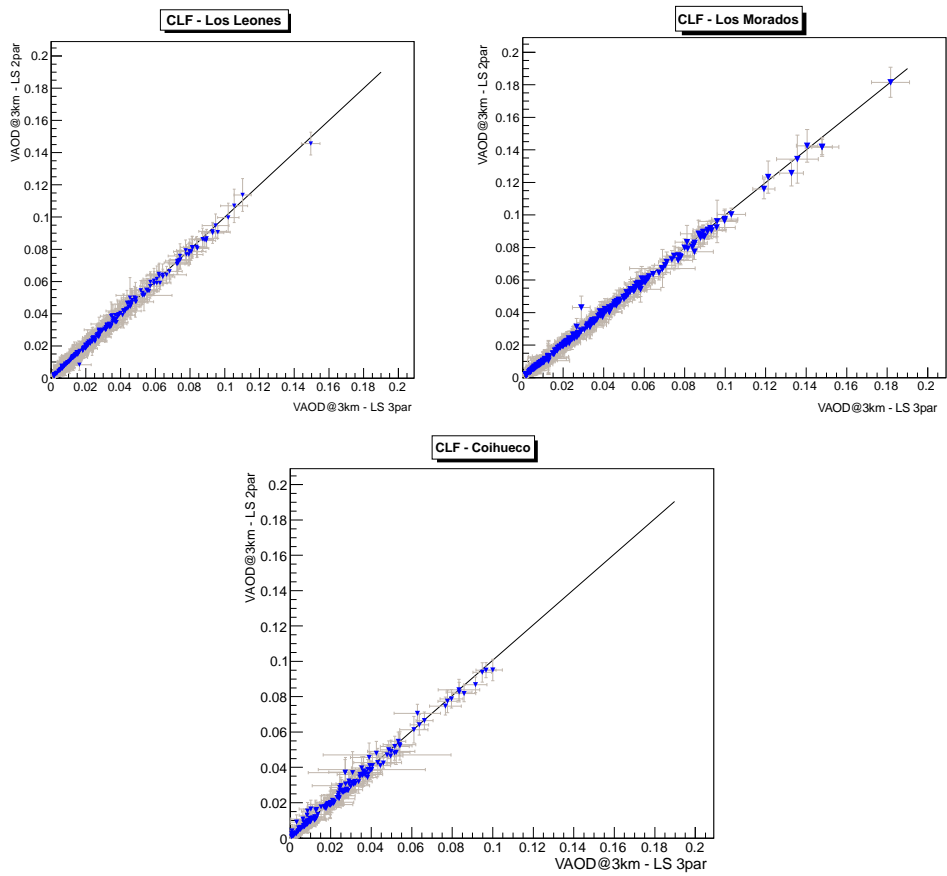


Fig. 3.15: Comparison between the values of VAOD at 3 km a.g.l. obtained using the 2 and 3 parameters Laser Simulation Analysis.

Chapter 4

The ARCADE project

4.1 Description of the project

ARCADE, Atmospheric Research for Climate and Astroparticle DEtectors, is a three year project started in 2012 and funded by the MIUR, the Italian ministry of education and university, through the program “Futuro in Ricerca - 2010 -RBFR10V192”. The project involves two research groups belonging to the *Università degli Studi di Napoli “Federico II”* and to the *Università degli Studi di Torino*, in close collaboration with some researchers of the *Colorado School of Mines* and of the *CETEMPS - Università degli Studi dell’Aquila*, and with the significant support of the *INFN - Sezione di Napoli* and *INFN - Sezione di Torino*.

Goal of the project is to characterize the optical properties of the atmosphere in the near UV, in particular the tropospheric aerosol stratification and the distribution and optical depth of clouds, topics of interest to the cosmic ray physics community and for climatology studies. The research program of this project is indeed positioned exactly between these two items, proposing to address the problem in an arid-desert like environment (Colorado) with characteristics typical of the areas where UV detectors for cosmic rays usually operate. The instrumentation chosen is on purpose redundant, similar to one commonly in use in the major cosmic rays experiments and in the atmospheric physics community, in order to assess the different systematics affecting each instrument providing simultaneous observations of the same air mass with different techniques. ARCADE compares measurements of atmospheric aerosol optical depth obtained using an UV detector with the same measurements provided by a steerable Raman and elastic lidar, performing measurements campaigns outside an ongoing cosmic rays experiment to avoid interference. This comparison will contribute to reduce the

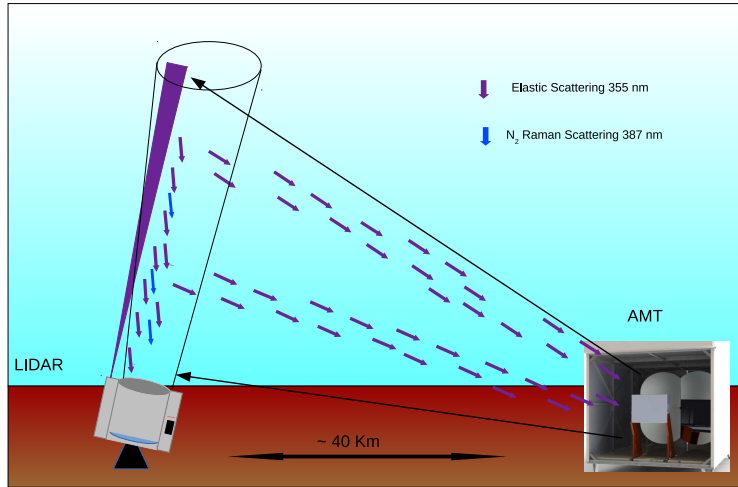


Fig. 4.1: Schematic of the experimental apparatus of the ARCADE project: the lidar is placed ~ 40 km far from the AMT. The lidar fires a laser beam and both the devices collect the light scattered by the atmosphere toward them.

uncertainties of cosmic rays detectors measurements, which inevitably affect the primary energy determination and make difficult to distinguish among primary particles.

The lidar used in the experiment has been fully designed within the project, while the device devoted to the side-scattering measurements is the Atmospheric Monitoring Telescope (AMT), a simplified fluorescence detector owned by the Colorado School of Mines and placed in Lamar (Colorado), the site where the experiment has taken place since June 2014 and is currently in acquisition. The location of the experiment is in a desertic zone in southeastern Colorado: the landscape is a flat plateau at about 1200 m a.s.l. with low air pollution, characteristics that make the site suitable for cosmic ray observations [93].

A schematic of the experimental apparatus is shown in Fig. 4.1; it consists in a steerable Raman and elastic lidar and in a UV telescope, the AMT, placed at about 40 km from the lidar. The AMT will collect the light emitted by the same laser source of the lidar and scattered by the atmosphere toward it.

The work on the project was divided among the two groups. The Naples group was in charge to work mainly on the AMT, both on the setup of the device and on the development of the software for the data analysis, and the Turin group was dedicated mainly to the lidar, from the construction to the data analysis; however both the group collaborated at every stage of the

project.

The timetable of the project can be divided in three phases: the first year was spent for the design and construction of the lidar, for testing the AMT in the laboratory of the Colorado School of Mines in Golden, and for the development of software needed for the control of the system. During the second year the construction of the lidar was completed and the instrument was tested first in Turin and then in L'Aquila, in the mean time the overall organization of the project was finalized. In the third year of the project the lidar was installed in the site of the experiment, the AMT was reassembled, and data taking started. Nowadays the experiment is in acquisition phase, fully controlled remotely from Italy and data analysis is being finalized.

I took part first hand to all the phases of the project, working on many tasks: in the next sections all the detail of the ARCADE devices and setup will be presented, and the activity that I have done will be highlighted. In the next chapter the description of the analysis methods that I developed for data analysis of both devices will be described, and some preliminary results will be also presented.

4.2 Design and construction phase

4.2.1 The lidar

The lidar used in ARCADE has been fully designed and realized within the project in collaboration with the technicians of the INFN Mechanical Workshop of Torino with the support of the INFN Mechanical Workshop of Napoli.

The mechanical structure of the lidar is extremely compact ($1.5 \text{ m} \times 0.8 \text{ m} \times 0.8 \text{ m}$) and consists in three boxes made of anodized aluminum that host the laser bench, the primary and secondary mirrors, and the wavelength separator system ("Raman block") respectively [94].

The laser source of the lidar is a Quantel Centurion Nd:YAG diode-pumped solid state laser with a second and third harmonic generation module that emits UV light at $\lambda = 354.7 \text{ nm}$, with residual at 1064 and 532 nm, at variable repetition rate from 1 to 100 Hz and average energy of 6 mJ [95]. In the first design the infrared residual component of the beam was filtered by a single dichroic mirror, the filtered laser beam passes through a beam splitter mirror that sends 5% of the light to a pyroelectric probe, *Laserprobe RjP-445* [96] read by a radiometer (LaserProbe Rm-6600) that constantly monitors the laser energy during operation: the measurement of the energy of each laser shot is needed to apply the Laser Simulation Analysis to the

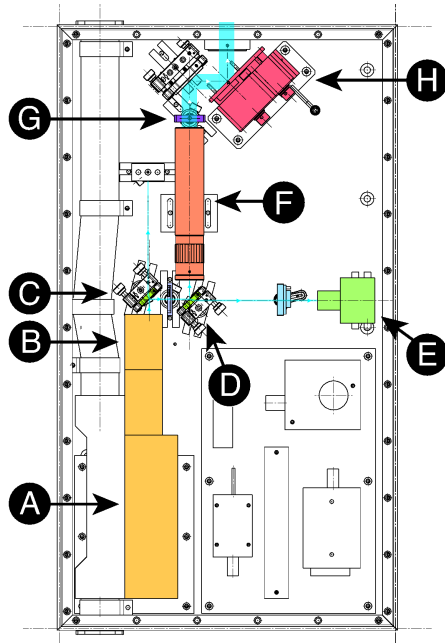


Fig. 4.2: Laser bench scheme. The laser (A) emits a ϕ 1.6 mm light beam with a full divergence of ~ 3 mrad. Light is purified by five dichroic mirrors (B,C). A beam splitter (D) sends 5% of the light to a laser probe (E). The main beam passes through a 10X beam expander (F), thus reducing the divergence to ~ 0.3 mrad. The light is then depolarized (G). The beam alignment can be finely controlled with a motorized mirror mount (H). The beam finally exits the laser box passing through a quartz window.

data collected using the AMT. A shutter and a divergent lens are placed before the aperture of the probe: the shutter is closed during lidar acquisition when the laser repetition rate is high (100 Hz). The divergent lens enlarges the spot of the laser beam and avoids damage to the probe. Accurate calculations were performed to choose the correct lens and to fix its position on the laser bench in order to send on the probe a laser beam characterized by a diameter comparable to the probe effective area and an energy density that was below the probe damage threshold.

The remaining 95% of the light reflected by the beam splitter is sent through a 10X beam expander that reduces the beam divergence to 0.3 mrad and enlarges the spot diameter to about 22 mm. A depolarizer glass is placed just after the beam expander: light emitted by the laser is vertically polarized, but for the side scattering measurements we need a random-polarized beam to assure the isotropy of the scattering process and to reproduce the behaviour of the fluorescence light.

At this stage the light is sent on a flat mirror that reflects it on another 2" flat mirror held by a two-axis motorized mirror mount [97] and finally the beam is fired into the atmosphere. The motorized mirror is controlled via software and allows the fine alignment between the beam and the receiver.

A schematic of the laser bench is shown in Fig. 4.2.

The light receiver is a 25 cm, f/3, Newtonian telescope: it consists in a parabolic primary mirror that reflects the collected backscattered light to a 45° inclined flat mirror placed along its axis just before the focus point. An iris, located in the focus of the primary mirror, fix the field of view of the telescope at a value of 3.3 mrad. Rays of light that pass the iris are then parallelized by a movable plano-convex lens and sent to the Raman block: here a mirror reflects the incoming light toward a beam-splitter which separates the N_2 Raman backscattered photons ($\lambda = 386.7$ nm) from the elastic component. The two light beams pass through a 2 nm-wide narrow band filters with transmission wavelength centered at 354.7 nm and 386.7 nm respectively and are collected by two different 2" Hamamatsu R1332 PMTs that convert light to electrical signals; signals from PMTs are amplified by a factor 20 and sampled with a 10 bit 1 GS/s CAEN DT5751 digitizer [98]. The travel of the light from the primary mirror toward the PMT is shown in Fig. 4.3: pictures result from the Geant4 simulation that I performed to study the geometry of the lidar.

The distance between the laser beam and the receiver is 301 mm. When the system is perfectly aligned the entire laser beam enters the field of view of the receiver (complete overlap) at a distance of about 250 m.

The system is fixed on a zenithal steerable mount that can rotate the lidar from 0° to 90°. The movement is handled by a Trio MC224 motion controller, which operates a servo motor, and reads the actual position of the telescope from a 13 bits absolute encoder directly mounted on the steering axis.

After the first assembling of the lidar and the first tests on the system performed in the mechanical workshop in Turin (see below for more details) the lidar was transported in the laboratories of CETEMPS in L'Aquila to carry out some tests and a direct comparison of results with a lidar that is part of the European Lidar network EARLINET [99]. During the first tests we found that the amount of the green light ($\lambda = 532$ nm) residual component of the beam was very high and needed to be further attenuated (see Fig. 4.4). It was decided to filter out this light by using a sequence of four dichroic mirrors contained in a preassembled Quantel block in addition to the one that was already installed: this setup allows the production of a very pure UV laser beam.

During the tests on the lidar in L'Aquila we also verified the acquisition system. First we noticed that the PMT collecting the elastic back-scattered light saturated in the short range and so it was not possible to acquire a clean lidar signal. The problem was solved adding some neutral optical filters just before the PMT window. In this way the return light was attenuated and the typical lidar signal appeared at the oscilloscope. A picture of one of the

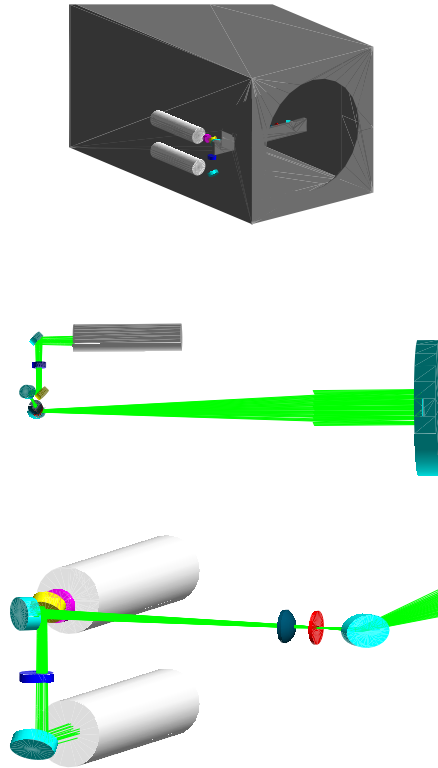


Fig. 4.3: The structure of the lidar resulting from the Geant4 simulation and the photon ray-tracing. Top: the overall structure of the lidar box. Middle: a parallel beam of light hit the primary mirror toward and photons are ray-traced toward the PMT. Bottom: detail of the light collecting system. The secondary mirror, on the left, sends the light through a movable system composed by an iris (in red) and a plano-convex lens (in grey) toward the Raman block. It is composed by a mirror (in light-blue on the top) that reflects the light toward a beam-splitter mirror (in yellow). The blue and violet disks represents the 354.7 nm and 386.7 nm narrow band filters respectively. In this case only the elastic back-scattered light is represented.

first lidar signal acquired by our system seen at the oscilloscope is shown in Fig. 4.5: a typical lidar signal decreases as the inverse of the square of the altitude. The peak in the elastic return signal indicates the presence of a cloud above the lidar since clouds scatter a great amount of the laser light; on the other hand the presence of a cloud marks also the Raman-shifted return signal, infact clouds have a great optical depth and appear as a depression in the signal.

Due to the refinements needed by our system it was not possible to obtain a

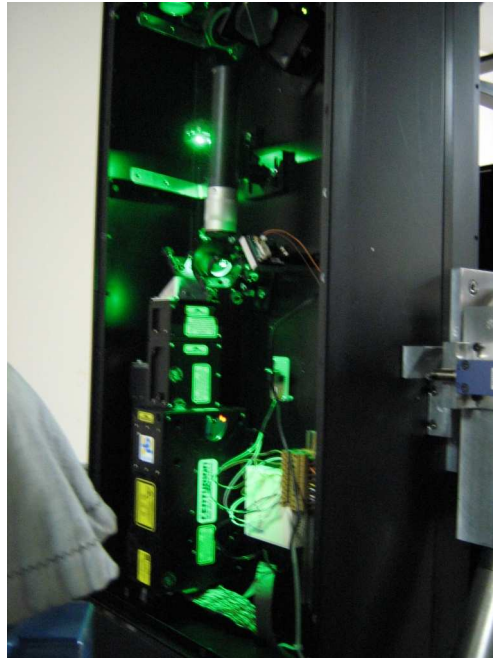


Fig. 4.4: During tests of the lidar in L'Aquila a great component of green light in the laser beam was noticed: it was removed by the use of a system of four dichroic mirrors.

significant comparison with results obtained using the CETEMPS lidar, but simultaneous acquisitions of the two systems showed the presence of clouds at the same altitude, a significant indication of the good alignment of our system.

My contributions in the Lidar development

I spent several weeks working at the INFN mechanical workshop in Turin to take part to the assembling and testing operations which were performed on each part of the system and, in addition, I worked on the developments of different software useful for the remote operations of the experiment. The main works to which I contributed are listed and described below.

- **High Voltage controller**

The power supply of the two photomultipliers of the lidar is provided by two high voltage power supply modules CAEN Mod. N 126 [100]. Each module is equipped by some input/output gates that allow the remote control of the module using NIM signals. For this purpose

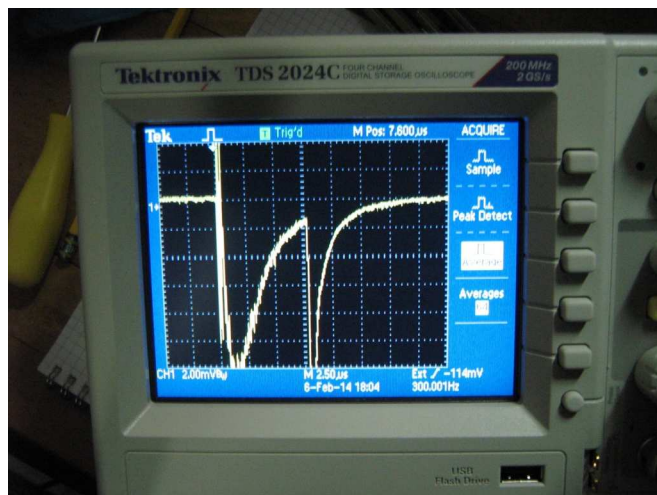


Fig. 4.5: A lidar signal acquired using our lidar: the second peak is indicative of the presence of a cloud above the lidar.

a single board computer (HV-SBC) was fully designed and assembled within the project. The HV-SBC is based on the Linux Embedded SMD module *Aria-G25* [101]: it is a System-On-Module computer integrated in a small 40×40 mm single SMD component. The main technical and software features of the *Aria-G25* are listed below:

- CPU: ARM9 400Mhz on Atmel AT91SAM9G25 SoC
- RAM: 128 or 256 MByte DDR2
- LAN: 10/100 Mbit
- USB: up to 3 host ports
- SPI: up to 2 SPI buses
- GPIO: 35 GPIO lines
- Line level: TTL 3.3V
- Boot from external microSD, SD card or serial flash
- Power supply: single at 3.3 Volt DC
- Linux Kernel version 3.16.1
- Debian Linux 7.6 “Wheezy”

The *Aria-G25* module is assembled on a PCB equipped with USB and Ethernet connections, a Digital to Analog Converter (DAC), an Analog to Digital Converter (ADC) and some TTL/NIM translators. The

PCB, shown in Fig. 4.6, was fully designed within the Naples group by Marco Cilmo with the essential help of the people of the Electronic Service of the *INFN Sezione di Napoli*. The HV-SBC is hosted in an ad-hoc NIM module.

I was assigned to develop the software for the communication between the HV-SBC and the high voltage power supply modules.

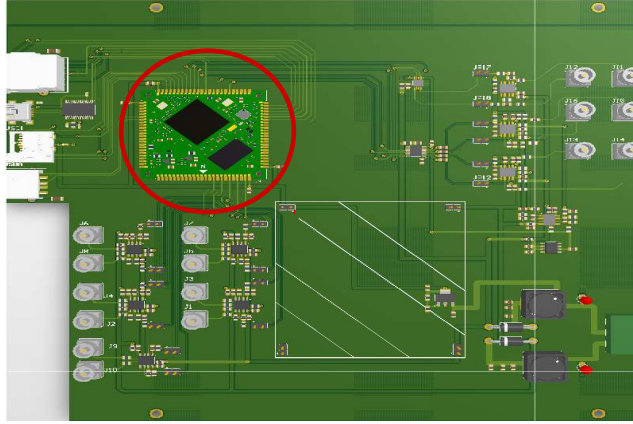


Fig. 4.6: Design of the PCB that hosts the Aria-G25 (in the red circle).

The functions of each power supply module that can be controlled remotely are:

- KILL: stops supplying power and the output voltage is quickly brought to zero.
- VSEL: selects one of two possible preset output voltage limits.
- ISEL: selects one of two possible preset output current limits.
- INH: drops the output voltage to zero at a fixed ramp-down rate until zero is reached.
- VSET: sets the value of output voltage.
- STS: monitors the status of the module, if the output current is higher than the preset maximum value (overload condition) STS becomes NIM TRUE.

For remote monitoring of the output voltage and current the device is also equipped by two output port:

- VMON: output for voltage monitoring, conversion ratio 1kV/1V



Fig. 4.7: A picture of the the high voltage power supply and of the control module in the NIM crate.

- IMON: output for current monitoring, conversion ratio 1 mA/1V

Power supply modules are connected to the HV-SBC through LEMO connectors. Since the Aria-G25 module can manage only TTL signals, and, on the other hand, the CAEN N 126 are NIM modules, each signal is converted by a translator TTL/NIM.

Functions KILL, VSEL, ISEL, INH and STS are managed by the General Purpose Input/Output (GPIO) interface of the Aria-G25; VSET is handled by a DAC and the monitor outputs VMON and IMON are read by an ADC. The DAC and the ADC are managed through the Serial Peripheral Interface (SPI) of the Aria-G25. The schematics of the connections between the power supply modules and the HV-SBC are shown in Fig.4.8 and in Fig.4.9.

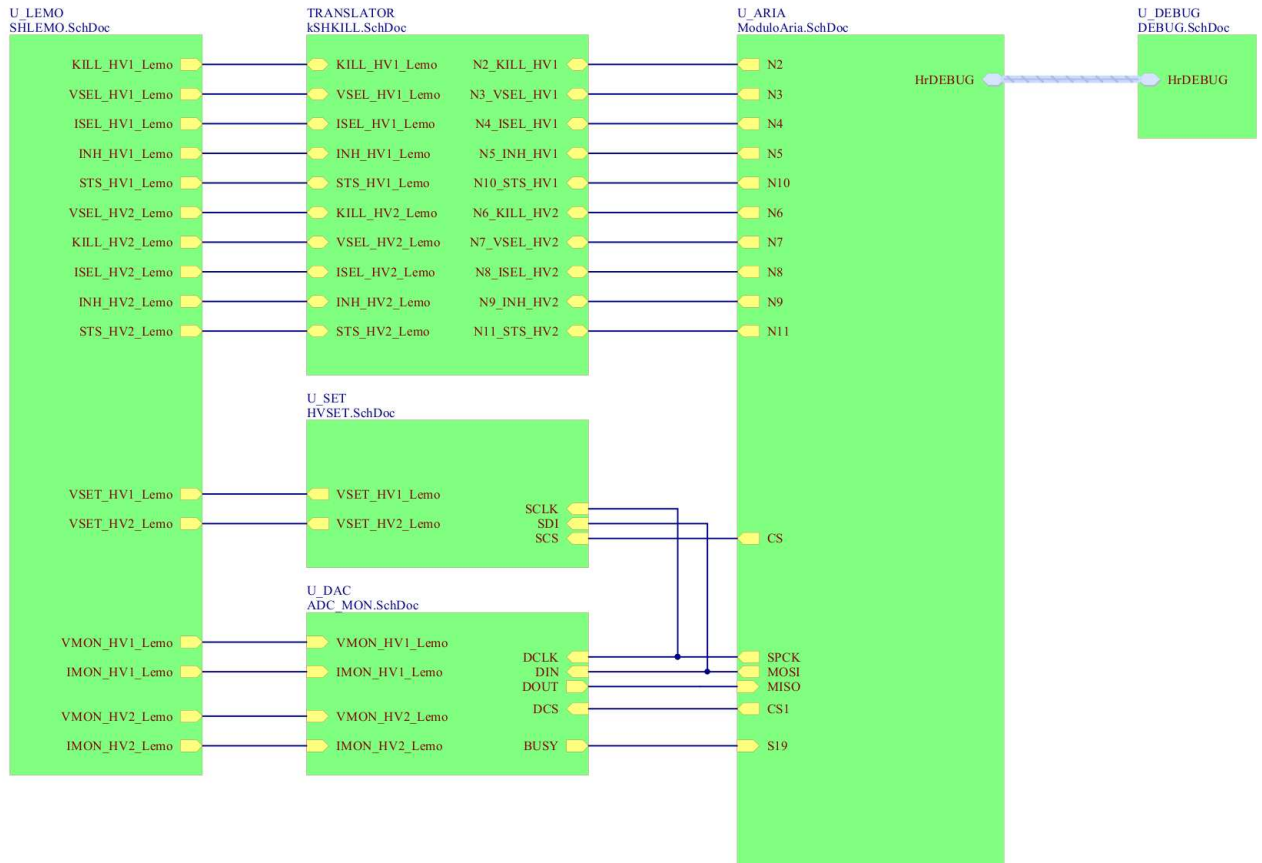


Fig. 4.8: Schematics of the connections between the power supply modules and the HV-SBC.

I have developed the code of three different C software that manage the communication between the the HV-SBC and the power supply modules: `gpio.c`, `adc.c` and `dac.c`. The HV-SBC is connected to the LAN via Ethernet and it is accesible via ssh.

gpio.c:

This software manages the GPIO lines of the Arig-G25. GPIO is a special pin present in some chip that can be set as input or output and used to move a signal high or low (in output mode) or to get the signal current status (in input mode).

The Linux filesystem path of the interface that allow working with GPIO is `/sys/class/gpio/`. The Aria-G25 is provided by 35 GPIO lines, for our purpose we use only 11 lines, that are managed by the software as text file to be read or to be written. To work with a particular GPIO the software reserves it, sets the input/output direction, writes (or reads) the high or low value , and then close it.

The program provides two different execution mode: an interactive mode where it shows the list of avaiable functions and asks to select one of these. If the choice is a writing function it asks the value to set (1 = high, 0 = low), otherwise if the choice is a reading fuction the value of the GPIO line is shown; the software can also be execute by a single shell command which includes the number of the function and the eventual value to be set. The layout of the execution modes are shown in Fig. 4.10 and Fig.4.11.

adc.c and dac.c

The communications to the DAC and the ADC are managed via SPI bus, a synchronous serial data link standard that operates in full duplex mode. Devices communicate in master/slave mode with a single master device that initiates the data frame. The SPI bus specifies four logic signals: a clock, SPCK, a “Master Out, Slave In” data line MOSI (output from master) , a “Master In, Slave Out” data line MISO (output from slave), and a chip select line, CS, that allows the selection of one of multiple slaves. In our HV-SBC the Aria-G25 is the master device and the ADC and DAC are the slave devices.

To enable and configure the SPI bus on Aria-G25 I had to edit a source file inside the Kernel tree, and, since we use two slave devices, I had to enable two different chip select pins.

The ADC we use is a Texas Instrument ADS8343 4-channel, 16-bit sampling ADC with a synchronous serial interface [102]. The power supply voltage (VCC) fixes the input voltage range ($\pm VCC/2$).

```

debarm:~# ./gpio
Select a function:
1 - Kill HV1
2 - VSel HV1
3 - ISel HV1
4 - Inh HV1
5 - Sts HV1
6 - Kill HV2
7 - VSel HV2
8 - ISel HV2
9 - Inh HV2
10 - Sts HV2
11 - Busy ADC
12 - Overload OFF HV1
13 - Overload OFF HV2
14 - Read Value VSel HV1
15 - Read Value VSel HV2
-----> 6
-----> Kill HV2
Select 0 - 1? ----> 1

```

Fig. 4.10: Interactive mode layout of the gpio.c programme: in this example the user chose to activate (1) the function KILL (6) on the second power supply.

```

debarm:~# ./gpio 5
Sts HV1 1

```

Fig. 4.11: Single-line mode layout of the gpio.c programme: in this example the user chose to read the value (1 = overload) of the function STS (5) on the first power supply.

```

debarm:~# ./adc
Select channel :
 1 - V_Mon HV1
 2 - I_Mon HV1
 3 - V_Mon HV2
 4 - I_Mon HV2
----> 1
Voltage: 1200 V

```

Fig. 4.12: Interactive mode layout of the `adc.c` programme: the user selects a channel to be read and the associated value is shown.

We use the ADC to read the voltage and current output of the power supplier, and since the PMTs need 1200 V and the VMON and IMON conversion rates are 1kV/1V and 1mA/1V, we decided to set the VCC at 5 V, so we are able to read output voltage up to 2.5 kV and current up to 2.5 mA.

Each communication between the Aria-G25 and the converter consists of eight clock cycles: one complete conversion can be accomplished with three serial communications, for a total of 24 clock cycles. The first eight cycles are used to select the active input channel of the input multiplexer, the next 16 clock cycles accomplish the actual analog/digital conversion. The output data from the ADC is in Binary Two's Complement format.

The software that I have developed, `adc.c`, controls the ADC in half-duplex mode using the C functions `write()` and `read()` to transmit the one-byte word that selects the channel that has to be read (VMON_HV1, IMON_HV1, VMON_HV2, VMON_HV2) and to receive the two one-byte words corresponding to binary value of the voltage of the selected channel. Finally the programme converts the data words in a decimal number.

The device we use to set the voltage on the power supply modules are the Linear Technology LTC2602 dual 16 bit DACs that use an SPI compatible 3-wire serial interface [103]. The digital-to-analog transfer function is:

$$V_{OUT} = V_{REF} \cdot (k/2^N), \quad (4.1)$$

where k is the decimal equivalent of the binary DAC input code, N is the resolution (16 bit) and V_{REF} is the voltage at reference, that we

```
debarm:~# ./dac
Select HV-PowSupply (1 or 2) : 1
Set V (kV): 1.2
```

Fig. 4.13: Interactive mode layout of the `dac.c` programme: the user first selects one of the two HV power supply module, and then set the value of the voltage.

fixed at 2.5 V.

The communication between the Aria-G25 and the DAC consists in the transmission of three one-byte binary words. The first word is used to select one the two DAC and then the power supply to which set the voltage and the command to execute on the DAC, the other two words contain the binary value that corresponds the value of voltage express in decimal units.

The software `dac.c` manages the DAC in duplex mode using the function `ioctl()`, a system call for device-specific input/output operations. The programme calculates the decimal to the value to set, “k”, according to eq. 4.1, and converts it in two binary words.

Also the `adc.c` and the `dac.` programmes implement two different layouts, interactive or a single command mode. The interactive layouts of the two software are shown in Fig. 4.12 and Fig. 4.13.

- **Radiometer remote control**

The laser bench of the lidar is provided by a laser probe used to monitor the energy of each lases shot during the low frequency acquisitions with the AMT; the response of the probe is read by a radiometer LaserProbe Rm-6600. I worked on the development of a C/C++ software for the remote control of the radiometer; the software manages the acquisition of data from the probe and their codification and trasmission to the single board computer to which the radiometer is connected.

Data are transferred via serial communications, through a RS-232 serial cable, so each word of data is sent or received one bit at a time. The speed of the serial data is most often expressed as baud rate (“baud”). This just represents the number of ones and zeroes that can be sent in one second.

The factory setting of the radiometer is:

- Baud Rate: 9600 baud
- Data bits: 8
- Parity bit: None
- Stop bit: 1

The programme includes the library `<termios.h>` that defines the terminal control structure and allows the use of the POSIX terminal (serial) interface for set parameters such as baud rate, character size, and so on.

The Rm-6600A follows a question and answer command technique. If a command is sent to the instrument with no parameters it will return the current setting. If a command is sent followed by parameters then, those values will be used in the function.

The reading of the radiometer is enabled by an external trigger, in this case the software reads the value of the energy of the laser shot and stores it in a file text containing the time of the shot.

- **Assembly and alignment of the lidar**

When the construction of the mechanical parts of the lidar (see Fig. 4.14) was finished we managed the assembling of all the optical and electrical equipments. A crucial job was the mounting of the mirrors of the lidar: mirrors were glued on the mechanical supports using a bi-component epoxy glue that is resistant to high temperature changes, since the temperature in the experiment sites typically ranges from -20°C in winter to $+40^{\circ}\text{C}$ in summer. Mirrors of the lidar are shown in Fig. 4.15. The primary parabolic mirror is glued on a movable support: thanks to a system of screws the mirror axis can be moved in order to be aligned to the successive optical components.

The alignment procedure is one of the most critical point of the lidar setup. The position of the secondary mirror and of all the optical components of the Raman block is fixed, so the only parts of the lidar that have an adjustable position are the primary mirror, the iris and the plano-convex lens (see Fig. 4.3). An optimal alignment assures that the light collected by the primary mirror is totally sent to the PMTs: if the system is misaligned light can hit the structure of the Raman block producing a shadow in the final image. Moreover the optimal operation of the narrow band filters is guaranteed only if light direction



Fig. 4.14: The lidar box before and after the assembly.



Fig. 4.15: Top: the primary parabolic mirror and its support. Bottom: the secondary mirror and the mirror at the entrance of the Raman block on their support.

is perfectly parallel (within $\sim 5^\circ$) to the filter axis, otherwise the filter transmission coefficient changes.

To align the lidar we used three self-leveling *Bosch GPL-3* laser level which project a fixed laser light along the horizontal and vertical axis. The levels placed on the top of the lidar receiver send vertical beam of light toward the primary mirror; using the screws placed in the rear of its support the mirror is moved until the image of the three laser spots appear centered in the secondary mirror. At this point a fine

adjustment of the position of the iris coupled to the plano-convex lens allow to focus the resulting beam. The alignment is considered satisfying when the images of the lasers are clearly resolved at the PMTs apertures. The procedure is repeated illuminating different part of the primary mirror moving the positions of the laser levels, to verify if all the light hitting the mirror is collected by the PMTs.

Once the best alignment configuration was found, we verified its resistance to the lidar rotation: the lidar was continuously rotated for a entire night and the alignment was preserved.

The laser levels are also used for the alignment of the lidar UV laser beam to the receiver. Beams of the levels and of the UV laser are fired on a target and the distance between the spots is measured; the operation is repeated moving the target in several different position far from the laser sources. The direction of the UV laser beam is adjusted moving the motorized mirror placed in the laser bench until the distances between the two laser beams is almost the same in all the position of the target.

Once all the system was verified, it was prepared for shipping.

4.2.2 The Atmospheric Monitoring Telescope

The Atmospheric Monitoring Telescope (AMT) is a telescope for the detection of UV light owned by the Colorado School of Mines. The telescope was built during 2008 with spares recovered from the HiRes experiment for the R&D of the Auger North experiment and was used for atmospheric research in 2010-2011 [104]. The AMT is placed in the region near Two Buttes at about 40 km from the laser source of the lidar.

The AMT is composed by a 4-segment spherical mirror having a total area of 3.5 m^2 , and by a camera, placed in its focal plane, equipped with three columns of sixteen photomultipliers with hexagonal window and a field of view of 1° (see figure 4.16), resulting in a total field of view for the camera of about $3\text{--}3.5^\circ$ in azimuth and about 14° in elevation. Light of the lidar laser scattered by the atmosphere reaches the AMT as a parallel beam, photons coming from the same direction in the field of view of the AMT are reflected onto a single spot on the camera.

The PMTs, Photonis XP3062 (the same type used at the Pierre Auger Observatory), are sensitive in a wavelength region from around 300 to 650 nm and the quantum efficiency reaches a maximum of 30% around 375 nm. The PMTs are supplied with the high voltage up to 1200 V and with $\pm 5 \text{ V}$ for the pre-amp electronics.

A UV filter is placed in front of the camera to reduce background light:

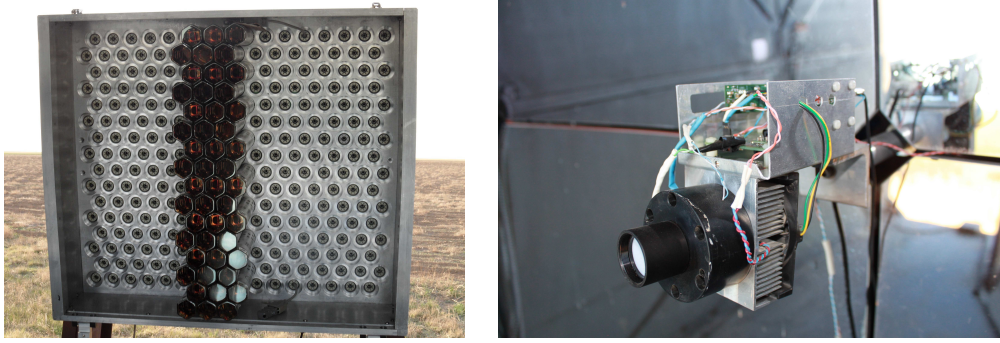


Fig. 4.16: Left: AMT camera equipped with 3 columns of XP3062 photomultipliers. Right: An LED source installed in the middle of the four segments of the mirror is used to calibrate the PMTs.

the value of the transmission has a maximum of $\sim 80\%$ at around 360 nm, and falls to less than 20% for wavelength above 420 nm.

An isotropic LED source is installed in the middle of the four segments of the mirror. The LED facility emits uniform and stable UV light across the camera and it is used to perform a day by day relative calibration of the PMTs and electronics response to a fixed amount of light. The stability of the LED is monitored by the use of a photodiode.

The PMTs readout is based on the data acquisition electronics designed for the HEAT telescopes of the Pierre Auger Observatory [44]. The sampling rate of the digitizing system is 20 MHz and the length of the recorded data is 100 μs , resulting in 2000 data bins with a bin width of 50 ns.

The DAQ is triggered externally, either by the signal of a GPS device in order to synchronize the acquisition with laser firing, or from the signal of the UV LED system used for calibration.

The AMT telescope is housed in a dedicated waterproof container with automatic and remotely controlled doors, as shown in figure 4.17. The container is inclined to obtain an angle of elevation of the telescope of 8.72° from the horizontal. With this setup the light of the laser of the lidar enters the field of view of the camera at about 1.5 km above ground level and exits at an altitude of ~ 10.8 km.

Within the ARCADE project, the camera of the AMT has been moved to the laboratory of the Colorado School of Mines in Golden, Colorado, at the end of 2012 to verify and upgrade it after the long period of inactivity. During this period, the Data Acquisition System has been improved and a new LED facility has been installed [105].



Fig. 4.17: The AMT: on the left, the 4-segment spherical mirror and the camera housed within the waterproof shelter. The office container next to the telescope hosts all the computers.

4.3 Implementation phase

4.3.1 Set-up of the AMT

In May 2014 we moved the camera of the AMT from Golden to Lamar for the reassembling, and the functionality of the whole camera of PMTs and LED system have been tested on site.

The operations for data taking and for the safety controls of the AMT are managed by several computers. A main server works as external internet access point for all the devices which are connected via a local network, and is provided by an extra access system (I-DRAC) in case of failure. The different components and their main functions are shown in Fig. 4.18.

- DAQ computer takes care of data acquisition;
- LED SBC manages the firing of the LED, sets the lengths and widths of LED pulse, and generates an external trigger signal for every LED shot that can be used to trigger the data acquisition;
- AMT SBC controls through an RPC the procedure of opening/closing of the door, the power to the camera and the high voltage of the PMTs. A weather station, connected to this SBC, provides measurements of temperature, wind, and precipitation every 5 seconds: a safety daemon on the AMT SBC checks if the values for wind and rain are within the

safety margins, otherwise the AMT SBC closes the door and stops the PMTs power supply;

- MAIN SBC controls the nightly operations. From there, commands can be sent to both the AMT and the LED SBC. The MAIN SBC includes a GPSY-II board [106] that is connected to a GPS antenna on the office container. The data acquisition can be triggered by this GPS signal in coincidence with lidar laser shots: the GPSY-II boards of the AMT SBC is synchronized to the lidar SBC, and generates the trigger signal after a fixed time ($130 \mu s$) compared to the other.

Two UPS systems are used to prevent the computers to shutdown in case of temporary power failures.

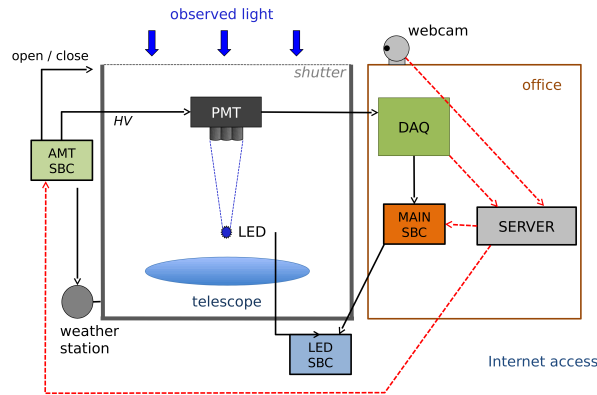


Fig. 4.18: The AMT scheme.

4.3.2 Set-up of the lidar

The lidar and all the devices useful for its operations were shipped in the United States of America inside a container and arrived in Lamar in May 2014. Technicians from Turin were involved in the preparation of the apparatus in situ. The lidar is hosted in an astronomical dome provided by a remotely controlled motorized aperture. The lidar and the dome were assembled on a platform that was placed on the roof of the container by a crane. Accurate measurements were performed to orientate the dome aperture, and then the lidar, in the direction pointing the AMT. The lidar control station was prepared inside the container [107].



Fig. 4.19: The lidar is mounted inside an astronomical dome placed on the roof of a container.

The lidar is completely controlled by remote: a schematization of all the connections between the computers and hardware is shown in figure 4.20. The Lidar-PC allows the remote access to the apparatus via internet connection and manages the steering of the lidar, the motion of the motorized mirror in the laser bench, the aperture of the dome, and the data acquisition through the digitizer. A single board computer hosting another GPSY-II card is devoted to the control of the laser firing. The SBC is connected to the laser control module and fix the energy of the laser beam setting the Q-switch of the laser. The external trigger signal generated by the SBC is sent to the laser fixing the repetition rate and the firing time, and enables the reading of the radiometer and of the digitizer. The module that controls the high voltage power supply of the PMTs is also connected to the SBC. The apparatus is equipped by a webcam and a weather station to control the condition and the device remotely.

All devices are connected to an RPC, remote controlled power supplies, that can switch the power on or off, and are controlled via the network. The Lidar-PC, all the SBCs and the control devices are connected to an uninterruptable power supply (UPS) that in case of power failure allows to shut everything down properly and to close the dome.

A web page was designed to manage the turning on/off of all the devices and to monitor the status of the lidar through the webcam and the weather station. Some screenshots of the web page are shown in Fig. 4.21.

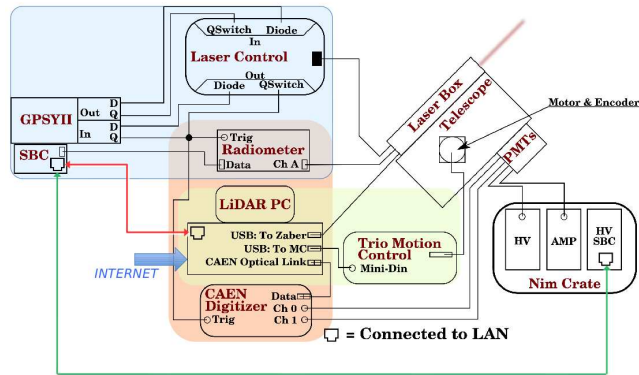


Fig. 4.20: The schematic of the lidar system.

4.4 Data taking

The AMT and the lidar system are manually operated from Italy during moonless night. Both the devices can be set up to take measurements automatically throughout the night using a list of commands.

Data taking started in July 2014 and will continue throughout the 2015, but several adverse events disturbed the regular operations. A failure of the high voltage power supply of the AMT occurred in August 2014 stopped the AMT acquisition until it was repaired in September, and the extremely low temperature (less than -20°C) in December/January made the laser unusable, requiring the installation of some heaters inside the laser bench at the end of January.

The operations for data acquisition start at sunset, or after the moonset. First the weather conditions are checked using the weather stations installed in both the lidar and AMT sites, and, if they are good, a variety of measurements is performed during the night, until sunrise or moonrise repeating the schedule shown in Fig.4.22.

Before starting the measurement, a number of laser shots are fired with the aim of checking and correcting the lidar optics alignment. The best set up is obtained by tilting the motorized mirror mount inside the laser box around two axes until the position that maximizes the signal over noise ratio at far distances is found.

After the fine alignment process, the laser fires 400 vertical shots a 4 Hz for side-scattering measurements with the AMT. The data acquisition of the AMT is triggered accordingly by the GPS on-board the Main SBC, corrected

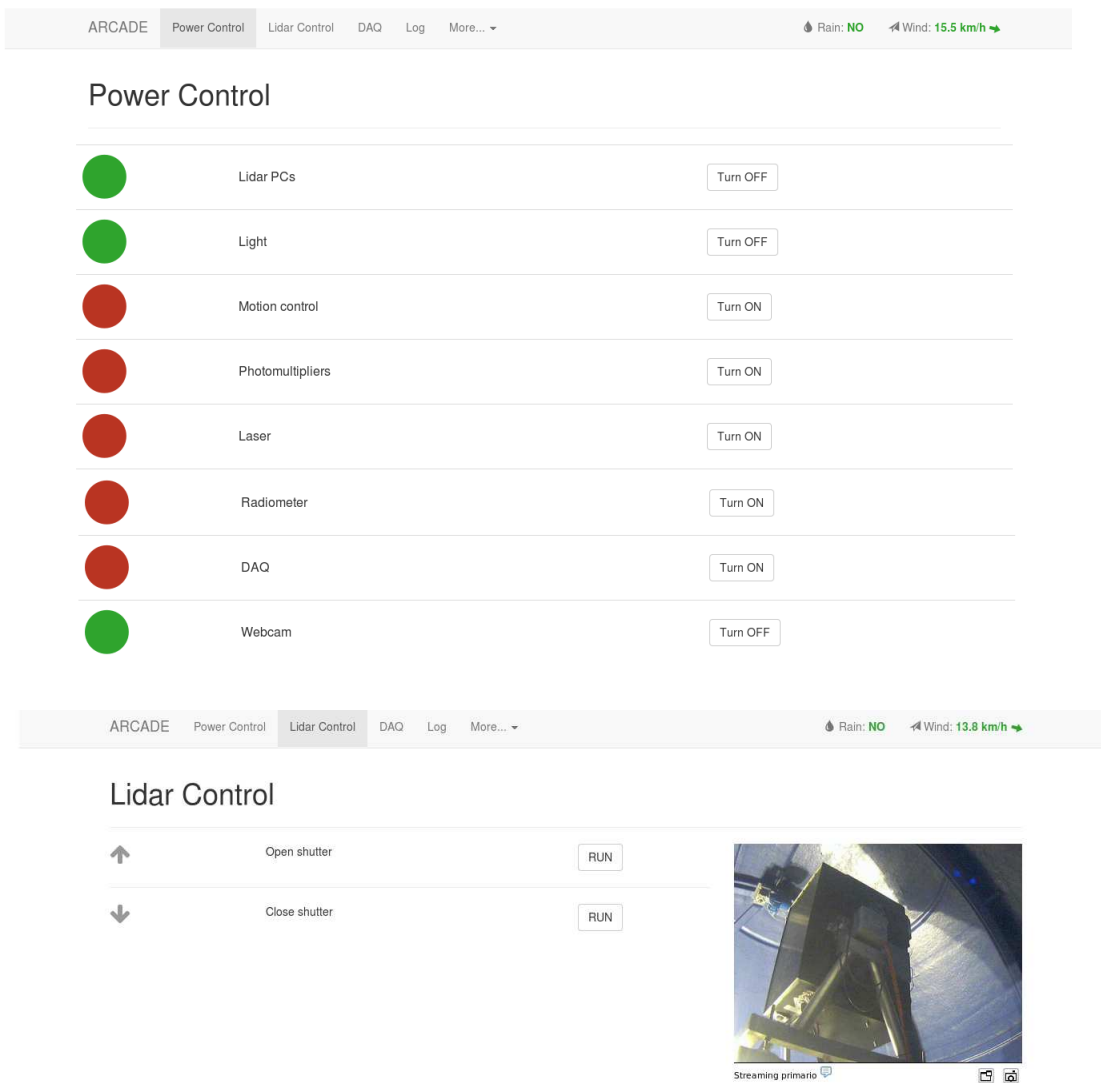


Fig. 4.21: Screenshots of the ARCADE webpage used to control the lidar.

for the time the light takes to reach the AMT, around $130 \mu s$. After each AMT acquisition the calibration of the PMTs camera is performed firing 240 LED shots. At this stage the long time Raman acquisition starts: the laser fires three series of 30000 laser vertical shots at 100 Hz for about 20 minutes. The AMT and Raman acquisition are repeated again and then the lidar is tilted at discrete positions in order to perform a multi-angle analysis with the

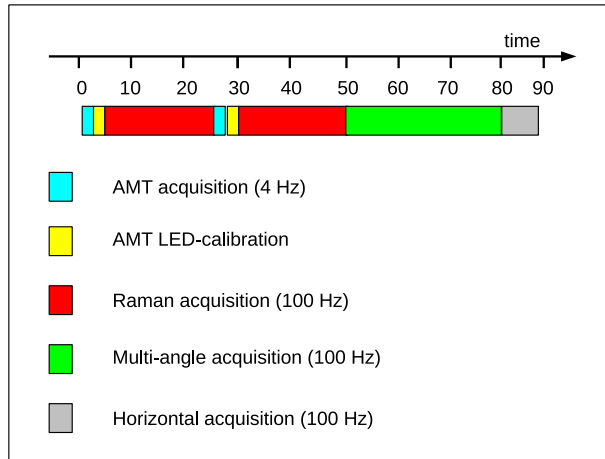


Fig. 4.22: Time schedule of the different measurements performed during the night.

elastic channel. The laser fires 30000 shots at 100 Hz with the lidar inclined at 0° , 30° , 40° , 46° , 51° respect to the zenith. These data can also be useful to apply the Raman analysis on inclined shots. At the end of the discrete scanning sequence the lidar fires and acquires a series of laser shots in the horizontal direction; these measurements are useful to calculate the value of α_{aer} at ground level, and then to check the horizontal uniformity at ground. Acquisitions in this position can be also used to interpolate the aerosol optical depth in the zone where the overlap function is not complete and, if the condition of horizontal uniformity is met, to estimate the distance at which the overlap function becomes constant. Then the sequence of measurement is repeated for all the night.

Chapter 5

ARCADE data analysis

5.1 Introduction

The goal of the ARCADE project is the comparison of the experimental techniques for the measurement of aerosol optical depth altitude profile adopted in cosmic rays experiments. The experimental apparatus, consisting in an UV detector, the AMT, placed at ~ 40 km from a steerable elastic and Raman lidar, allows the application of different analysis methods. Data from side-scattering measurements are handled by the Laser Simulation Analysis adapted for the AMT, and, concerning lidar data, Raman-shifted signals are treated applying the “Raman analysis”, and the multi-angle analysis is adopted to study the elastic signals.

During my PhD I have developed the software for the AMT-Laser Simulation Analysis and for the Raman analysis: in the following sections I will describe in details the principles of these methods and the procedure for the data analysis, showing some preliminary results. The multi-angle analysis applied to elastic lidar signals was developed by the group of Turin, therefore I will include in this thesis only the explanation of the technique.

5.2 VAOD measurements using the AMT

The analysis of side-scattering data acquired by the AMT is performed using a custom version of the Laser Simulation Analysis developed by the Auger group of Naples and largely described in sec. 3.2.

The AMT analysis differs from the one performed in the Auger experiment in at least two main aspects: first of all the simulation of the AMT is different from the one of the Auger fluorescence detector and therefore I developed

a full simulation of this detector that is described in the following section. Nevertheless, the procedure to calibrate the AMT using a close by laser facility and an LED calibrated source allows to fix the energy scale between simulated and measured laser events and avoids the use of the normalization to a reference night.

5.2.1 Geant4 simulation of the AMT

The simulation process adopted to generate simulated laser light profiles using the AMT is the same used in the Pierre Auger Observatory except for the modules that define the detector and the ray-tracing of the photons through it.

I developed a new module that performs a Geant 4-based simulation of the AMT, the *TelescopeSimulatorAMT*, starting from a module included in the Auger Offline framework, the *TelescopeSimulatorLX*. The new module uses the Geant4 version 9.6.0 and is fully compatible with the Auger Offline software. The simulation exploits the Geant4 capabilities to realistically describe complex 3D geometries and its ability to simulate the relevant optical processes, such as refraction and reflection at medium boundaries, scattering and absorption.

The module is composed by several C++ classes; those related to the simulation of the geometry of the telescope are listed below:

AMT_G4DetectorConstruction

AMT_G4Camera

AMT_G4Mirror

AMT_G4PMT

AMT_G4Filter

According to the rules of Geant4, the geometry of the detector is constructed defining a number of volumes. The largest volume, the World, contains all the others. Each volume is created by describing its shape and its physical characteristics, and is placed inside a containing volume, the mother volume. The volume of each part of the detector is shaped by composition of some elementary solids that are implemented in Geant4 as primitive classes.

AMT_G4DetectorConstruction is one of the mandatory user initialization classes and derives from the abstract base class “G4VUserDetectorConstruction”

provided by Geant4. This class manage the “construction”of the elements composing the telescope and sets their positions. I developed also the code for the detailed description of each part of the telescope in dedicated classes (Camera, Mirror, PMT, Filter).

Mirror: The mirror is composed by four identical elements, was implemented. Each element is a portion of a spherical cap with a particular shape. The curvature centre of each mirror segment coincides with the curvature center of the composed mirror. The exact geometry of each mirror segment was implemented taking advantage of the Geant4 capabilities for building new solids through boolean operations: each element corresponds to the subtraction of a parallelepiped-shaped box from a hollow sphere; the resulting solid is then intersected with two another boxes. The single mirror segment is then duplicated, and the copies are properly rotated to assemble the entire mirror (see Fig. 5.1).

Camera/PMTs: The PMT windows were implemented as lime-glass hexagons, containing the metallic photocathodes. 48 PMT windows and photocathodes were placed on the plane surface of the camera: the camera is placed in the focus of the mirror, and the arrangement of the PMTs on the camera results from direct measurement made on the actual AMT camera. The vertical supports of the camera were also implemented in the simulation.

Filter: The filter was implemented as a glass that transmits the 80% of the light.

The main constituents of the AMT constructed in the Geant4 simulation are shown in Fig. 5.1.

As in the Auger FD simulation sequence, photons in the laser beam are generated and transported to the AMT aperture (“diaphragm”). The *TelescopeSimulatorAMT* module reads photons at diaphragm resulting from the *ShowerPhotonGeneratorOG* module, tracks them through the Geant4 telescope simulation, and estimates the number of photo-electrons generated at photocathode of each PMT for each time bin.

The total signal in each pixel and time bin is then computed multiplying the number of photons by a weight that takes into account the maximum number of photons per time bin which are tracked through the detector.

The tracking of photons through the assembled telescope is illustrated in Fig. 5.2.

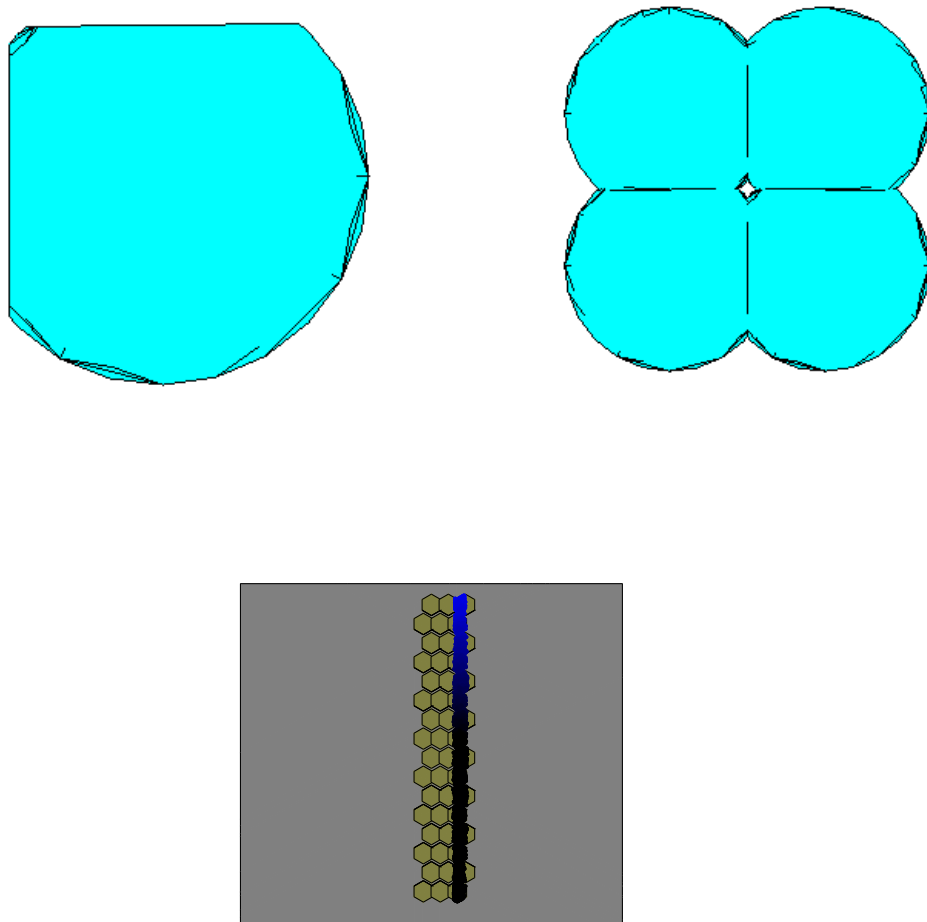


Fig. 5.1: Elements of the AMT resulting from the Geant4 simulation. Top: on the left, one of the four spherical segments that compose the mirror of the AMT drawn on the right. Bottom: simulation of the AMT camera containing 3 columns of 16 exagonal PMTs: the black and blue points on some PMTs represent the “hits” of the photons.

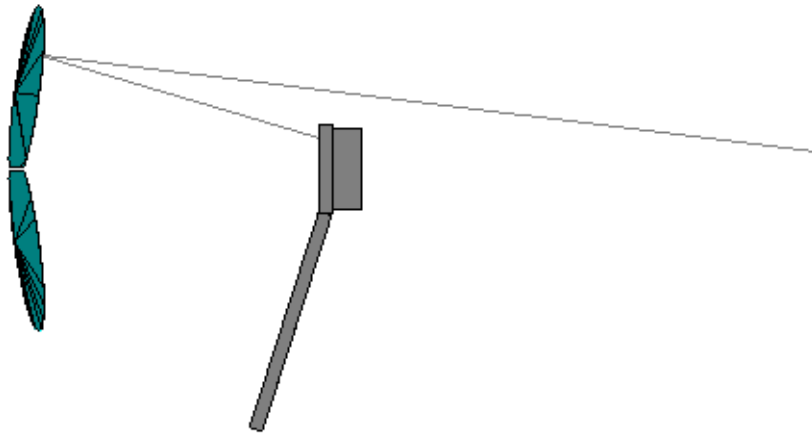
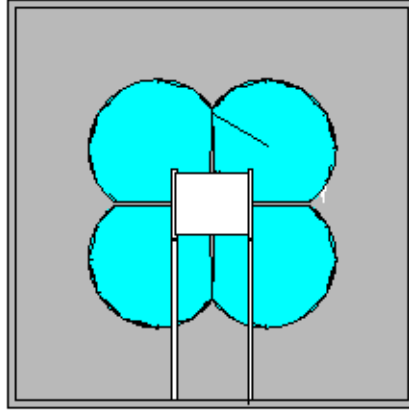


Fig. 5.2: Top: the AMT geometry resulting from the Geant4 simulation. Bottom: example of the ray-tracing of a photon.

5.2.2 AMT calibration

During a long time campaign acquisition the response of a complex detector like the AMT can mutate due to many reasons, such as changes in the PMTs gain or accumulation of dust on the mirror. To take into account any possible variation, relative and absolute calibrations of the AMT are regularly performed.

The relative calibration uses an UV LED source mounted in front of the camera that was provided by the Colorado State University. Several layers of diffuser material are used to make the light almost isotropic when it reaches the camera. The LED was calibrated in lab and the stability over time of the intensity of the source was verified.

The LED is fired 240 times at a frequency of 4 Hz, just after the AMT data taking, providing a set of calibration data for each set of laser shots. The calibration constant (K_i^{FF}) is calculated for each AMT pixel by dividing the averaged signal of each PMT (S_i) for the averaged signal of a reference PMT (S_0):

$$K_i^{FF}(t) = \frac{S_i(t)}{S_0(t)} \quad (5.1)$$

in this way a flat field correction is applied to the camera. Fig. 5.3 shows the different responses of some pixels at the LED pulse before the flat field correction.

To take into account any possible change over time of the response of the PMTs the calibration factor of each pixel is normalized to the ratio between the value of the averaged signal of the reference PMT measured in that calibration set with the average signal recorded by the same PMT in a

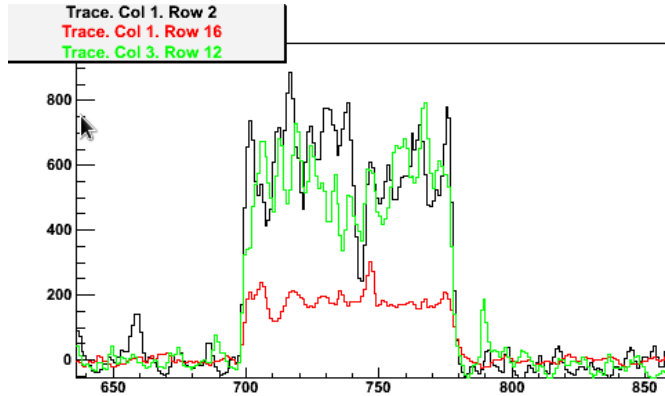


Fig. 5.3: Responses of different pixel to the isotropic light of a LED pulse.

reference night ($S_0(t_0)$):

$$K_i(t) = \frac{K_i^{FF}(t)}{S_0(t)/S_0(t_0)} \quad (5.2)$$

An absolute calibration of the AMT is done in periodic intervals every few months using a calibration laser system. A first campaign of measurements was performed in October 2014, a second in January 2015 and the next one is planned in May 2015. The laser is driven out into the field approximately 3 km in the field of view of the AMT and fires vertical shots at different energies as low as 10-15 μJ to avoid saturation of the PMTs. The light scattered by the atmosphere is collected by the AMT according to the procedure followed when the laser of the lidar is used.

The aerosol attenuation can be neglected at such short distances from the AMT, and since Rayleigh scattering from the molecular component of the atmosphere is known, the flux of photons arriving at the telescopes can be predicted very accurately once the energy of each shot is measured by a probe. The calibration laser is equipped with two energy probes, one monitors the energy of each shot measuring a percentage of the beam, and another is used to take measurements of the whole energy of the laser beam sent to the sky. We use the data acquired using the calibration laser to fix the energy scale between simulated and measured laser events: Rayleigh scattering is well implemented in the simulation code, and hourly GDAS data are used to extract the concentration of molecules in the atmosphere.

5.2.3 AMT data analysis

The procedure for the measurement of VAOD profiles from laser data using the AMT is based on the Laser Simulation Analysis method.

A grid of simulated light profiles is generated by varying the atmospheric aerosol conditions: the different content of atmospheric aerosol is defined in the parametric formulas in eq. 3.7. Rayleigh scattering and molecular attenuation are evaluated using a GDAS database containing the value of the atmospheric state variables recorded everyday in Lamar.

An example of the output of the simulation chain is shown in Fig. 5.4. Since the distance of the AMT from the laser source is greater than that of the Auger FD sites from the CLF the number of ADC counts is lower than in simulation related to Auger data (compare Fig. 5.4 and Fig. 3.1). To reduce the fluctuation of the signal we generate average profiles obtained from 200 simulated laser shots.

The procedure for the reconstruction consists in averaging the simulated or measured light profiles contained in the raw data. A crucial step in the

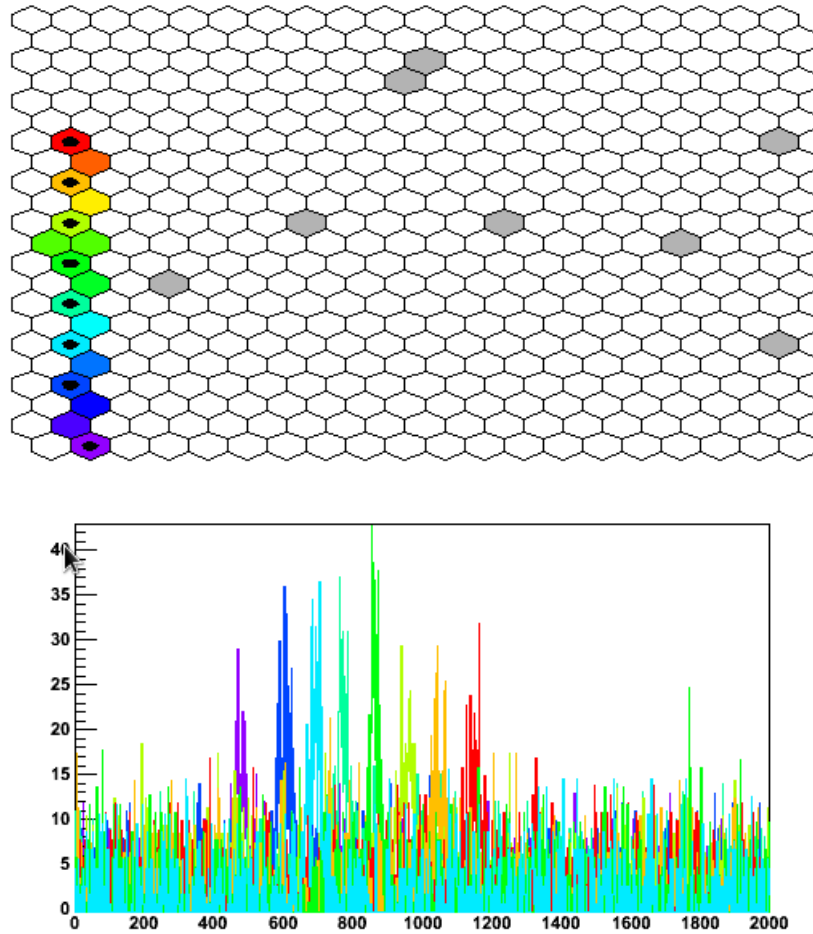


Fig. 5.4: A simulated laser event as seen by the AMT. On the left, a vertical trace fires the PMTs of the AMT camera. The event viewer is the same adopted for the Auger FD, the AMT is provided by only three columns of 16 PMTs, the other columns and row of PMTs are not implemented in the simulation: On the right panel, the ADC signal corresponding to the selected pixels.

reconstruction process is the use of the calibration factor evaluated for each PMT as described above. A calibration file is generated for each pixel of the camera. The file contains a list of calibration factors calculated from the analysis of data acquired using the LED and a time-string related to the date of the event. During the reconstruction process the software finds the two calibration events that closely precede and follow in time the measured event and interpolates the value of the calibration factor. The resulting value is used to normalize the signal recorded by the ADC of each pixel. The effect

of the calibration of the camera can be inferred comparing the results of the reconstruction process obtained before and after the application of the flat field correction. Plots in Fig. 5.5 refers to the same laser profile event: the profile on the left panel was reconstructed without the use of calibration factors, instead that on the right panel was corrected taking into account the different response of each pixel.

Calibrated data are normalized to the nominal energy of the laser using the text file generated in the lidar SBC containing the relative energy of each lidar laser shot as read by the radiometer. Finally laser events are averaged, and an output light profile is generated.

Since in the simulation of the detector the response of each PMTs is the same, simulated profiles don't need the application of the flat field correction. The number of ADC counts which is generated in the simulation when a photon is collected by the PMT differs from the one observed in the measured profile, then a normalization is needed to scale the simulated profile to the measured one. The normalization factor is found analyzing the data acquired using the calibration laser. The reconstructed signal of a measured and of a simulated calibration laser event are shown in Fig.5.6: the simulation reproduces closely the measured signal. In the simulation the value of energy of the laser is set using the value recorded by the probe of the calibration laser to fix the scale between simulated and measured events.

The ratio between the integral of the area under the measured profile and the same corresponding to the simulated profile is used as normalization factor to be applied during the reconstruction of the simulated events of the grid.

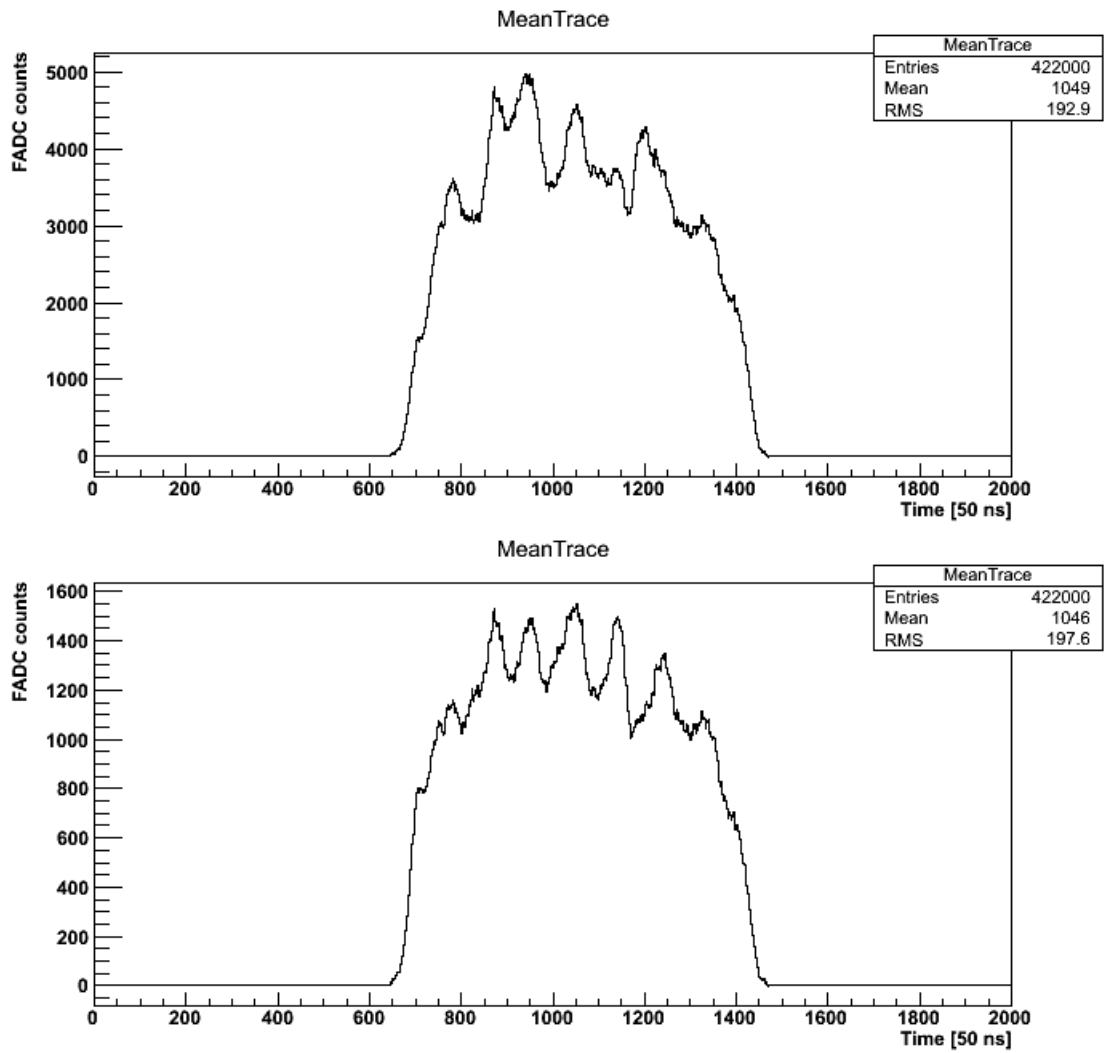


Fig. 5.5: Comparison of a laser light profile reconstructed with (right) and without (left) the use of the flat field correction.

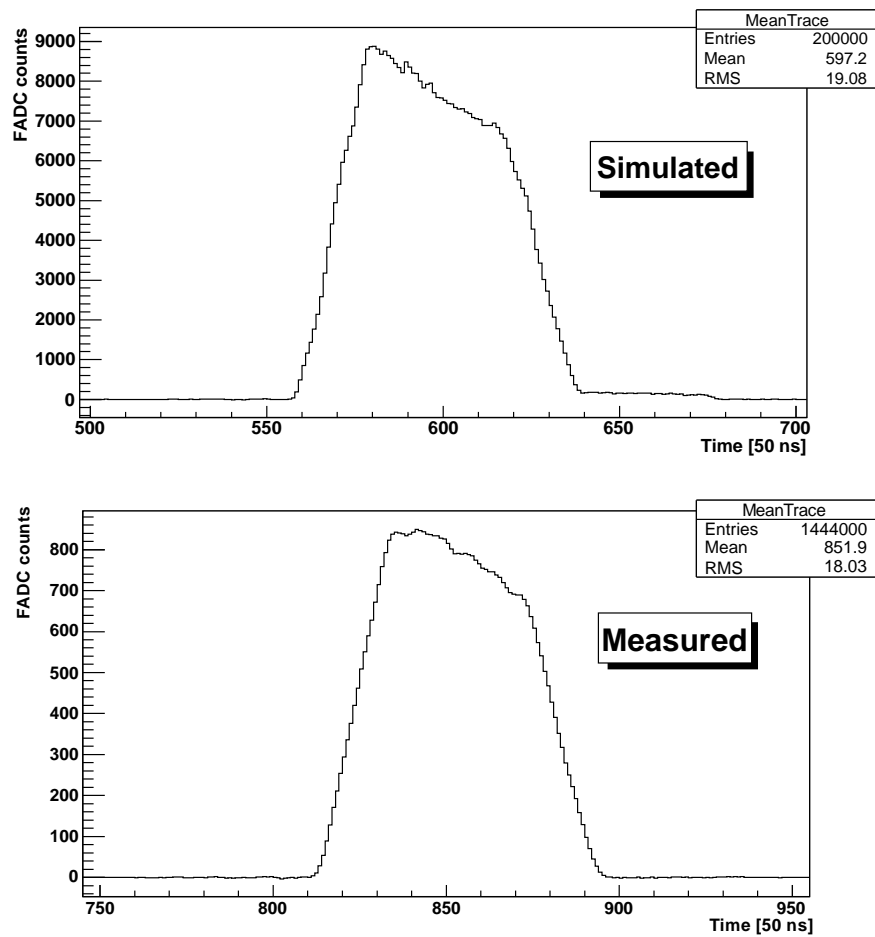


Fig. 5.6: Comparison of a simulated (top) and a measured (bottom) calibration laser profile. The different value of ADC counts forces the use of an absolute calibration factor.

5.3 VAOD measurements using the lidar

The lidar of the ARCADE project uses a short-pulse (7 ns) ND:YAG laser as a transmitter to send an UV light beam through the atmosphere. The emitted light pulse propagates through the atmosphere, where it is attenuated during its travel. At each altitude, some fraction of the light that reaches that point is scattered by aerosols and molecules in the atmosphere. A small portion of this scattered light, namely, the backscattered light reaches the lidar receiver. The telescope collects the backscattered light and focuses the light on the photodetector, which converts the light to an electrical signal. The signal from the detector is then digitized and processed.

Light scattering by particulates and molecules in the atmosphere may be divided into two general types: elastic scattering, where the wavelength of the scattered photon is the same of that of the laser light, and inelastic scattering, where the wavelength of the reemitted light is shifted compared with emitted light. A typical example of an inelastic scattering process is the Raman scattering, in which the wavelength of the scattered light is shifted by a fixed amount [109]. The intensity of the inelastic component of the backscattered light is significantly lower (~ 3 orders of magnitude) than the intensity of the elastically scattered light.

Our lidar is able to separate the two components of the returning signal and to process them separately.

The width in time of the laser pulse is equivalent to the maximum resolution in space achievable by the lidar. The scattering volume that creates the backscattered signal at the time t on the photodetector is located in the range from r_1 to r_2 , where $r_2 = ct/2$ and $r_1 = c(t - \eta)/2$, where c is the speed of light and η the width of the laser pulse. A pulse width of 7 ns correspond to a range of ~ 1.2 m. The factor 2 appears because the light pulse passes along the path from lidar to scattering volume twice, from the laser to the corresponding edge of the scattering volume and then back to the photodetector.

The lidar equation for return signals due to elastic backscattering by air molecules and aerosols can be written as:

$$P(R, \lambda) = \frac{E_0 \cdot F_\lambda}{R^2} O(R) (\beta_{aer}(R, \lambda) + \beta_{mol}(R, \lambda)) \times e^{-2 \int_0^R [\alpha_{aer}(r, \lambda) + \alpha_{mol}(r, \lambda)] dr}, \quad (5.3)$$

where $P(R, \lambda)$ is the signal due to elastic scattering with molecules and particulates received from distance R , E_0 is the energy of the transmitted laser pulse, $F(\lambda)$ contains all the system constants that depend on the efficiency of the receiver optical units, $O(R)$ describes the overlap between the laser beam and the receiver field of view. $\beta_{aer}(R, \lambda)$ and $\beta_{mol}(R, \lambda)$ are the aerosols and

molecular angular backscattering coefficients; $\alpha_{aer}(R, \lambda)$ and $\alpha_{mol}(R, \lambda)$ are the aerosol and molecular extinction coefficients.

A way to solve the lidar equation is the Klett method [110] but the procedure suffers the fact that two physical quantities, $\beta_{aer}(R, \lambda)$ and $\alpha_{aer}(R, \lambda)$ have to be calculated from only one equation. The lidar equation is solved fixing the value of the so-called lidar ratio, $L(R) = \alpha_{aer}(R)/\beta_{aer}(R)$, and this assumption makes the method model dependent.

This problem is overcome with the use of the Raman lidar technique. Atmospheric gases, such as nitrogen, interact with laser light via the Raman scattering process, causing light of longer wavelengths to be scattered. Our lidar collect the Raman-shifted light ($\lambda = 386.7$ nm) scattered by atmospheric nitrogen molecules. The backscattered Raman-shifted signals is given by the following equations [109]:

$$P(R, \lambda_{N_2}) = \frac{E_0 \cdot F_{\lambda_{N_2}}}{R^2} O(R) \beta_{N_2}(R, \lambda_0) \times e^{-\int_0^R [\alpha(r, \lambda_0) + \alpha(r, \lambda_{N_2})] dr}. \quad (5.4)$$

The coefficient $\beta_{N_2}(R, \lambda_0)$ denotes the molecular Raman backscattering due to the nitrogen, while aerosol backscattering does not appear in the equation. $\alpha(R, \lambda)$ is the sum of the aerosols and molecular extinction coefficients: $\alpha(R, \lambda_0)$ describes the extinction on the way up to the scatter region, and $\alpha(R, \lambda_{N_2})$ the extinction on the way back to the lidar.

Eq. 5.4 can be rearranged inserting the expression of the molecular backscatter coefficient that is calculated from the nitrogen number density N_{N_2} , and the molecular differential cross section at the scattering angle $\theta = 180^\circ$:

$$\alpha_{aer}(r, \lambda_0) + \alpha_{aer}(r, \lambda_{N_2}) = \frac{d}{dR} \ln \left(\frac{N_{N_2}(R)}{R^2 P(R, \lambda_{N_2})} \right) + \frac{d}{dR} \ln O(R) - \alpha_{mol}(r, \lambda_0) - \alpha_{mol}(r, \lambda_{N_2}) \quad (5.5)$$

The overlap function is constant, $O(R) = 1$, starting from the distance where the total laser beam enters the receiver field of view, and the wavelength dependence of the particle extinction coefficient can be expressed introducing the Ångström's law (see eq. 1.18).

Finally the aerosol extinction coefficient can be expressed as:

$$\alpha_{aer}(r, \lambda_0) = \frac{\frac{d}{dR} \ln \left(\frac{N_{N_2}(R)}{R^2 P(R, \lambda_{N_2})} \right) - \alpha_{mol}(R, \lambda_0) - \alpha_{mol}(R, \lambda_{N_2})}{1 + \left(\frac{\lambda_0}{\lambda_{N_2}} \right)^\gamma} \quad (5.6)$$

5.3.1 Raman lidar analysis

Lidar return signals are acquired using a digitizer that samples the trace at 1 GS/s. The digitizer is set via software to count the numbers of photons of the trace. A photon is counted when the acquired signal remains over a threshold value for a given time interval. Accurate studies were performed on the shape of the signals generated by a single photon and to identify the characteristic values: if the signal lasted over 45 ADC counts for at least 4 time bins, i.e. 4 ns, the software counts it as a photon; if the same signal lasts more than 25 time bin the signal continuation will be treated as different photons.

Lidar raw data consists in files containing the number of photons counted at a certain time: the digitizer sums photons that are counted within 25 time bins and so the maximum altitude resolution is ~ 4 m. Moreover during data taking the lidar fires a certain number of laser shots; all the signals belonging to the same set of measurements are summed in a single output file.

The lidar signals are treated in order to convert the value of the time bins in range. The conversion of the bin N_{bin} in range is based on the linear function: $R = T_0 + c \cdot k \cdot N_{bin}$, where $k = 1$ bin/ns, and T_0 is the time at which the signal starts, it takes into account all the delay due to the detection system. The value of T_0 was measured during the tests performed in L'Aquila. An optical fiber was used to send the light from the laser output directly on the PMTs; the value of the bin where the signal started, corrected for the length of the fiber, was used to calculate $T_0 = c \cdot k \cdot N_0$.

No other treatments to refine the lidar signal have been performed so far, in the next future we will attempt to subtract the background noise and to evaluate the overlap function to reduce the altitude where the signal starts to be analyzable.

The technique I adopt to analyze lidar signals was developed thanks to the essential support of the Auger atmospheric group of the INFN - Università dell'Aquila. They used this technique to analyze data of a Raman lidar that was installed in the past years at the Pierre Auger Observatory [111].

The technique evaluates the VAOD altitude profile by direct integration of eq. 5.6:

$$VAOD(R) = \int_0^R \alpha(r) dr = -\frac{\ln\left(\frac{P(R, \lambda_0) \cdot R^2}{T_{mol}(\lambda_{N_2}) \cdot T_{mol}(\lambda_0) \cdot N_{N_2}(R)}\right)}{1 + \left(\frac{\lambda_0}{\lambda_{N_2}}\right)^\gamma} + C \quad (5.7)$$

$T_{mol}(\lambda_{N_2})$ and $T_{mol}(\lambda_0)$ are the molecular atmospheric transmission due

to molecular scattering at λ_{N_2} and λ_0 respectively as defined by eq. 1.11; the constant C results from the integration and must be calculated. The Ångström coefficient γ is assumed to be 1. The advantage of using this procedure is the skipping of the numerical calculation of the derivative in eq. 5.6.

I have implemented the data analysis in a C++/ROOT software. A class is dedicated to the calculation of the optical properties of the molecular part atmosphere. The GDAS is used to obtain atmospheric state variables informations. A database contains the altitude profiles of atmospheric pressure, water vapor pressure, temperature and air molecular density recorded every three hours. The atmosphere is treated as a gas mixture and the values of the Rayleigh volume-scattering coefficient is calculated according to equations 1.14 and 1.15. The values of the refractive index and of the King factor are calculated for each air component according to the parametric formulas described in [112] and [113].

The value of the constant C in eq. 5.7 is fixed with a fit procedure. We fit the VAOD altitude profile using a linear function in a range that starts at the altitude where the overlap function is complete up to an altitude lower than the PBL height; then we extrapolate the function down to the ground level and impose the condition $\text{VAOD}(0) = 0$. In this way we use the typical assumption of the linearity of the VAOD profile in the PBL; in my preliminary analysis the fit was performed in the altitude range 600 m ÷ 1 km, in the future, thanks to a better alignment of the lidar system, we expect to reduce the altitude where the overlape function starts to have a unit value, and then we will move down the extreme values of the fit.

An example of the analysis procedure and results are shown in Fig. 5.7: the plot in the top panel represents the Raman signal obtained summing 30000 laser shots, the altitude resolution of the signal is 30 m. The dashed blue line indicates the altitude from where the overlap function is considered complete and then the analysis method can be applied. The plot in the middle panel is the result of the VAOD profile estimated from the Raman signal using eq. 5.7 and the plot in the bottom panel represents the same profile after the calculation of the integration constant. The data are smoothed using a central running average, the smoothed data are drawn in red. The two dashed blue profiles are obtained shifting the smoothed profile by the associated uncertainty. Only a rough estimate of the errors on the VAOD profile was performed: it comes from the propagation of a contribution related to the statistical nature of the photon counting process plus a contribution that takes into account the uncertainties on the parameters resulting from the linear fit procedure. A better estimation of the uncertainties in the VAOD

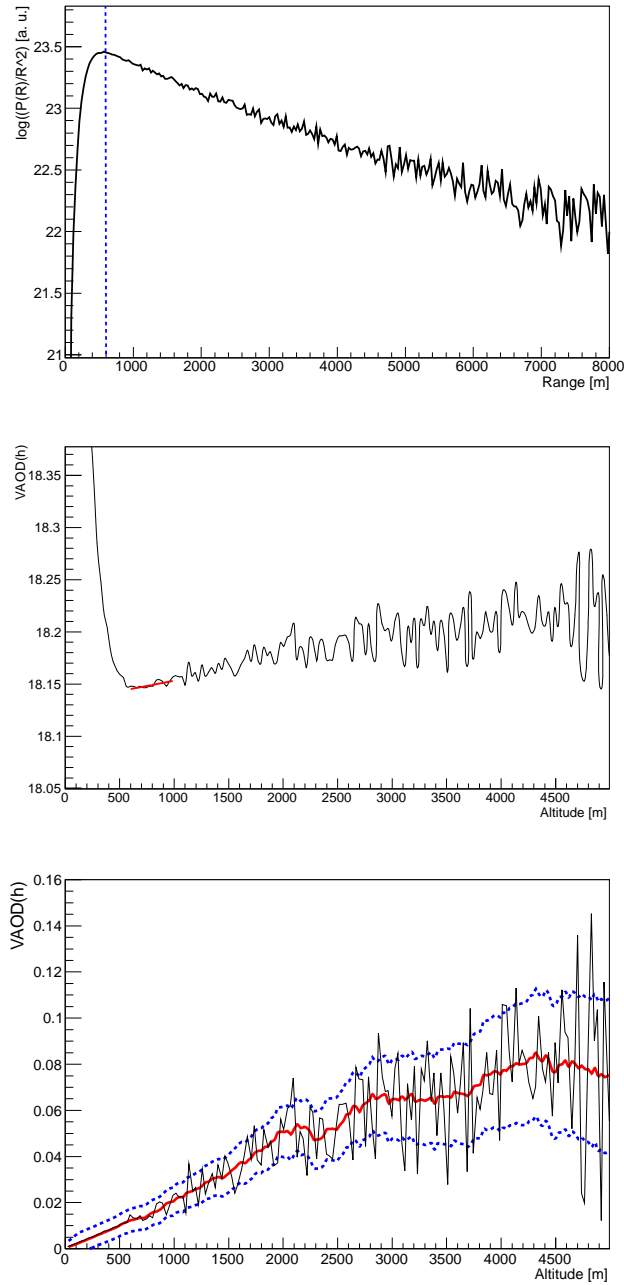


Fig. 5.7: Top: an example of a Raman signal resulting from the sum of 30000 laser shots. The dashed blue line indicate the altitude from where the analysis is performed. Middle: VAOD profile resulting from the analysis of the Raman signal before the evaluation of the integration constant. Bottom: corrected VAOD profile; continous red line is a smoothing obtained using a central running average, dashed blue lines are obtained shifting the smoothed profile by the associated uncertainty.

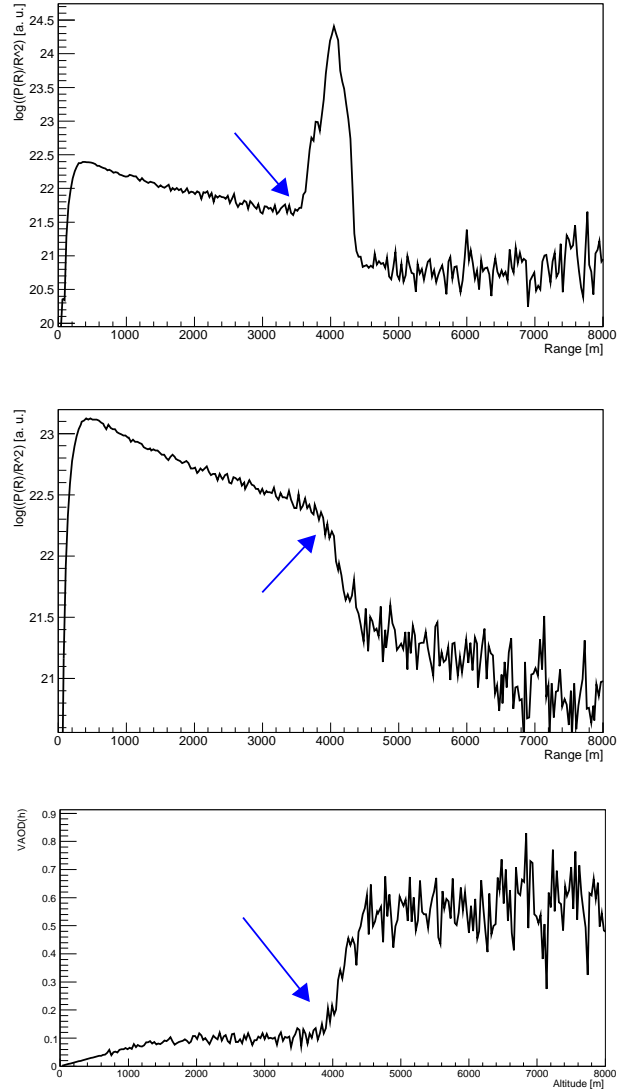


Fig. 5.8: A cloud is present above the lidar: it appears as a bump in the elastic signal (top) and as a depression in the Raman one (middle). The value of the VAOD increases at the altitude correspondig to the cloud base (bottom)

profile will take into account the contributions associated to the molecular transmission factors and to the evaluation of the range from the ADC time bins.

Lidar signals acquired in a cloudy night are shown in Fig. 5.8. As expected, the cloud appears as a bump in the elastic signal (top panel) and as a depression in the Raman one (middle panel). The value of the VAOD increases abruptly at the altitude correspondig to the cloud base due to the high value of its optical depth.

5.3.2 Elastic lidar analysis

The use of a steerable elastic lidar allows to solve the elastic lidar equation without the assumption on the lidar ratio.

Horizontal laser shots can be used to to extract the aerosol extinction coefficient at ground level. Introducing the normalized range-corrected signal, $S(R)$, the expression of the elastic lidar equation becomes [111]:

$$S(R) = \ln \frac{P(R)R^2}{P(R_n)R_n^2} = \ln \frac{O(R)\beta(R)}{O(R_n)\beta(R_n)} - 2 \int_{R_n}^R \alpha(r)dr, \quad (5.8)$$

where the value of the return signal measured at the distance R_n , $P(R_n)$, is used as normalization factor.

Assuming the horizontal homogeneity of the atmosphere at ground level, which means that $\beta(R)$ and $\alpha(R)$ are supposed to be constant along the horizontal path of the laser beam, for a perfectly aligned system $\ln(O(R)/O(R_n)) = 0$ and eq. 5.8 becomes:

$$S(R) = -2\alpha_0(R - R_n), \quad (5.9)$$

where α_0 is the sum of the aerosol and the molecular extinction coefficients at ground. The value of α_0 can be calculated with a simple fit of the previous equation.

If the horizontal homogeneity of the atmosphere can be also assumed at different altitudes eq. 5.8 can be used to evaluate the atmospheric optical depth applying the multi-angle lidar technique: it consists in the measurement of the lidar return signal at different shooting angles. Under the horizontal honogeneity assumption $\alpha(R)$ and $\beta(R)$ don't depend on the shooting angle θ , and where the overlap function is complete, the range-corrected signal

function becomes:

$$S(R, \theta) = \ln \frac{\beta(R)}{\beta(R_n)} - \frac{2}{\cos\theta} \int_{R_n}^R \alpha(r) dr = \ln \frac{\beta(R)}{\beta(R_n)} - 2 \sec\theta \cdot \tau(R, R_n) \quad (5.10)$$

For the purpose of the analysis the atmosphere is divided in horizontal slices, and for each one the values of $S(r, \theta)$ at different angles is evaluated. The value of the optical depth is extracted with a linear regression from eq. 5.10.

5.4 Next step: comparison of the results

The main goal of the ARCADE project is the comparison of the measurement of aerosol optical depth performed using different instruments and analysis methods.

This study will clarify the validity of the different assumptions on which each method is based, and then will determine the limits of applicability of these techniques.

For example the multi-angle analysis can be used to verify the linear trend of the VAOD profile in the low atmosphere assumed in the Raman analysis; the value of the aerosol extinction coefficient estimated from the the analysis of horizontal laser shots can be directly compared with that estimated with the analysis of the side-scattering data acquired by the AMT, infact one of the parameters resulting from the Laser Simulation Analysis is $L_{aer} = 1/\alpha_0$. Nevertheless the analysis of Raman return signals acquired at different shooting angles can be useful to check the horizontal homogeneity of the atmosphere, assumption on which all the other analysis methods are based.

Currently the set-up of the experimental apparatus is completed, the instruments are in acquisition phase and the analysis techniques developed for the purpose are being finalized.

Regarding my work on the development of the data analysis techniques both the side-scattering analysis and the Raman analysis methods are mainly complete but need some refinements. In particular the simulation of the AMT has to be refined in order to produce light profile that are more similar than possible to the measured ones and to make then results deriving from the comparison method reliable. Concerning the Raman analysis, a better treatment of the raw lidar return signals and a better estimation of the uncertainties in the VAOD profile are the only aspects to be refined. Both the targets will be hit in the next future.

Conclusions

A detailed knowledge of the atmospheric conditions is a crucial point in experiments based on the detection of fluorescence light emitted by cosmic ray showers, since they use the atmosphere as a huge calorimeter. In particular the atmospheric property that most affects air shower measurements is the variation of aerosol conditions: in hazy nights the aerosol attenuation can affect the reconstructed energy of distant showers up to 40%. In the Pierre Auger Observatory, hourly measurements of the vertical aerosol optical depth (VAOD) altitude profile are performed using the telescopes of the Fluorescence Detector (FD): they record vertical UV laser tracks produced by the two laser facilities of the observatory, the Central Laser Facility (CLF) and the eXtreme Laser Facility (XLF).

During the three years of my PhD activity, the understanding of the light attenuation by aerosols in the Auger experiment was greatly improved. This was achieved by the addition of a new laser facility (XLF), the upgrade of the existing one (CLF) with the addition of a Raman Lidar (CRLF), improved calibration of the Fluorescence Detector, a better understanding of the energy monitor of the lasers which led to more accurate results with reduced statistical and systematics uncertainties, and finally a better description of the aerosol stratification including the Planetary Boundary Layer.

As a member of the atmospheric monitoring group of the Pierre Auger Collaboration, I worked on the data analysis of vertical laser tracks for the production of hourly aerosol attenuation profiles to be included in the Auger aerosol database. I performed the analysis of laser data using the “Laser Simulation Analysis”, a method that compares measured laser profiles to a grid of simulated laser events, generated varying the aerosol conditions according to a two parameters model, to find the best compatibility.

I applied for the first time this analysis technique to XLF data: in 2010 this new laser facility was installed at the Pierre Auger Observatory, with the purpose of having two laser facilities each equidistant from three of the four FD buildings. Results of this work have been at first used to produce aerosol attenuation profiles for the Loma Amarilla FD site; then, in 2014, they were

used to fill an updated version of the aerosol database containing 2013 data: in this release XLF data were used to produce VAOD profiles for each FD telescope during the CLF upgrade.

In 2013 I also contributed to the complete revision of the Auger aerosol database. The result of this work was the production of nine years (2004 - 2012) of aerosol profiles obtained with the Laser Simulation Analysis using both laser facilities. This release includes a more precise evaluation of the energy calibration of the lasers, addition of more data, new FD calibration constants that led to a reduction of the total uncertainties on the VAOD profiles that propagates on the energy scale.

Finally I improved the Laser Simulation Analysis including a third parameter, the height of the Planetary Boundary Layer, in the description of the aerosol attenuation to produce more realistic VAOD altitude profiles. A comparison between the VAOD profiles obtained using the two and three parameters Laser Simulation Analysis shows that results are strongly correlated, however the introduction of the PBL allows a more accurate description of the lower layers. The three parameters analysis will be used for the next release of the aerosol database.

Despite of the great improvements achieved in the Auger atmospheric analysis, the side scattering technique should be fully validated by means of a detailed comparison to the usual lidar analysis (Raman and multi-angle for the elastic signals). The ARCADE project aims to compare different methods (back-scattering and side-scattering), and different analyses (elastic, Raman Lidar and Laser Simulation) on the same air mass without the limitations imposed by the interference of the lasers sources with the data taking in the Auger experiment.

Working in the ARCADE group I had the challenging opportunity to participate to all the phases of a new experiment, from the design phase to the realization, data taking and finally to the data analysis, since the small number of members of the project imposed on us to work on all the necessary items.

In this thesis I described in details the project and in particular the work I performed both on the hardware setup and on the software development.

Concerning the hardware work, I took part to the design of the lidar and the final assembling in the INFN mechanical workshop in Torino and to the tests of the system in L'Aquila. After the optimization of the system, we mounted the lidar in Lamar (USA) where I participated also to the setup of the AMT. I wrote the entire code for the management of the high voltage power supply modules needed by the PMTs of the lidar, and the program for the control of the radiometer used to monitor the laser energy. Finally I worked at the analysis of the AMT data and of the Raman lidar signals. I developed a

detailed simulation of the AMT telescope using Geant4 to apply a custom version of the Laser Simulation Analysis to the AMT data. Results of the simulation are promising, some refinements are needed before the application to the data analysis. I carried out a preliminary Raman analysis and first results are presented in these thesis. A better treatment of the uncertainties should be developed.

The experiment is now in data acquisition phase and is fully controlled remotely.

The challenge of setting up an entirely new experiment was successful, the devices will continue the data taking for all the 2015 and in the near future the data analysis methods will be ready, and it will be possible to compare the results obtained with different instruments and analysis techniques.

Bibliography

- [1] V. Hess, *Phys. Zeit*, **13**, 1084 (1912)
- [2] A. H. Compton, *Phys. Rev.*, **43**, 387 (1933)
- [3] P. Auger and R. Maze, *C. R. Acad. Sci. Ser. B* **207**, 228 (1938)
- [4] J. Linsley, *Phys. Rev. Lett*, **10**, 146 (1963)
- [5] B. Peters, *Il Nuovo Cimento*, **22**, 800 (1961)
- [6] W. D. Apel et al., *Astropart. Phys.* **36**, 183 (2012)
- [7] J. Abraham et al., Pierre Auger Collaboration, *Physics Letters B*, **685** 239 (2010)
- [8] A. M. Hillas, *J. Phys. G: Nucl. Part. Phys.*, **31** R95 (2005)
- [9] K. Greisen, *Phys. Rev. Letters*, **16**, 748 (1966)
- [10] G. T. Zatsepin and V. A. Kuzmin, *JETP Lett.*, **4**, 78 (1966)
- [11] P. Auger, et al., *Rev. Mod. Phys.* **11**, 288 (1939)
- [12] E. Fermi, *Phys. Rev.*, **75**, 1169 (1949)
- [13] A. M. Hillas, *Ann. Rev. Astron. Astrophys.*, **22**, 425 (1984)
- [14] V. Berenzinsky, et al., *Phys. Rev. Lett.*, **79**, 4302 (1997)
- [15] V. A. Kuzmin and I. Tkachev, *JEPT Lett.*, textbf68, 271 (1998)
- [16] C. T. Hill, *Nucl. Phys.* **B 224**, 469 (1983)
- [17] P. Bhattacharjee, C. T. Hill and D. N. Schramm, *Phys. Rev. Letters*, **69**, 567 (1992)

- [18] W. Heitler, *The Quantum Theory of Radiation*, Oxford University Press, London (1944)
- [19] J. Matthews, *Astropart. Phys.* **22**, 387 (2005)
- [20] M. Takeda et al., *Astropart. Phys.* **19**, 446 (2003)
- [21] J. Matthews, et al., *32nd ICRC proceedings*, (Beijing, China) 2011, 273
- [22] C. Berat for the Pierre Auger Collaboration, *Nucl. Instr. and Meth.*, **A 718**, 471 (2013)
- [23] F. Arqueros, J. R. Horandel, B. Keilhauer, *Nucl. Instr. and Meth.*, **A 597**, 1 (2008)
- [24] M. Ave, et al., *Nucl. Instr. and Meth.* **A 597** 41, (2008)
- [25] F. E. Kakimoto et al., *Nucl. Instr. and Meth.* **A 372**, 527, (1996)
- [26] R. M. Baltrusaitis, et al., *Nucl. Instr. and Meth.* **A 240**, 410 (1985)
- [27] M. Nagano, et al., *Astropart. Phys.* **22** 235, (2004)
- [28] T. Waldenmaier, et al., *Nucl. Instr. and Meth.* **A 597**, 67 (2008)
- [29] F. Arqueros, et al., *Nucl. Instr. and Meth.* **A 597**, 94 (2008)
- [30] J. Belz, et al., *Astrop. Phys.* **25**, 5763 (2006)
- [31] V. A. Kovalev and W. E. Eichinger, *Elastic Lidar - Theory, Practice, and Analysis Methods*, Wiley, (2004)
- [32] J. Abraham, et al., Pierre Auger Collaboration, *Astrop. Phys.* **33**, 108 (2010)
- [33] B. Keilhauer et al., *Astrop. Phys.* **25**, 259 (2006)
- [34] <http://www.ncdc.noaa.gov/data-access/model-data/model-datasets/global-data-assimilation-system-gdas>
- [35] L. Valore for the Pierre Auger Collaboration, *Nucl. Instr. and Meth.* **A 630**, 246 (2011)
- [36] D. K. Killinger, N. Menyuk, *Science* **235**, 37 (1987)
- [37] J. H. Seinfeld, S. N. Pandis, *Atmospheric Chemistry and Physics: From Air Pollution to Climate Change*, Wiley, 2006

- [38] S. Y. BenZvi et al., *Astrop. Phys.* **28**, 312 (2007)
- [39] L. G. Henyey, L. J. Greenstein, *Astrophis. J.* **93**, 70 (1941)
- [40] The Pierre Auger Collaboration *Nucl. Instr. and Meth.* **A 523**, 50 (2004)
- [41] The Pierre Auger Collaboration *Nucl. Instr. and Meth.* **A 613**, 29 (2010)
- [42] The Pierre Auger Collaboration *Nucl. Instr. and Meth.* **A 620**, 227 (2010)
- [43] Federico Sánchez for the Pierre Auger Collaboration, *32nd ICRC proceedings* Beijing, China (2011)
- [44] T. H.-J. Mathes for the Pierre Auger Collaboration, *32nd ICRC proceedings* Beijing, China (2011)
- [45] J. L. Kelly for the Pierre Auger Collaboration, *32nd ICRC proceedings* Beijing, China (2011)
- [46] R. Gaior for the Pierre Auger Collaboration, *32nd ICRC proceedings* Beijing, China (2011)
- [47] P. Allison for the Pierre Auger Collaboration, *32nd ICRC proceedings* Beijing, China (2011)
- [48] J. Alvarez et al., arXiv:1208:2734
- [49] P. Abreu, et al., The Pierre Auger Collaboration, *Astrop. Phys.* **34**, 368 (2011)
- [50] J. Hersil, et al., *Phys. Rev. Lett.*, **6**, 22 (1961)
- [51] V. Verzi for The Pierre Auger Collaboration, *33rd ICRC proceedings*, Rio de Janeiro, Brasil, (2013)
- [52] I. Allekotte, et al., The Pierre Auger Collaboration, *Nucl. Instr. and Meth.* **A 586**, 409 (2008)
- [53] D. Allard et al., The Pierre Auger Collaboration, *29th ICRC proceedings*, Pune, India, (2005)
- [54] R. C. Shellard for the Pierre Auger Collaboration, *Brazilian Journal of Physics*, **36 4A**, 1184 (2006)
- [55] J. Abraham et al., The Pierre Auger Collaboration, *Nucl. Instr. and Meth.* **A 620**, 227 (2010)

- [56] Schott Glaswerke, Mainz, Germany - <http://www.schott.com>
- [57] PHOTONIS - <http://www.photonis.com>
- [58] G. Matthiae, P. Privitera, *Pierre Auger Project Technical Note, GAP-99-011* (1999).
- [59] T.K. Gaisser, A.M. Hillas, *15th ICRC proceedings*, Plovdiv, Bulgaria (1977)
- [60] A. Aab, et al., The Pierre Auger Collaboration, *33rd ICRC proceedings*, Rio de Janeiro, Brazil, (2013)
- [61] K. Kamata, J. Nishimura, *Proc.Theor.Phys.Supplement* **6** 93 (1958)
- [62] D. Newton, J. Knapp, A. A. Watson, The Pierre Auger Collaboration, *Astropart. Phys.* **26** 414 (2007)
- [63] S. Argiro, et al. for the Pierre Auger Collaboration, *Nucl. Instr. and Meth.* **A 580** 1485 (2007)
- [64] A. Schulz for the Pierre Auger Collaboration, *33rd ICRC proceedings*, Rio de Janeiro, Brasil, (2013)
- [65] A. Aab et al., The Pierre Auger Collaboration, *Phys. Rev. D* **90**, 122005 (2014)
- [66] J. Abraham et al., The Pierre Auger Collab., *Astropart. Phys.* **27**, 155 (2007)
- [67] M. Settimo for The Pierre Auger Collaboration, *32nd ICRC proceedings* Beijing, China (2011)
- [68] P. Pieroni, for The Pierre Auger Collaboration, *33rd ICRC proceedings*, Rio de Janeiro, Brasil, (2013)
- [69] J. N. Bahcall and E. Waxman, *Phys. Rev.* **D64** , 023002 (2001)
- [70] IceCube Collab., R. Abbasi et al., *Phys. Rev.* D83, 092003 (2011)
- [71] ANITA Collab., P. Gorham et al., *Phys. Rev.* D85, 049901 (2012)
- [72] RICE Collab., I. Kravchenko et al., *Phys. Rev.* D85, 062004 (2012)
- [73] HiRes Collab., R. U. Abbasi et al., *Astrophys. J.* 684, 790 (2008)

- [74] J. Abraham, et al. , The Pierre Auger Collaboration, *Science*, **318**, 938 (2007)
- [75] M.-P. Veron-Cetty, and P. Veron, *A&A*, **455**, 773 (2006)
- [76] K.-H. Kampert, for the Pierre Auger Collaboration *32nd ICRC proceedings* Beijing, China (2011)
- [77] P. Abreu et al., The Pierre Auger Collaboration, *Phys. Rev. Lett.* **109**, 062002 (2012)
- [78] R. J. Glauber and G. Matthiae, *Nucl. Phys.* **B21**, 135 (1970).
- [79] E. Harold, W. Means, *XML in a Nutshell*, O'Reilly Media, 2004
- [80] J. Abraham et al., The Pierre Auger Collaboration, *Astrop. Phys.* **33**, 108 (2010)
- [81] B. Keilhauer, M. Will, The Pierre Auger Collaboration, *Eur. Phys. J. Plus* **127**, 96 (2012)
- [82] P. Abreu, et al., The Pierre Auger Collaboration, *Astrop. Phys.* **35**, 591 (2012)
- [83] S. BenZvi, et al., The Pierre Auger Collaboration, *30th ICRC proceedings*, Merida, Mexico, (2007)
- [84] B. Fick, et al., The Pierre Auger Collaboration, *JINST* **1** P11003 (2006)
- [85] L. Wiencke, The Pierre Auger Collaboration, *32nd ICRC proceedings* Beijing, China (2011)
- [86] The Pierre Auger Collaboration, *JINST* **8** 04009 (2013)
- [87] J.Chirinos for The Pierre Auger Collaboration, *33rd ICRC proceedings*, Rio de Janeiro, Brasil, (2013)
- [88] S. BenZvi, et al., The Pierre Auger Collaboration, *Nucl.Instrum.Meth.* **A574** 171 (2007)
- [89] V. Rizi, A. Tonachini, M. Iarlori, G. Visconti, The Pierre Auger Collaboration, *Eur.Phys.J.Plus* **127** 92 (2012)
- [90] R. Abbasi et al., *Astropart. Phys.* **25** 74 (2006)
- [91] L. Valore for The Pierre Auger Collaboration, *33rd ICRC proceedings*, Rio de Janeiro, Brasil, (2013)

- [92] A. Filipcic, M. Horvat, D. Veberic, D. Zavrtanik, M. Zavrtanik *Astrop. Phys.* **18** 501 (2003)
- [93] M. Buscemi, C. Cassardo, M. Cilmo, M. Coco, S. Ferrarese, F. Guarino, A. S. Tonachini, L. Valore, L. Wiencke “ARCADE-Atmospheric Research for Climate and Astroparticle Detection”, *1st AtmoHEAD proceedings*, Paris, France (2013)
- [94] M. Buscemi, C. Cassardo, M. Cilmo, M. Coco, S. Ferrarese, F. Guarino, A. S. Tonachini, L. Valore, L. Wiencke- “The ARCADE project: characterization of aerosol attenuation properties in the near UV for astroparticle experiments”, *33rd ICRC proceedings*, Rio de Janeiro, Brasil, (2013)
- [95] <http://www.quantel-laser.com/products/item/centurion-40-mj-135.html>
- [96] <http://www.laserprobeinc.com/Rjp445.pdf>
- [97] http://www.zaber.com/products/product_group.php?group=T-MM
- [98] <http://www.caen.it/csite/CaenProd.jsp?parent=14&idmod=632>
- [99] <http://www.earlinet.org/>
- [100] http://www.tunl.duke.edu/documents/public/electronics/CAEN/caen_n126-n186.pdf
- [101] <http://www.acmesystems.it/aria>
- [102] <http://www.ti.com/lit/ds/symlink/ads8343.pdf>
- [103] <http://www.linear.com/product/LTC2602>
- [104] L. Wiencke for the Pierre Auger Collaboration and at., *32nd ICRC proceedings* Beijing, China (2011)
- [105] L. Valore, M. Buscemi, C. Cassardo, M. Cilmo, M. Coco, S. Ferrarese, F. Guarino, M. Iarlori, H.J. Mathes, V. Rizi, A.S. Tonachini, L. Wiencke, M. Will, “ARCADE: description of the project and setup of the Lidar/AMT system”, *2nd AtmoHEAD proceedings*, Padova, Italy, (2014)
- [106] J. Smith, J. Thomas, S. Thomas, and L. Wiencke, *30th ICRC proceedings*, Merida, Mexico, 5 997-1000 (2007)

- [107] A.S.Tonachini, L.Valore, M.Buscemi, C.Cassardo, M.Cilmo, M.Coco, S.Ferrarese, F.Guarino, M.Iarlori, H.-J.Mathes, V.Rizi, L.Wiencke, and M.Will, “ARCADE - Atmospheric Research for Climate and Astroparticle DEtection”, *5th RICAP proceedings*, Noto, Italy, (2014)
- [108] S. Agostinelli et al., GEANT4 Collaboration, *Nucl. Instrum. Meth. A* **506** 250, (2003)
- [109] C. Weitcamp, *Lidar: Range-resolved optical remote sensing of the atmosphere*, Springer Series in Optical Sciences, (2005)
- [110] J. D. Klett, *Appl. Opt.* **20**, 211 (1981)
- [111] V. Rizi, A. Tonachini for the Pierre Auger Collaboration, M. Iarlori and G. Visconti, *Eur. Phys. J. Plus* **127** 92 (2012)
- [112] D. R. Bates, *Planet. Space Sc.* **32** 785, (1984)
- [113] B. A. Bodhaine, N. B. Wood and E. G. Dutton, *Journal of Atmospheric and Oceanic Technology* **16** 1854 (1999)